# CONTRIBUTION OF ION TEMPERATURE ANISOTROPY AND VELOCITY SHEARS IN THE DIRECT GENERATION OF SMALL-SCALE IRREGULARITIES IN THE HIGH-LATITUDE F-REGION

## CONTRIBUTION DES ANISOTROPIES DE TEMPÉRATURE ET DES CISAILLEMENTS DE VITESSES IONIQUES DANS LA GÉNÉRATION DIRECTE D'IRRÉGULARITÉS À PETITE ÉCHELLE AU SEIN DE LA RÉGION F DE L'IONOSPHÈRE À HAUTES LATITUDES

A Thesis Submitted

to the Division of Graduate Studies of the Royal Military College of Canada

by

Patrick J.G. Perron, CD, BSc, MSc
Major

In Partial Fulfillment of the Requirements for the Degree of

Doctor of Philosophy

May 27, 2014

*À mon amoureuse Marie-Andrée*

# Acknowledgements

Je remercie mon aviseur, Dr. Jean-Marc Noël, pour son grand soutien et sa confiance. Merci Jean-Marc de m'avoir introduit à la physique spatiale et de m'avoir fourni des opportunités aussi enrichissantes. Je dois également souligner l'énorme contribution du Dr. Jean-Pierre St-Maurice à l'Université de Saskatchewan qui a été pour moi un mentor scientifique et une source intarissable de précieux conseils. Il a toujours pris le temps de réviser mes travaux et de discuter de mes résultats malgré la distance nous séparant et son horaire très chargé.

I would also like to thank Dr. Konstantin Kabin at RMCC who has been a great scientific mentor for the past 3 years. He has expressed a constant interest in my work and has provided valuable and insightful scientific advices on numerous occasions. I would also like to thank John De Boer, Laureline Sangalli, Albert Russel and Alex Cushley for the great discussions on space weather and space physics!

Finalement, ce travail n'aurait pas été possible sans l'appui inconditionnel de mon amoureuse Marie! Merci pour ta grande compréhension lorsque je passais des heures dans le bureau à faire le "scientifique fou"!

# Abstract

Perron, Patrick J.G. Royal Military College of Canada, May 27, 2014. *Contribution of ion temperature anisotropy and velocity shears in the direct generation of small-scale irregularities in the high-latitude F-region* Supervised by Dr. Jean-Marc Noël.

Plasma instabilities play an important role in producing small-scale irregularities in the ionosphere. In particular, current-driven electrostatic ion-acoustic (CDEIA) instabilities contribute to high-latitude F-region electrodynamics. CDEIA instabilities are affected by ion velocity shears and temperature anisotropies. Ion temperature anisotropies with perpendicular enhancements often exist in the high-latitude F-region. In addition to temperature anisotropies, ion velocity shears are observed near auroral arc edges, sometimes coexisting with thermal ion upflow processes and field-aligned currents (FAC). We investigated whether ion temperature anisotropy or shears lower the threshold conditions required for the onset of CDEIA instabilities and also, enhance the incoherent scattering from ion-acoustic waves. We generalized a dispersion relation to include ion thermal anisotropy, finite Larmor radius corrections and collisions. We derived new fluid-like analytical expressions for the threshold conditions required for instability. We studied how the instability threshold conditions vary as a function of the wave vector direction in both fluid and kinetic regimes. We found that, in some cases, ion temperature anisotropy lowers significantly the threshold drift requirements for a large range of intermediate aspect angles. In particular, realistic ion temperature anisotropies contribute to reducing the instability threshold velocity shears that are associated with small relative drift thresholds, for modes propagating almost perpendicularly to the geomagnetic field. Such instabilities could play a role in the direct generation of field-aligned irregularities in the collisional F-region that could be observed with the Super Dual Auroral Radar Network (SuperDARN) array of high-frequency radars. These modes would be very sensitive to the radar probing direction

since they are restricted to very narrow angular intervals. On the other hand, our study confirmed that temperature anisotropies in magnetized plasmas are unimportant when the incoherent radar is pointing at the critical angle for which the total temperature is equal to the effective temperature. Yet, under the right conditions, "small" ion velocity shears produce significant enhancements in ISR spectra, especially for directions near perpendicular to the geomagnetic field. This could lead to overestimations of the interpreted electron to ion temperature ratio and electron density when using standard ISR fitting procedures. In closing, ion temperature anisotropies and velocity shears are important parameters that need to be considered in the studies of CDEIA waves and instabilities in the high-latitude F-region, especially for propagation directions near perpendicular to the geomagnetic field.

# Résumé

Perron, Patrick J.G. Collège militaire royal du Canada, April, 2014. *Contribution des anisotropies de température et des cisaillements de vitesses ioniques dans la génération directe d'irrégularités à petite échelle au sein de la région F de l'ionosphère à hautes latitudes* Thèse dirigée par M. Jean-Marc Noël, Ph.D.

Les instabilités du plasma jouent un rôle important dans la production d'irrégularités à petite échelle au sein de l'ionosphère. En particulier, les instabilités électrostatiques ion-acoustiques déclenchées par courants contribuent aux processus électrodynamiques de la région F à hautes latitudes. Ces instabilités sont affectées par les cisaillements de vitesse ionique et les anisotropies de température. Les anisotropies de température avec une température perpendiculaire plus importante que parallèle se manifestent souvent au sein de la région F à hautes latitudes. En outre, des cisaillements de vitesse sont observées près des contours des arcs auroraux, parfois en présence de remontées d'ions thermiques et de courants alignés avec le champ magnétique. Nous avons examiné si les anisotropies de température ou bien les cisaillements de vitesse réduisent les conditions de seuil requises pour le déclenchement d'instabilités ion-acoustiques et aussi, si elles augmentent la diffusion incohérente à partir des ondes ion-acoustiques. Nous avons généralisé une relation de dispersion en incluant les anisotropies thermiques, les corrections du rayon de Larmor et les collisions. Nous avons dérivé de nouvelles expressions analytiques de nature fluide pour les conditions de seuil requises pour déclencher l'instabilité. Nous avons étudié comment les conditions de seuil varient en fonction de la direction du vecteur d'onde pour les régimes fluide et cinétique. Dans certains cas, nous avons trouvé que les anisotropies de température diminuent de façon significative la dérive de seuil pour une gamme d'angles d'aspect intermédiaires. En particuler, des anisotropies de température réalistes réduisent les dérives minimales vers des plus petites valeurs seuil de cisaille-

ment, pour les ondes se propageant vers des directions presque perpendiculaires au champ magnétique. Ces instabilités pourraient contribuer à la génération directe d'irrégularités alignées avec le champ magnétique au sein de la région F et en présence de collisions. Ces irrégularités pourraient être observées avec des radars à diffusion cohérente à haute-fréquence. D'autre part, nous avons confirmé que les anisotropies de température au sein d'un plasma magnétisé sont d'importance moindre lorsqu'un radar à diffusion incohérente pointe vers la direction correspondant à l'angle critique pour lequel la température totale est égale à la température effective. Cependant, dans les bonnes conditions, de petits cisaillements de vitesse ionique produisent des augmentations importantes des spectres à diffusion incohérente, spécialement pour des directions presque perpendiculaires au champ magnétique. Ceci pourrait mener à une surestimation du rapport de température électron/ion et de la densité électronique lorsque les procédures normalisées d'ajustement aux spectres à diffusion incohérente sont utilisées. Pour conclure, les anisotropies de température et les cisaillements de vitesse sont d'importants paramètres qui doivent être considérés dans l'étude des ondes et des instabilités ion-acoustiques au sein de la région F à hautes latitudes et pour des petits angles d'aspect.

**Mots clés :** Ionosphère (ondes et instabilités dans un plasma) - Physique des plasmas spatiaux (Ondes et instabilités; théorie cinétique) - Irrégularités à petite échelle - radars à spectre incohérent - radars à spectre cohérent

# Contents

# List of Tables

# List of Figures

# List of Symbols

| Symbol | Description |
|---|---|
| $A_e$ .............. | Antenna effective gain |
| $A_i$ .............. | Ion temperature anisotropy ratio ($= T_{\perp i}/T_{\parallel i}$) |
| $\mathbf{a}$ .............. | Acceleration vector |
| $\mathbf{B}$ .............. | Magnetic field vector |
| $\mathbf{B}_0$ .............. | Ambient Earth magnetic field vector (in Tesla) |
| $\mathbf{B}_{sw}$ .............. | Solar wind magnetic field vector |
| $B_z$ .............. | Vertical component of the magnetic field |
| $\mathbf{B}_1$ .............. | Perturbed magnetic field |
| $b$ or $b_i$ .............. | Argument of the exponentially scaled modified Bessel function of the first kind ($= k_\perp^2 \rho_{Li}^2$) (in Chap. 3) |
| $b_e$ .............. | $= k_\perp^2 \rho_{Le}^2$ (in Chap. 4) |
| $b_j(\xi)$ .............. | Phase argument of the exponential (in Chap. 3) |
| $b_s$ .............. | $= k_\perp C_s^2/\Omega_i^2$ |
| $c$ .............. | Speed of light in vacuum ($= 3 \times 10^8 m/s$) |
| $C_s$ .............. | Isothermal ion acoustic speed ($= \sqrt{(\gamma_e T_e + \gamma_i T_i)/m_i}$ where $\gamma_e = \gamma_i = 1$ ) |
| $D$ .............. | Magnitude of the E×B drift velocity |
| $\mathbf{E}$ .............. | Electric field vector |
| $E_a$ .............. | Auroral zone electric field |
| $\mathbf{E}_0$ .............. | Ambient electric field vector (unperturbed) |
| $E_{pc}$ .............. | Polar cap electric field |
| $\mathbf{E}_{sw}$ .............. | Solar wind electric field vector |
| $\mathbf{E}_1$ .............. | Perturbed electric field |
| $e$ .............. | Elementary charge ($= 1.602 \times 10^{-19}C$) |
| $f_j = f_j(\mathbf{r},\mathbf{v},t)$ ..... | Average distribution function of species $j$ |
| $f_0$ .............. | Frequency of radar incident wave (in Chap. 4) |
| $f_{0bm}$ .............. | Bi-Maxwellian distribution function |
| $f_{0j}$ .............. | Average unperturbed distribution function of species $j$ |
| $f_{0m}$ .............. | Maxwellian distribution function |
| $f_{1j}$ .............. | Average perturbed distribution function of species $j$ |
| $G$ .............. | Transmit gain ($= 4\pi/\Omega$) |
| $H_j = H_j(k,\omega)$ ..... | Susceptibility of species $j$ |
| $\mathbf{J}$ .............. | Current density vector |
| $\mathbf{k}$ .............. | Wavenumber vector in the y-z plane ($\mathbf{k}=k_\perp \hat{y} + k_\parallel \hat{z}$) |
| $k_B$ .............. | Boltzmann's constant ($= 1.38 \times 10^{-23} J/K$) |
| $k_0$ .............. | Radar incident wavenumber |

| | | |
|---|---|---|
| $L_s$ | ............... | Spatial scale length associated with the hydrodynamic drift velocity gradient |
| $m_j$ | ............... | Mass of species $j$ |
| $m_n$ | ............... | Neutral mass |
| $n_j$ | ............... | Number density of species $j$ |
| $n_{0j}$ | ............... | Unperturbed number density of species $j$ |
| $n_{1j}$ | ............... | Perturbed number density of species $j$ |
| $P_r$ | ............... | Received power |
| $P_t$ | ............... | Transmitted power |
| $Q_{in}^k$ | ............... | Generalized ion-neutral collisional cross-section (where $k$ is an integer) |
| $q_j$ | ............... | Charge of species $j$ |
| $\mathbf{r}$ | ............... | Position vector |
| $r$ | ............... | Radar range |
| $\Delta r$ | ............... | Radar range resolution |
| $S(k,\omega)$ | ............... | Spectrum desnity function |
| $S_i$ | ............... | Normalized ion shear $(= V'_{di}/\Omega_i)$ |
| $T$ | ............... | Total temperature $T = \frac{1}{3}(T_\parallel + 2T_\perp)$ or radar averaging integration time |
| $T_{if}$ | ............... | Effective ion temperature along the radar line-of-sight |
| $T_j$ | ............... | Temperature of species $j$ (in eV) |
| $T_n$ | ............... | Neutral temperature |
| $t$ | ............... | Time |
| $\mathbf{U}$ | ............... | Neutral wind velocity |
| $U_j = U_j(k,\omega)$ | ............... | Function arising from the BGK collision model in linearized Boltzmann equation |
| $u$ | ............... | One-dimensional velocity component |
| $V$ or $V_s$ | ............... | Scattering volume |
| $V_{de}$ | ............... | Electron parallel drift with respect to the ions (or electron-ion parallel relative drift) |
| $V_{di/n}$ | ............... | Relative ion-neutral drift |
| $V_{dj}$ | ............... | Drift velocity of species $j$ |
| $\mathbf{V}_{sw}$ | ............... | Solar wind drift velocity |
| $\mathbf{V}_{0\perp}$ | ............... | Plasma E×B drift |
| $\mathbf{v}$ | ............... | Velocity vector |
| $v_{tj}$ | ............... | Thermal velocity of species $j$ $\left(= \sqrt{k_B T_j/m_j}\right)$ |
| $v_\perp$ | ............... | Velocity perpendicular to the magnetic field |
| $v_\parallel$ | ............... | Velocity parallel to the magnetic field |
| $v_{\perp t}$ | ............... | Perpendicular thermal velocity $\left(= \sqrt{k_B T_\perp/m}\right)$ |
| $v_{\parallel t}$ | ............... | Parallel thermal velocity $\left(= \sqrt{k_B T_\parallel/m}\right)$ |
| $V'_d$ | ............... | Shear in the drift velocity $(V'_d = \partial V_d/\partial x)$ |
| $V'_{di\perp}$ | ............... | Spatial derivative in perpendicular ion drift velocity (or "perpendicular shear") |

# List of Acronyms

**AE-C**    Atmosphere Explorer C

**AGU**     American Geophysical Union

**BGK**     Bhatnagar Gross Krook

**CDEIA**   Current-Driven Electrostatic Ion-Acoustic

**CHAMP**   CHAllenging Minisatellite Payload

**CME**     Coronal Mass Ejection

**CSR**     Coherent Scatter Radar

**DC**      Direct Current

**EISCAT**  European Incoherent Scatter Scientific Association

**EM**      Electromagnetic

**ESR**     EISCAT Svalbard Radar

**FA**      Field-Aligned

**FAC**     Field-Aligned Current

**FAI**     Field-Aligned Irregularities

**FAST**    Fast Auroral Snapshot Explorer

**FFT**     Fast Fourier Transform

**FLR**     Finite Larmor Radius

**HF**      High Frequency

**HILAT**   High Latitude Satellite

**IA**   Ion-Acoustic

**IC**   Ion-Cyclotron

**IF**   Infrared

**IMF**   Interplanetary Magnetic Field

**ISR**   Incoherent Scatter Radar

**MHD**   Magnetohydrodynamic

**MHz**   Megahertz

**NEIAL**   Naturally Enhanced Ion-Acoustic Line

**PDF**   Plasma Dispersion Function

**PFISR**   Poker Flat ISR

**RHS**   Right Hand Side

**SDF**   Spectrum Density Function

**SEP**   Solar Energetic Particles

**SuperDARN**   Super Dual Auroral Radar Network

**TAI**   Transversely Accelerated Ions

**TIU**   Thermal Ion Upflow

**UHF**   Ultra-High Frequency

**UV**   Ultra-Violet

**VHF**   Very-High Frequency

Chapter 1

# Introduction

In this chapter, we describe some elements of the Sun-Earth environment and plasma physics as an introduction to this thesis. To remain concise, we only touch upon a few solar-terrestrial relationship features that influence the properties of the high-latitude ionosphere. Furthermore, we introduce two important remote sensing tools used to study plasma irregularities in the ionosphere: incoherent and coherent scatter radars. In the last section, we provide a description of small-scale irregularities in the high-latitude F-region and we discuss their possible generation mechanisms.

## 1.1 Introduction to the Sun-Earth Environment

### 1.1.1 The Sun as a source of space weather

Space weather encompasses several components of the Sun-Earth system, such as the variable solar wind, sunspots, solar flares, solar energetic particles (SEP), coronal mass ejections (CME), interactions with the Earth's magnetosphere and ionosphere, and the production of the aurora. First, the prime source of space weather is the dynamic Sun. Deep inside the Sun's core, nuclear fusion reactions release enormous amounts of energy being radiated outwards. Closer to the surface, large convection cells generate electrical currents and strong magnetic fields. The Sun continuously releases supersonic streams of highly conductive electrically charged particles, called "solar wind". The solar wind travels in the interplanetary space at speeds of several hundreds km/s, carrying with it the Sun's magnetic field, also called "interplanetary magnetic field" (IMF). The direction of the IMF plays a crucial role in how well the solar wind couples with the Earth's magnetic field and consequently, transfers energy to the Earth.

Besides the solar wind, dark regions often appear on the surface of the Sun, called sunspots. The number of sunspots visible on the surface of the Sun is well correlated with

the approximate 11 years solar cycle. Sunspots are associated with magnetically active regions of the Sun's surface. At times, short-lived explosions can occur near these active regions, discharging radiation across the EM spectrum and high-energy particles. These bursts are called "solar flares". Solar flares are important because they have a direct effect on the properties of the Earth's upper atmosphere. As a result, solar flares can disrupt long-range radio signals and enhance satellite drag. Sometimes flares accelerate the Sun's particles to extremely high energies, propagating at velocities that can reach 80% of the speed of light. These high-energy particles are called "solar energetic particles" (SEP). SEP events are of particular interest because they can endanger human life in outer space and damage electronics.

In addition to solar flares and SEPs, strong magnetic field loops, called prominences, may extend outside the surface of the Sun. At times, these features break apart, releasing formidable amounts of charged matter at speeds that can be much faster than the solar wind. This phenomenon corresponds to a CME. When a CME is directed towards the Earth, it can trigger a geomagnetic storm. Solar wind, sunspots, solar flares, SEPs and CMEs are all components of solar activity, which are driven by the dynamics of the Sun's magnetic field.

### 1.1.2 The Earth's magnetosphere

The Earth's magnetic field is continuously immersed in the solar wind, which carries a large amount of kinetic energy. Similarly to a magnetohydrodynamic (MHD) electrical generator, some of the kinetic energy is converted into electrical energy. This electrical energy is fed into the ionosphere, which acts as a load. The term "magnetosphere" refers to the domain inside of which the motion of charged particles is mainly controled by the Earth's magnetic field. On the sunward side, the magnetosphere is compressed due to the solar wind's kinetic pressure. On the nightside, the magnetosphere is stretched into a long magnetotail that resembles a windsock. The magnetosphere's boundary is called "magnetopause". Figure 1.1 shows several magnetospheric plasma populations and regions.
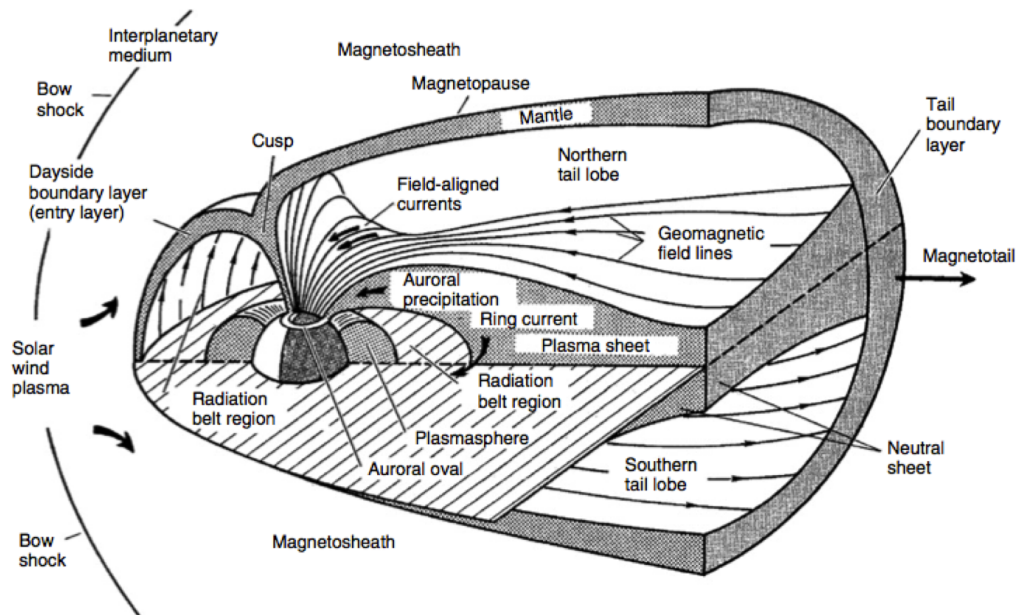
Figure 1.1: Cartoon representation of several regions, plasma populations and current systems in the Earth's magnetosphere. Reproduced from Kelley (2009).

The magnetosphere contains multiple current systems that result from complex solar-wind-magnetosphere interactions. For example, in the magnetotail, the stretched magnetic field is associated with the neutral sheet current, that flows across the neutral sheet in the dawn to dusk direction. The neutral sheet is also the region in which open field lines may reconnect to form closed field lines that convect back to the earth. This topic will be further discussed in more detail in Sect. 1.1.4.

### 1.1.3   The Earth's ionosphere

Besides the outflow of highly energetic particles, the Sun continuously emits electromagnetic (EM) radiation, ranging from the short wave X-rays up to the longer radio waves. Most of the emitted energy is concentrated in the infrared (IR), visible and ultra-violet (UV) portion of the EM spectrum, providing light and heat on Earth. The extreme UV and X-ray parts of the solar radiation spectrum are responsible for ionizing the upper part of the Earth's atmosphere, between approximately 60-1000 km of altitude. This region, known as the ionosphere, is comprised of free electrons, different type of molecular and atomic
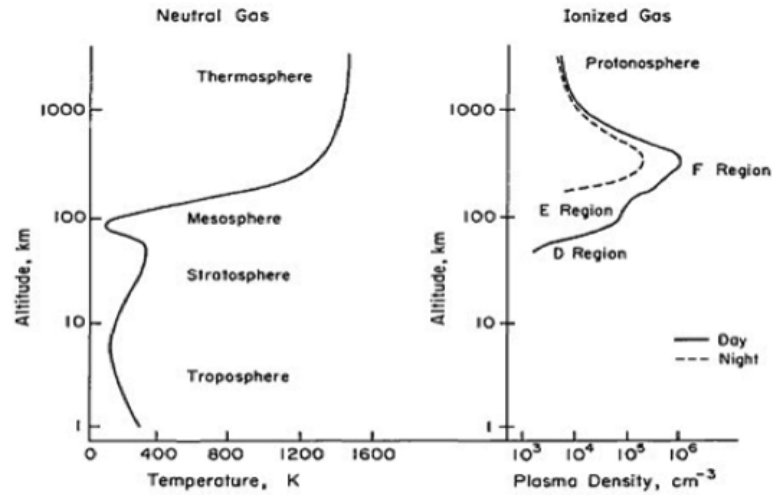
Figure 1.2: Typical altitude profiles of neutral atmospheric temperature and ionospheric plasma density with the various layers identified. Reproduced from Kelley (2009).

ions as well as neutral particles. On a macroscopic scale, the ionosphere contains an equal number of ions and electrons, a property named "quasineutrality".

The various ionospheric layers are shown in Fig. 1.2, along with neutral gas temperatures. It should be noted that the typical plasma density "nose shape" vertical distribution profile portrayed in Fig. 1.2 is representative of mid-latitudes. The D-region (60-90 km) contains small electron densities and large neutral densities. It is the most complex chemically, including ion production, recombination and transport processes that are not fully understood yet. Also, its ionization level is so low that its properties differ a lot compared with the weakly collisional E-region (105-160 km) and the quasi-collisionless F-region. $NO^+$ and atomic oxygen dominate the plasma below about 150 km (E-region), whereas the F-region comprises mostly of atomic oxygen (see Fig. 1.3). The F-region is further divided into two sub-regions: F1 (160-180 km) and F2 (with a peak at approximately 300 km).

In general, the ion temperature is lower than the electron temperature, but larger than the neutral one. Figure 1.4 shows typical temperature profiles for neutrals, ions and electrons between 100 and 600 km. All ionospheric layers are highly variable depending on
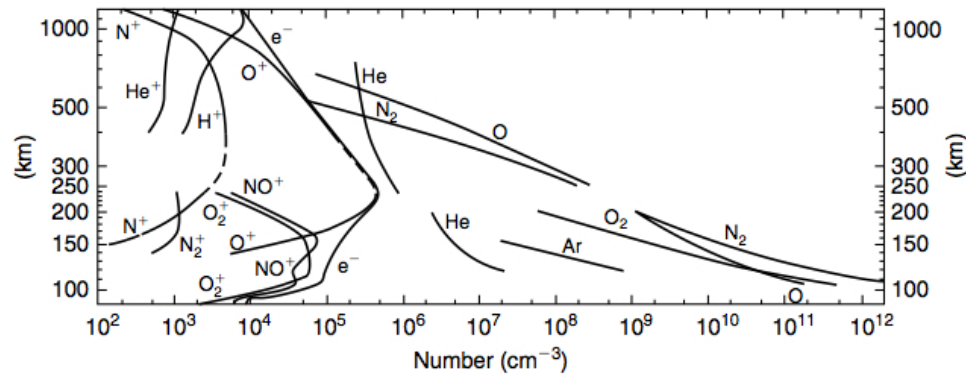
Figure 1.3: Typical altitude profiles of number density for the most common ion and neutral species, together with the electron density profile. Reproduced from Kelley (2009).

seasons and solar activity. Diurnal variations make the D, E and F1 regions vanish at night, whereas the F2 region tends to persist since atomic oxygen has a much longer lifetime than molecular ions (see right hand side of Fig. 1.2). At high-latitudes, the plasma density profile can differ from the one presented in Fig. 1.2, one reason being that solar radiation is not the only source of plasma. Indeed, at high-latitudes, the ionosphere is strongly coupled with the magnetosphere and consequently, is strongly affected by the solar-terrestrial environment. Energetic particles precipitating along the magnetic field lines and into the neutral gas can also be an important source of ionization at high-latitudes. In the auroral zone, the interaction of energetic particles with those of the upper atmosphere emits green, red and sometimes violet light, a phenomenon known as auroral borealis (northern hemisphere) and australis (southern hemisphere). On global scales, the aurora takes the form of ovals centered on the Earth's magnetic poles. The region encircled by the auroral oval is the polar cap.

## 1.1.4 Electrical coupling between the ionosphere, magnetosphere and solar wind

The ideal geometry that enhances electrical currents closure in the ionosphere occurs when the vertical component of the IMF ($B_z$) points in the southward direction. Indeed, magnetic field merging on the dayside magnetosphere is most effective when $B_z$ and the Earth's magnetic field point in opposite directions. On the dayside magnetopause, the neutral points
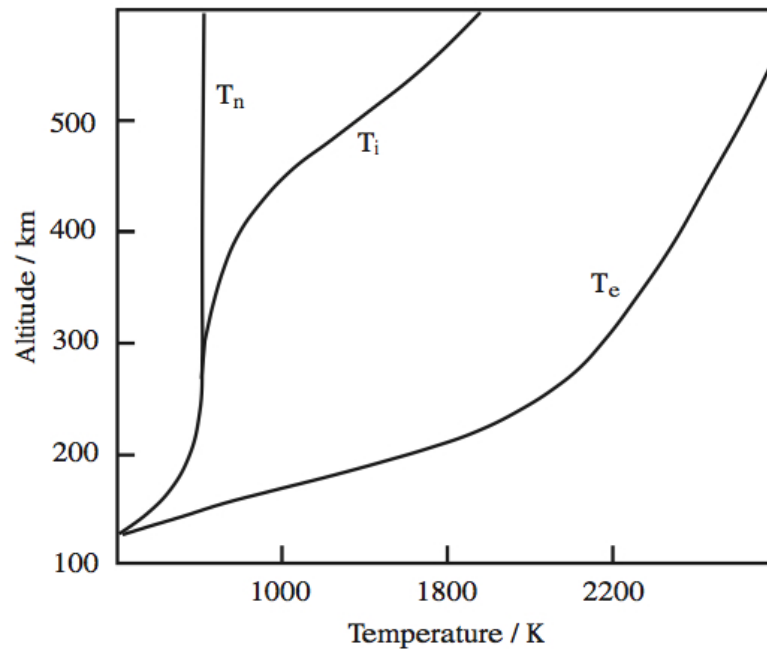
Figure 1.4: Representative altitude profiles of ion, electron and neutral temperatures between 100 and 600km. Reproduced from Brekke (2012).

where the magnetic field is nul map down along magnetic field lines to near-Earth regions at a geomagnetic latitude of $\pm 78°$. As a result, solar wind particles can then easily penetrate into these ionospheric regions that are named "polar cusps" or "clefts" (see Fig. 1.1).

After magnetic reconnection on the dayside magnetopause, the newly created open field lines have one foot attached to the Earth (associated with the cusp and polar cap) and the other one being swept antisunward with the solar wind, resulting in magnetic flux transfer to the magnetotail. This process is illustrated in Fig. 1.5. The numbers indicate the temporal sequence of the magnetic field lines reconnection and movement. Magnetic field reconnection can also occur in the neutral sheet (magnetotail), forming closed field lines that convect back in the sunward direction. In general, the auroral oval corresponds to the boundary between open and closed magnetic field lines.

For an ideal, magnetized and collisionless (with infinite conductivity) solar wind plasma, MHD theory dictates that its electric field with respect to a fixed frame of reference is
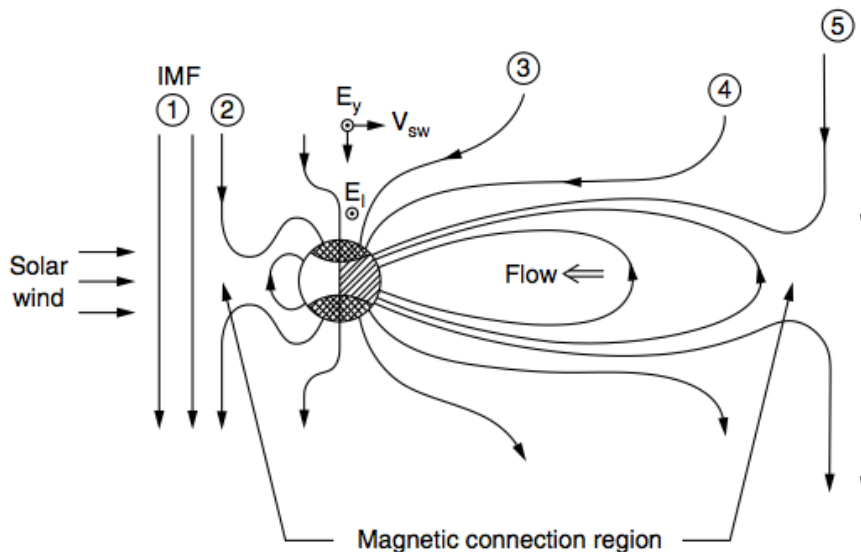
Figure 1.5: Cartoon representation of IMF-magnetosphere reconnection processes when $B_z$ is south. The view is in the noon-midnight plane. $E_y$ is the interplanetary electric field and $E_I$ is the electric field mapped into the ionosphere down the magnetic field lines. Reproduced from Kelley (2009).

$\mathbf{E}_{sw} = -\mathbf{V}_{sw} \times \mathbf{B}_{sw}$ (Kelley, 2009), where the subscript "sw" refers to the solar wind. When $B_z$ is pointing south, the interplanetary electric (indicated as $E_y$ in Fig. 1.5) is aligned with the dawn-to-dusk direction across the magnetosphere. Since the magnetic field lines can usually be treated as equipotentials in steady-state conditions (not applicable in auroral acceleration zones where parallel electric fields sometimes exist), this electric field maps down into the ionosphere ($E_I$ in Fig. 1.5). Consequently, the same electric field drives the ionospheric F-region plasma in the antisunward direction at the $\mathbf{E} \times \mathbf{B}$ speed since collisions with neutrals are infrequent enough both for electron and ions. This antisunward drift combined with the sunward convection that occurs after reconnection in the magnetotail leads to the two cells ionospheric convection pattern that can be tracked with the Super Dual Auroral Radar Network (SuperDARN) of HF radars from the coherent scattering of F-region plasma irregularities (more on that in Sect. 1.3.3). A representation of the two cells convection pattern along with ionospheric electric fields is shown in Fig. 1.6. In this figure, $E_a$ denotes the electric field in the auroral zone and $E_{pc}$ is the polar cap electric field.
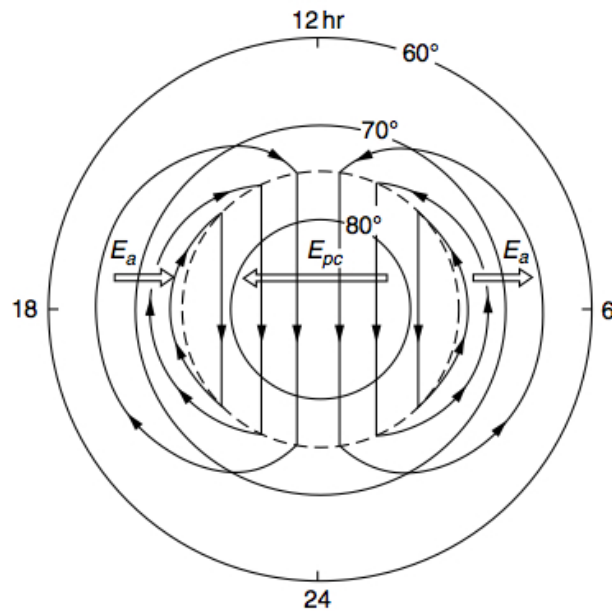
Figure 1.6: Representation of the ionospheric two cells convection pattern in the northern hemisphere and the electric fields in the polar cap $(E_{pc})$ and auroral zone $(E_a)$. Reproduced from Kelley (2009).

In the E-region, the ionosphere is a resistive medium due to different collision and gyro frequencies for ions and electrons and consequently, horizontal currents can flow. In accordance with Ohm's law, the electrical current is linked to the electric field by the equation

$$\mathbf{J} = \sigma \cdot (\mathbf{E} + \mathbf{U} \times \mathbf{B}) \tag{1.1}$$

where $\sigma$ is the ionospheric conductivity tensor, $\mathbf{U}$ is the neutral wind velocity and $\mathbf{B}$ is the magnetic field. Ignoring the presence of neutral wind, the electric field will drive an ionospheric current. In this case, the ionosphere acts as a load dissipating some of the electrical energy originating from the solar wind (generator). From the continuity equation, any divergences in ionospheric perpendicular currents will result in field-aligned currents (FAC), also called "parallel" or "Birkeland" currents. FACs play an essential role in linking the solar wind-magnetosphere system with the ionosphere. FACs have been categorized as Region 1 and Region 2 currents, as shown in Fig. 1.7. This figure represents the most stable FAC systems during quiet (a) and more active (b) magnetospheric conditions. The
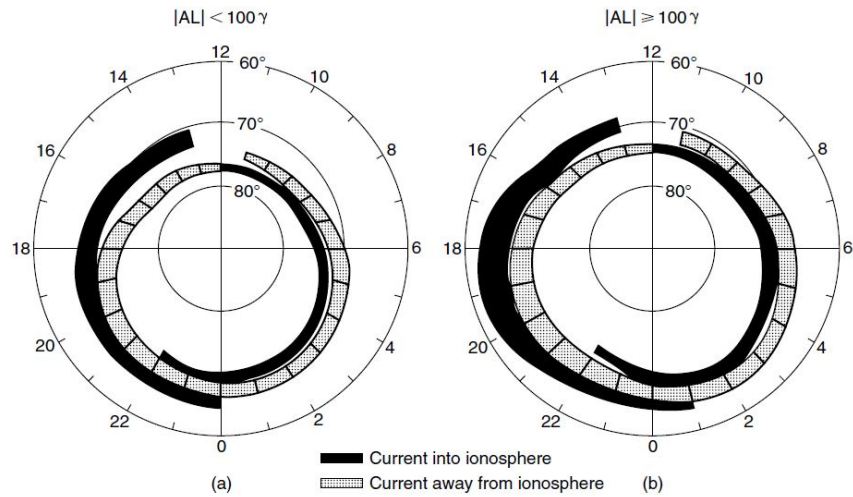
Figure 1.7: Topside view (looking from above the Earth toward the magnetic pole) of field-aligned currents when the IMF has a southward component. The inner ring is termed Region 1 and the outer ring Region 2. Left figure (a) corresponds to a quiet magnetosphere and (b) when it is more disturbed. Reproduced from Kelley (2009) [original source: Iijima and Potemra (1978)].

inner ring corresponds to Region 1 currents. Region 1 currents link the poleward portion of the auroral oval and the polar cap to the magnetosheath, solar wind or the boundary layer near the magnetopause (Kelley, 2009, page 386). Region 2 currents link the equatorward edge of the auroral oval with the inner magnetosphere. The presence of FACs carried by thermal particles can be a source of plasma instabilities in the high-latitude ionosphere, provided that the magnitude is large enough. The topic of plasma instability is introduced in Sect. 1.2.3.

## 1.2   Elements of Plasma Physics

### 1.2.1   Debye shielding and collective effects

As mentioned previously, for a plasma to be quasineutral, there must be a nearly equal number of positive and negative charges per unit volume. The Debye length ($\lambda_D$) is a characteristic scale length over which a balance is achieved between the thermal particle energy and the electrostatic potential energy resulting from any charge separation (Baumjohann

and Treumann, 1997, chapter 2). In essence, it provides a measure of the average screening distance of the electrostatic potential associated with a test charge. For scales larger than the Debye length, the plasma is quasineutral because of the electrons clouding effect, while for scale lengths smaller than $\lambda_D$, the plasma cannot be considered quasineutral anymore. The Debye length is a function of temperature, $T$, and density, $n$, and can be written as

$$\lambda_D = \sqrt{\frac{\varepsilon_o k_B T}{ne^2}} \tag{1.2}$$

where $\varepsilon_o$ is the free space permittivity, $k_B$ is the Boltzmann constant and $e$ is the elementary charge.

As far as incoherent scatter radars (ISR) are concerned, the Debye length turns out to be an important plasma characteristic parameters since it sets the minimum radar wavelength required to observe scattering from wave fluctuations, or collective effects. In this limit $k\lambda_D \ll 1$, or equivalently $2\pi\lambda_D^2/\lambda^2 \ll 1$, the ISR spectrum would contain information about the plasma as a whole. By contrast, the limit $k\lambda_D \gg 1$ would correspond to purely incoherent scattering from the free electrons. In this case, the plasma would not be seen to be quasineutral. In addition, in the low-frequency limit, ions will oscillate with the electrons despite their much larger inertia. To that extent, one can envisage the plasma to behave as a fluid with collective behaviors where only the effect of forces on fluid elements is taken into account. On the other hand, in the small wavelength limit, the plasma can be described as a collection of individual particles and one must use the kinetic theory.

### 1.2.2 Kinetic plasma theory

A complete microscopic description for a plasma would involve solving equations of motion and Maxwell equations for all particles and fields. Because of the enormous amount of calculations that would be required, kinetic theory uses probability distribution functions expressed in the velocity-configuration phase space. The number of particles per unit volume is a function of spatial coordinates $(x,y,z)$, velocity coordinates $(v_x, v_y, v_z)$ and time $(t)$. Kinetic theory relies on the Boltzmann equation, given by

$$\frac{\partial f_j}{\partial t} + \mathbf{v} \cdot \frac{\partial f_j}{\partial \mathbf{r}} + \mathbf{a} \cdot \frac{\partial f_j}{\partial \mathbf{v}} = \left( \frac{\delta f_j}{\delta t} \right)_c \tag{1.3}$$

where $f_j = f_j(\mathbf{r}, \mathbf{v}, t)$ is the average distribution function of species $j$, $\mathbf{a} = q_j/m_j (\mathbf{E} + \mathbf{v} \times \mathbf{B})$ is the acceleration and $m_j$ and $q_j$ are the mass and charge of species $j$, respectively. The right hand side (RHS) of Eq. (1.3) is a collision term. When collisions are negligible, then the RHS can be set to zero and the resulting equation is called "the Vlasov equation".

As per linear stability theory, we consider that the plasma fluctuations (perturbed quantities) are small compared to the unperturbed ones. Hence, the distribution function can be expressed as

$$f_j = f_{0j} + f_{1j} \tag{1.4}$$

where $f_{0j}$ is the unperturbed average distribution function of a constant background and $f_{1j}$ is the perturbed average distribution function of species $j$. Similarly, the fields can be separated into an unperturbed and a perturbed quantity such that

$$\mathbf{E} = \mathbf{E}_0 + \mathbf{E}_1 \tag{1.5}$$

and

$$\mathbf{B} = \mathbf{B}_0 + \mathbf{B}_1 \tag{1.6}$$

where $\mathbf{E}_0$ and $\mathbf{B}_0$ are the unperturbed quantities while $\mathbf{E}_1$ and $\mathbf{B}_1$ are the perturbed quantities. Substituting Eq. (1.4) into (1.3) and using the electrostatic approximation

$$\mathbf{E}_1 = -\vec{\nabla}\phi_1 \tag{1.7}$$

where $\phi_1$ is the perturbed electrical potential, and $\mathbf{B}_1 = 0$, keeping only the linear terms and assuming a quasi-neutral state with vanishing background electric field ($\mathbf{E}_0 = 0$), Eq. (1.3) can be written as

$$\frac{\partial f_{1j}}{\partial t} + \mathbf{v} \cdot \frac{\partial f_{1j}}{\partial \mathbf{r}} - \frac{q_j}{m_j}\vec{\nabla}\phi_1 \cdot \frac{\partial}{\partial \mathbf{v}}f_{0j} + \frac{q_j}{m_j}(\mathbf{v} \times \mathbf{B_o}) \cdot \frac{\partial f_{1j}}{\partial \mathbf{v}} = \left(\frac{\delta f_{1j}}{\delta t}\right)_c. \tag{1.8}$$

For electrostatic modes, a Fourier/Laplace analysis in space/time of Eq. (1.8), combined with Poisson's equation

$$\nabla^2 \phi_1 = -\frac{1}{\varepsilon_0}\sum_j n_j q_j \int f_{1j} d^3\mathbf{v} \tag{1.9}$$

yields the normal modes of the plasma through a dispersion equation relating complex frequency ($\omega = \omega_R + i\gamma$) with the wavenumber $k$, where $\omega_R$ and $\gamma$ are the real and imaginary

part of the frequency, respectively. Before proceeding, an appropriate distribution function must be selected.

Maxwellian distribution functions are used to represent particle populations in thermal equilibrium. The one-dimensional Maxwellian distribution function ($f_{0m}$) as a function of velocity component $u$ can be written as

$$f_{0m}(u) = \sqrt{\frac{m}{2\pi k_B T}} \exp\left(-\frac{mu^2}{2k_B T}\right).$$
(1.10)

In addition, temperature anisotropies may be encountered in space plasmas when there is a preferred direction, for instance, a strong magnetic or electric field. At times, the three-dimensional velocity distribution function depends solely on $v_\perp$ and $v_\parallel$. As a result, the equilibrium distribution function can be modelled as a product of two Maxwellians. In this case, the resulting distribution is referred to as "bi-Maxwellian". The bi-Maxwellian distribution function ($f_{0bm}$) can also be extended in the case of a distribution drifting along the magnetic field line at a velocity $V_d$, which is given by (Baumjohann and Treumann, 1997, chapter 6)

$$f_{0bm}(v_\perp, v_\parallel) = \frac{1}{T_\perp T_\parallel^{1/2}} \left(\frac{m}{2\pi k_B}\right)^{3/2} \exp\left(-\frac{mv_\perp^2}{2k_B T_\perp} - \frac{m(v_\parallel - V_d)^2}{2k_B T_\parallel}\right)$$
(1.11)

where $v_\perp$ and $v_\parallel$ are the perpendicular and parallel velocities, respectively. The perpendicular and parallel thermal velocities are defined respectively as $v_{\parallel t} = \sqrt{k_B T_\parallel/m}$ and $v_{\perp t} = \sqrt{k_B T_\perp/m}$. Finally, for consistency with the kinetic definition of temperature, the total temperature can be expressed as a function of $T_\perp$ and $T_\parallel$ (Schunk and Nagy, 2004)

$$T = \frac{1}{3}(T_\parallel + 2T_\perp).$$
(1.12)

In the theory of linearized waves or oscillations in a hot plasma, a function of complex argument named "the plasma dispersion function" is often used whenever the velocity distribution function is taken to be Maxwellian. This function is defined as (Fried and Conte, 1961)

$$Z(\rho) = \pi^{-1/2} \int_{-\infty}^{\infty} \frac{e^{-t^2}}{t - \rho} dt$$
(1.13)

for Im $\rho > 0$ and as the analytic continuation for Im $\rho \leq 0$, where $\rho$ is the argument of the plasma dispersion function (PDF). Analytic continuation is related to the so-called Landau contour "C" in the integral of Eq. 1.13. More information on the integration along the Landau contour and the causality condition can be found in several plasma physics textbooks (for example, see Krall and Trivelpiece, 1973).

### 1.2.3 Plasma instabilities

Several textbooks such as Treumann and Baumjohann (1997) cover the subject of plasma instabilities extensively. For plasma instabilities to arise, there must be a positive feedback mechanism, or a source of free energy, which allows an initial perturbation of the medium to grow to larger amplitudes with time. The free energy inputs can produce inhomogeneities or gradients in the plasma configuration, or it can take the form of relative thermal drifts between particles species, electric fields or temperature anisotropies. Consequently, the plasma can attempt to redistribute this additional energy and to recover an equilibrium state by generating plasma instabilities.

Plasma instabilities can be categorized as macroinstabilities or microinstabilitites. A macroinstability, which can be described in terms of macroscopic (fluid) equations in the configuration space, produce unstable arrangement of the plasma on large scales. An example of macroinstability is the "E×B instability", which requires an ambient perpendicular density gradient and a perpendicular electric field in order to be triggered. Another example is the "Kelvin-Helmholtz" instability that results from gradients in drift velocity. On the other hand, microinstabilities occur in the velocity space and depend on the shape of the distribution function. This thesis is mostly concerned with ion-acoustic (IA) type of microinstabilities that includes electron-ion thermal relative drifts, ion velocity shears and ion temperature anisotropies. In addition to IA modes, ion-cyclotron (IC) modes are also included in the calculation of ISR spectra for magnetized plasmas (see Chap. 4).

For selected parameters that can be sources of free energy, a threshold value must be exceeded before an instability can take place. Linear theory allows to determine whether

a plasma is stable to small perturbation amplitudes. Stable plasmas will see their perturbations eventually damped. However, when the threshold conditions are surpassed, the wave amplitude will grow with time until some dissipation mechanisms act to quench the plasma. To sum up, linear theory provides a tool to assess the threshold conditions for the development of small amplitude fluctuations.

The high-latitude ionosphere is continuously provided with mass, momentum and energy of magnetospheric or solar-wind origin. As a result, a variety of plasma waves and instabilities can be excited in the high-latitude ionosphere. Instabilities as well as other processes create structure in the plasma density, or irregularities. In particular, it is well established that plasma instabilities play an important role in the generation of small and intermediate scale irregularities (scales are defined in Sect. 1.4). Irregularities can be pictured as alternating regions of plasma density enhancements and depletions. These structures have scale sizes ranging from tens of kilometers down to centimeters and have been observed at all heights. See Fejer and Kelley (1980) for a comprehensive review of irregularities and Tsunoda (1988) for a review of high-latitude F-region irregularities. They are sometimes referred to as patches, blobs, plumes or bubbles depending on the regions and scales involved. Such irregularities can be studied using incoherent or coherent scatter radars.

## 1.3 Incoherent and Coherent Scatter Radars

Both incoherent scatter radars (ISR) and coherent scatter radars (CSR) are designed to detect echoes from collective scattering in the ionosphere. ISRs operate at higher frequencies and transmit much more power than CSRs. The intent of this section is to describe how these two techniques can be useful to study ionosphere irregularities.

### 1.3.1 Elements of basic radar theory

Radar systems are used extensively for the detection and location of hard targets. The EM energy that is reflected and returned to the radar allows the determination of the target lo-

cation (range) and also, by comparing the received echo signal with the transmitted signal, other target-related information can be inferred. From the fundamental radar range equation, the distance factor is $1/r^2$ to reach the target and $1/r^2$ from the target back to the radar, so the received power varies as $1/r^4$ (The basic radar equation can be found, for example, in Skolnik, 2003, page 6).

$$P_r = \frac{P_t G A_e \sigma_s}{(4\pi)^2 r^4} \tag{1.14}$$

In Eq. (1.14), $P_t$ and $P_r$ are the transmitted and received power respectively, $G$ denotes the transmit gain, $A_e$ is the antenna effective area, $\sigma_s$ is the target cross-section and $r$ is the range. For the incoherent scatter case, the target is a volume of ionosphere plasma and consists of multiple scatterers which "fill up" the radar beam. In this case, the ionosphere consists of a "soft target" and the scattering will depend on the radar operating frequency. The backscattering cross section for "beam filling" echoes can be written as $\sigma_s = \eta V$ where $\eta$ is the backscattering cross section per unit volume $[m^2/m^3]$ and $V_s$ is the scattering volume. The scattering volume $V$ can be approximated as $\approx \Omega r^2 \Delta r$ (Kelley, 2009, App.A), where $\Omega$ is the beam antenna solid angle in steradians and $\Delta r = c\tau_p/2$ defines the range resolution of the measurement ($\tau_p$ is the radar pulse length and $c$ is the speed of light). Since the gain of the main beam is inversely proportional to the solid angle illuminated by the antenna $G = 4\pi/\Omega$, Eq. (1.14) reduces to

$$P_r = \frac{P_t A_e \eta \Delta r}{4\pi r^2}. \tag{1.15}$$

Hence, in the case of beam filling targets, the received power varies according to $1/r^2$. For coherent scatter radars, received echoes are not purely point targets, but they are not likely to be beam filling either (in general, they tend to be extremely sensitive to the aspect angle). As a result, we expect a variation between $1/r^2$ and $1/r^4$ depending on the nature of turbulence (St-Maurice and Hamza, 2009). Consequently, the scattering cross-section for coherent backscatter is typically $10^4$–$10^9$ times greater than incoherent scattering.

## 1.3.2   Incoherent Scatter Radars (ISR)

Incoherent scattering is a powerful technique to estimate ionospheric macroscopic state parameters provided that the plasma is near thermal equilibrium. ISRs transmit large amounts

of power (in the megawatt range) to the ionosphere in order to detect weak signals (in the picowatt range) from thermal and semi-coherent plasma density fluctuations along the radar line-of-sight. ISRs operate in the very-high frequency (VHF: 30-300 MHz) and ultra-high frequency (UHF: 300-3000 MHz) portions of the EM spectrum. Such radar waves are almost unattenuated by the ionosphere however, a very small amount of energy is backscattered by the electrons which act as small dipole antennas. Although most of the scattering comes from the electrons, when the probing radar half-wavelength is larger than the Debye length (Eq. 1.2), the presence of ions influences the motion of electrons due to electrostatic forces and introduces some degree of coherence. In other words, electrons scatter the radar signals, but the spectral properties are influenced by plasma waves propagating along the radar beam. This semi-coherent scattering is also called "collective scattering". The principal wave components are IA waves and electron plasma (Langmuir) waves. Hence, a typical ISR spectrum comprises of two features: the ion line and a pair of electron lines (or plasma lines). The ion line consists of a double humped shape centered near the transmitted frequency, with the two humps offset by the IA wave frequency seen by the radar. It can be pictured as two broadened overlapping lines corresponding to Landau damped IA waves propagating away and toward the radar probing direction (for a monostatic radar). Figure 1.8 shows what typical ion lines look like for various plasma bulk parameters. The electron (plasma) lines would be located at much higher frequencies (in the MHz range) and would be much narrower.

As alluded to before, an ISR is only sensitive to plasma fluctuations matching the Bragg conditions for scattering (more on Bragg scattering in Sect. 1.3.3). For a monostatic radar with a probing wavenumber $k_0$, the corresponding wave number matching Bragg condition for coherent scattering is $k = 2k_0 = 2\pi/\lambda$ where $k$ is the Bragg wavenumber and $k_0$ is the radar incident wavenumber. In other words, monostatic radars detect only one spatial Fourier component plasma density fluctuations with a wavelength equal to half the radar incident wavelength $\lambda = \lambda_0/2$ and propagating along the radar probing direction (or parallel and anti-parallel to $\mathbf{k}$).

A large amount of information can be extracted from the ISR measured signal spectrum. Using a statistical approach, the theoretical spectra can be fit to the ISR raw data in the form of autocorrelation functions in order to infer the main ionosphere state parameters. For this fitting procedure to be valid, it is assumed that the plasma scattering volume is homogeneous, near thermal equilibrium and stationary over the whole integration time. These assumptions are not always fulfilled, for instance when the plasma is driven out of thermal equilibrium. In other words, when the instability threshold conditions are exceeded, the calculation of ISR spectra becomes meaningless. On the other hand, when the stability, homogeneity and stationarity conditions are met, the main inferred parameters are the electron density, ion composition, ion and electron temperatures and the plasma drift velocity along the radar line-of-sight. The electron density $n_e$ can be found from the total back-scattered power, or the integral under the curve. The temperature ratio $T_e/T_i$ can be inferred from the peak-to-valley ratio of the ion line (since the damping of IA waves depends on $T_e/T_i$). The ion temperature to mass ratio $T_i/m_i$ can be deduced from the width of the ion line. If $m_i$ is known or assumed, then $T_i$ and $T_e$ can be estimated. We illustrate some effects associated with varying the previous parameters $(n_e, T_e/T_i, T_i)$ on the ion line in Fig. 1.8. These calculations were done in the case of Poker Flat ISR (449MHz). Finally, the mean Doppler shift yields the line-of-sight plasma drift velocity. In this case, the whole line would simply be upshifted or downshifted by the Doppler frequency without changing the actual shape of the line.

The shape of the ISR spectrum for a stable plasma can also be modified by additional parameters such as electron-ion relative drifts or collisions. The effect of both negative and positive relative drifts is shown in Fig. 1.9 for the Poker Flat ISR operating at 449MHz. In this figure, $V_{de}$ is the parallel electron-ion drift and $C_s$ is the ion-acoustic speed of the medium. Indeed, in the presence of an electron-ion relative drift, either shoulder of the ion feature is enhanced depending on the sign of the parallel drift.

The general expression for the ISR scattering spectrum function was independently derived by several authors in the 60's using different approaches and all leading to similar re-
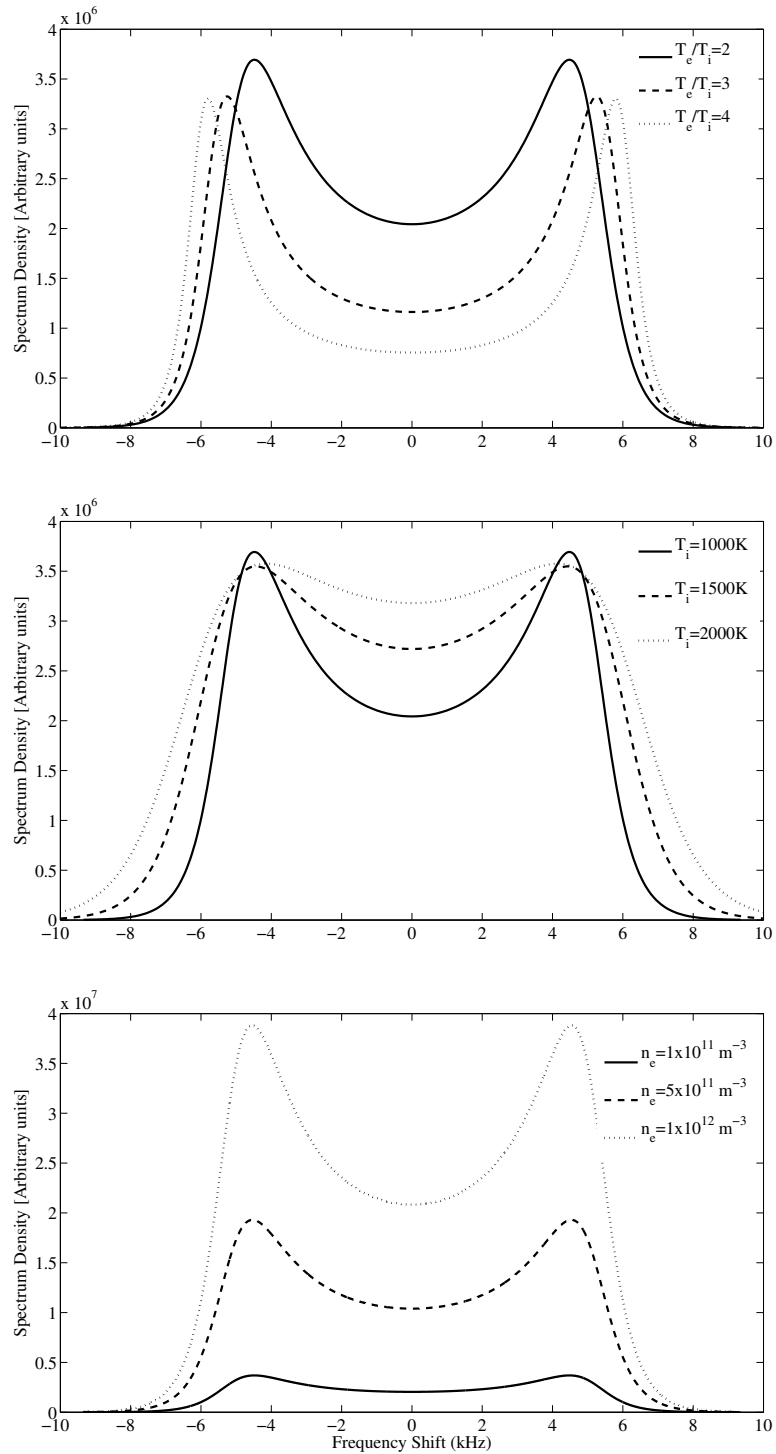
Figure 1.8: Effects of ion-to-electron temperature ratio $T_e/T_i$ (upper panel), ion temperature $T_i$ for a known ion mass (middle panel) and electron density $n_e$ (lower panel) on the ion line calculated in the case of Poker Flat ISR (449MHz) and for a $O^+$ plasma.
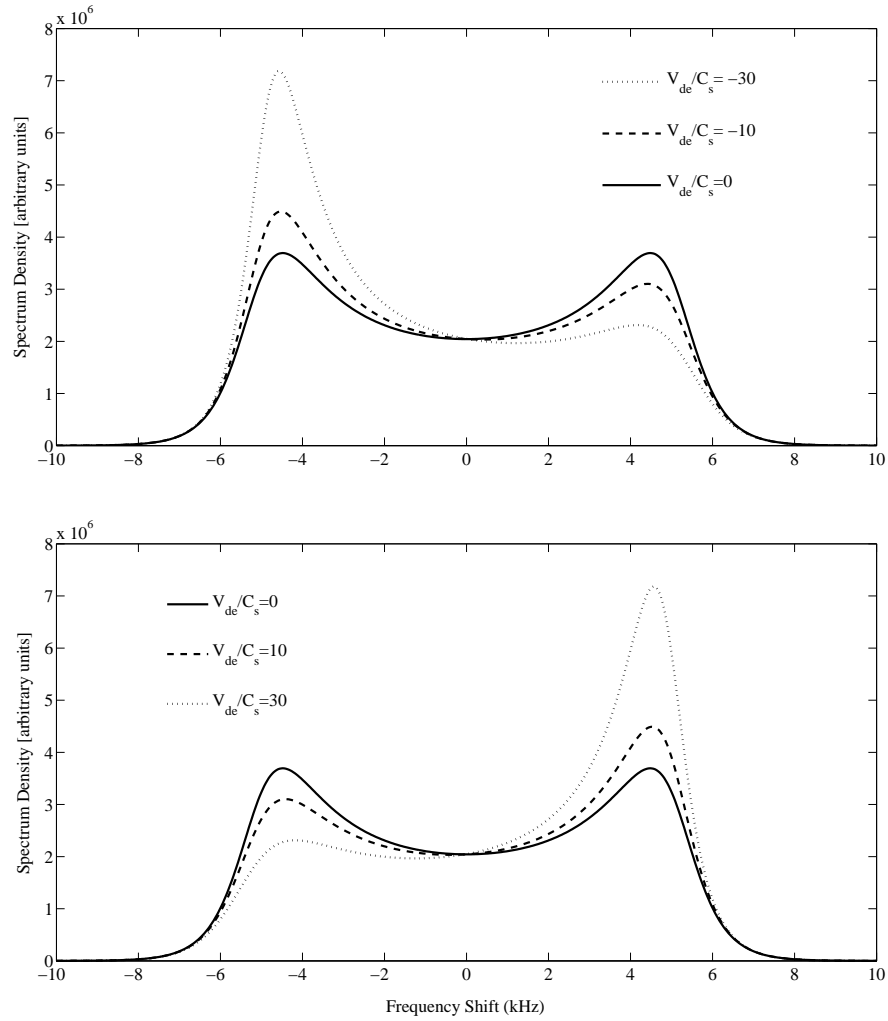
Figure 1.9: Effects of a positive and negative (parallel and anti-parallel) electron drift $V_{de}/C_s$ (with respect to the ions) on the ion line calculated in the case of Poker Flat ISR (449MHz) and for a $O^+$ plasma. The upper panel shows how the left shoulder is enhanced with negative drifts and the lower panel shows how the right shoulder is enhanced with positive drifts.

sults (Dougherty and Farley, 1960, Fejer, 1960, Salpeter, 1960). Evans (1969) and Beynon and Williams (1978) provide in-depth reviews of the development of the technique and the basic ISR theory involved. In this work, we use the plasma kinetic formalism initially developed by Fejer (1960) that involves the Vlasov equation to establish the equilibrium microscopic density fluctuations. Specifically, we closely follow the detailed presentation of Froula *et al.* (2010).

Afterwards, both Farley *et al.* (1961) and Fejer (1961) considered the effects of a uniform magnetic field in the calculation of the spectral power density. Indeed, they found that the total scattered power is not affected by the magnetic field. Moreover, they showed that the magnetic field has a significant effect on the shape of the spectrum only if the incident radar beam is very nearly perpendicular to the magnetic field lines. For this reason, it has been generally believed that gyroresonances effects on ISR spectra are negligible unless the wave vector is near perpendicular to the magnetic field. The effects of a magnetic field on ISR spectra is further discussed in Chap. 4.

### 1.3.3 Coherent Scatter Radars (CSR)

CSR's operate in the high-frequency (HF: 3-30 MHz) and VHF parts of the electromagnetic spectrum. CSR's detect coherent scattering from enhanced non-thermal plasma fluctuations or waves with amplitudes beyond thermal levels. Stated differently, it "sees" plasma instabilities or turbulence. The three measurements of interest are the spectral power, the Doppler shift and the Doppler spread.

As it was alluded to previously, due to conservation of momentum considerations, the irregularity wavelength observed by a monostatic radar is one half the transmitted wavelength. This condition is referred to as "Bragg" scattering. Irregularities tend to naturally align themselves along the magnetic field ($\mathbf{B}_0$) because electrons are able to move freely along $\mathbf{B}_0$ and short-circuit parallel electric fields, which is not the case for electric fields that are perpendicular to $\mathbf{B}_0$. Since the optimal observing geometry for Bragg scattering is perpendicular to $\mathbf{B}_0$, CSRs are very sensitive to the aspect angle. This perpendicular geom-

etry allows reinforced scattering and consequently, the detection of strong coherent echoes. For this reason, HF radars prove to be convenient at high-latitudes owing to the fact that refraction can bend HF rays as they propagate through the ionosphere. Consequently, HF rays can hit field-aligned irregularities (FAI) in a direction perpendicular to the magnetic field. By using Doppler velocity measurements from two radars, a 2D vector quantity can then be estimated. For example, the SuperDARN network of HF radars is commonly used to map the high-latitude convection patterns of both hemispheres through coherent echoes from F-region FA irregularities in the 10-20 meters band (Greenwald *et al.*, 1995).

ISR systems can also detect non-thermal waves if they are present. For example, coherent echoes can often be detected when the ISR pointing direction is parallel to $\mathbf{B}_0$ or at large angles with respect to the direction perpendicular to $\mathbf{B}_0$. In such cases, the irregularities are near field-perpendicular. In this case, the power level is enhanced by more than one order of magnitude in either or both IA peaks, well above thermal fluctuation levels. This phenomenon is commonly named "naturally enhanced ion-acoustic line", or NEIAL, in the litterature. This topic is further discussed in Sect. 2.2 and Sect. 2.2.3. ISRs have also occasionally detected F-region coherent echoes when the radar was pointing in a direction perpendicular to $\mathbf{B}_0$. For example, Foster (1990) observed field-aligned coherent echoes at 300 km that looked similar to that which would be expected in the E-region (Foster, 1990, St-Maurice, 2003). Interestingly, these field-aligned coherent echoes were located in between field lines along which NEIALs were also detected.

## 1.4   Small-Scale Irregularities in the High-Latitude F-Region

In this section, we further narrow the scope of the introduction to small-scale irregularities in the high-latitude F-region in order to transition to the following chapter. This summary is largely based on Sect. 10.3 of the textbook by Kelley (2009) and Sect. 3 of St-Maurice and Hamza (2009). According to the former author, small-scale wavelengths are defined to be smaller than 100 meters. This definition encompasses scales accessible to radars, i.e. from centimeter up to decameter wavelengths, which allows them to be studied with the

help of incoherent and coherent scatter radars. Furthermore, small-scale irregularities are important to understand since they are known to produce amplitude and phase scintillations of radio signals owing to diffractive scattering (Hunsucker and Hargreaves, 2002). This effect, which is particularly severe in auroral zones, results in trans-ionospheric radio signals fading.

Most intermediate-scale irregularities (scales ranging from approximately 100 m to 30 km) in the high-latitude F-region are believed to be generated by the "E×B instability" (also named "interchange" or "gradient-drift" by some authors). As mentionned previously, this finger type of instability requires an ambient perpendicular density gradient and a perpendicular electric field to be generated. However, this macroinstability is typically stable for wavelengths smaller than 10 meters (Kelley, 2009, page 510), unless stronger perpendicular electric fields than average are present. As a result, it would be difficult to detect wavelengths smaller than 10 meters directly produced by this mechanism. In addition to the gradient-drift, the "current convective" instability has also been invoked (Ossakow and Chaturvedi, 1979) when in the presence of parallel electron-ion relative drifts. Since FACs are common at high-latitudes, the current convective instability is competing with the gradient-drift despite the fact that it requires large parallel current densities for the onset of instability.

Small-scale irregularities (centimeters to decameters) can be the consequence of turbulent mixing, in other words, the cascade of larger structures into smaller ones. In spite of the fact that cascading processes are seen to play an important role in the generation of decameter structures in the F-region, as seen with in-situ rockets (for example, see Kelley, 2009), it does not imply that direct growth processes are not also involved. To explain these small-scale irregularities in terms of direct generation mechanisms, one has to turn to microscopic instability theories.

### 1.4.1 The Doppler shift

From coherent echoes, the plasma E×B drift velocity along the radar look direction can be inferred by assuming that the irregularities are field-aligned and that their phase speed is zero (or small) in the E×B frame of reference. Stated differently, the irregularities are frozen into the plasma drift and are used as tracers of the plasma E×B drift velocity. This assumption is believed to be valid at HF because the preferred instability mechanisms (E×B instability, current-convective instability) operating at such wavelengths have low phase velocities (Kelley, 2009, page 510). In fact, observations have been made to verify the assumption of F-region plasma waves drifting with the plasma using ISRs and CSRs illuminating almost the same ionospheric volumes. For example, the early work of Ruohoniemi *et al.* (1987) provided data comparison between the HF radar at Goose Bay and the ISR at Sondre Stromfjord. The initial comparison exhibited good agreement between the irregularities Doppler velocities (measured by HF radar) and the cosine component of the plasma drift velocities as measured with an ISR in the F-region. A number of subsequent studies have addressed the FAI drift–E×B correspondence assumption using ISR or satellite data as a comparison (see introduction of recent article by Bahcivan *et al.*, 2013). In several other cases, no such agreement between plasma E×B and irregularity drift velocities was obtained so that interesting questions remain about how perfect this match should be. A number of factors are invoked to explain these differences including contamination by E-region echoes (e.g.: Bahcivan *et al.*, 2013), different spatial and temporal resolutions of the instruments (Xu *et al.*, 2001) or positional uncertainties related to refraction of radar rays (e.g.: Ponomarenko *et al.*, 2009).

Besides these FAI drift–E×B discrepancy factors, linear theory predicts that non-E×B drifting F-region plasma waves or instabilities can take place near the edge of auroral arcs, where large thermal electron drifts are possible and also, near regions of ion velocity shears which can be associated with ion upflows (St-Maurice *et al.*, 2007). In those situations, it was shown that Doppler shifts of the order of the ion-acoustic speed $C_s$ could be introduced in the E×B moving frame. This topic will be further explored in the following chapters.

## 1.4.2   The spectral width

There are two main interpretations for the spectral width. The first one is related to the irregularity driving process. For example, if the process that drives decameter waves (e.g: electric field) is itself structured and turbulent, there will be a mix of spectra with various Doppler shifts. Secondly, spectra also have an inherent width associated with the lifetime of the individual structures. For short-lived structures, the spectrum is broader. In cases for which the electric field is uniform and constant with time, this feature can be observed.

Irregularities resulting from direct generation processes, or instabilities, could be differentiated as having narrower Doppler spectra, indicating that the structures are more coherent than usual. Put another way, narrow spectra might indicate that the structures are not associated with cascading or strong turbulent processes. In this case, the waves could be considered to be longer lived than usual (St-Maurice *et al.*, 2007, St-Maurice and Hamza, 2009).

This thesis is concerned with possible direct generation scenarios behind small-scale irregularities in the high-latitude F-region. A hierarchy of electrostatic instability theories that involve parallel thermal drifts, ion velocity shears or ion temperature anisotropies is presented in the following chapter.

Chapter 2

# Literature Survey

This chapter provides a synthesis of published work relevant to this thesis. In Sect. 2.1, observational results from geospace and laboratory experiments that form a motivational basis for the present study are presented. In particular, emphasis will be on observations that support the occurence of small-scale auroral structures, intense field-aligned current (FAC) densities, ion velocity shears and ion temperature anisotropies in the high-latitude F-region. Subsequently, ISR detections of naturally enhanced ion-acoustic lines (NEIAL) will be reviewed since these phenomena also constitute an important motivation for this thesis. In Sect. 2.2, selected examples of ion temperature anisotropies produced by numerical models are first discussed. Then, a summary of electrostatic plasma instability theories, triggered by FACs, shears, anisotropies or a combination thereof, which have been invoked to explain high-latitude F-region irregularities, is provided. Finally, in Sect. 2.3, the objectives of this thesis are laid out.

## 2.1 Observational Motivation

Plasma instabilities play an important role in producing small structures in the terrestrial ionosphere. In particular, current-driven electrostatic ion-acoustic (CDEIA) instabilities are known to contribute to high-latitude F-region electrodynamics. They are affected by many background parameters such as FAC densities, ion velocity shears or temperature anisotropies. In this section, we describe observations of the magnitudes of FAC density, ion velocity shear and temperature anisotropy that could be supported by the ionosphere.

### 2.1.1 Field-aligned currents

Average FAC densities in the ionosphere are generally believed to be on the order of a few $\mu A/m^2$ (for example, see Kelley, 2009, p.422). However, there are many examples of parallel current densities derived from in-situ measurements more than two orders of magnitude

larger than average values over narrow horizontal regions of several hundred meters (St-Maurice and James, 1996, Noël *et al.*, 2000, 2005, St-Maurice *et al.*, 2007, and references therein). More recent cases of spiky and intense FACs over narrow regions have been reported. For example, bursts of very intense kilometer-scale FACs were frequently observed by the Challenging Minisatellite Payload (CHAMP) when it passed through the auroral region (Rother and Lühr, 2007). In extreme cases, Rother and Lühr (2007) estimated current densities to be in excess of $3 \ mA/m^2$. Furthermore, in-situ observations from high precision magnetometers onboard the Ørsted satellites inferred small-scale FAC's several $100 \ \mu A/m^2$ in the cusp region and over spatial scales of a few hundred meters. They also reported some instances in excess of $1000 \ \mu A/m^2$ during disturbed conditions (Neubert and Christiansen, 2003). These observations suggest that very large and localized currents densities could be discharged over small spatial scales in the high-latitude ionosphere, while large-scale average current densities can be much lower. The presence of large parallel current densities associated with thermal electron drifts is the simplest mechanism to date that can explain the enhancement of either ion-acoustic shoulder in the returned power spectra that are routinely seen using incoherent scatter radars (ISR) [see Fig. 1.9].

Numerous ISR observations of NEIALs along the direction of the magnetic field (e.g.: Foster *et al.*, 1988, Collis *et al.*, 1991, Rietveld *et al.*, 1991, Sedgemore-Schulthess and St-Maurice, 2001) suggested the presence of strong and bursty field-aligned thermal relative drifts between electrons and ions, assuming that they resulted directly from a current-driven electrostatic ion-acoustic (CDEIA) instability. A more detailed discussion on NEIALs and their possible generation mechanisms will be presented in Sect. 2.2.

## 2.1.2 Small-scale auroral structures

In addition to FACs, there exist numerous examples of small auroral arcs of widths from a few metres to several decameters observed from ground-based high resolution optical cameras (e.g.: Maggs and Davis, 1968, Borovsky *et al.*, 1991, Trondsen and Cogger, 1997, 2001, Sandahl *et al.*, 2008). The existence of thin precipitation structures have also been deduced from rocket and satellite measurements (see introduction by Noël *et al.*, 2000, and

references therein). Consequently, the detection of such small-scale features suggests the presence of steep plasma density or velocity gradients associated with their boundaries. CSRs have also hinted at the possibility that perpendicular density gradients with length scales as small as 100 meters can exist in association with particle precipitation (e.g.: St-Maurice *et al.*, 1994).

### 2.1.3   Ion velocity shears

In addition to density gradients and FACs, velocity shears have been known to exist in the high-latitude ionosphere for several decades. Two types of shear have been reported. The first type consists of spatial derivatives in field-aligned (FA) ion drift velocities. In this case, the spatial derivative is perpendicular to the magnetic field. Since the magnetic field is nearly vertical at high latitudes, the gradient direction is almost horizontal. Following the same nomenclature as Koepke *et al.* (2007), we name the first type of shear "parallel" since it involves ions drifting along the magnetic field lines. This type of shear could be associated with thermal ion upflow (TIU) processes at high-latitudes. The second type of shear consists of gradients in perpendicular drift velocities. We will refer to these shears as "perpendicular". For example, at high-latitudes, shears in $\mathbf{E} \times \mathbf{B}$ ion drifts would fall into the second category.

In the following chapters, we consider only shears in parallel ion drifts velocities since we were interested to find possible linkages with ion upflows and/or NEIAL phenomena. To our knowledge, there are very few observations in the literature that consists solely of parallel shears. Nonetheless, numerous authors have reported simultaneous and co-located observations of both parallel and perpendicular shears. For example, shears in FA ion velocities were measured with a rocket near and inside an auroral arc at F-region heights and in the nighttime sector (Whalen *et al.*, 1974). During that same event, large shears in convective flow (perpendicular shears) near the poleward boundary of an intense electron precipitation region were also brought to notice. Moreover, satellite data from Dynamics Explorer 2 (DE-2) showed evidence of moderate ($\sim$1 Hz) and intense perpendicular

shears ($\sim$10 Hz), associated with electrostatic waves and observed concurrently with parallel shears (Basu *et al.*, 1988). Furthermore, horizontal gradients in parallel ion flow velocities, co-located with perpendicular shears, at high-latitudes and in the F-region, were evident in the study by Loranc *et al.* (1991), using the same satellite payload (DE-2). As indicated by Koepke *et al.* (2007), the occurence of simultaneous and co-located parallel and perpendicular shears suggests that the generation mechanisms behind one type of shear may be involved with the other one. TIUs associated with convection velocity shears were reported by Tsunoda *et al.* (1989), using the ion drift meter instrument onboard the HILAT satellite, in the dayside polar ionosphere and at 800 km of altitude. In addition to being related to velocity shears in the convection pattern, the reported TIU events were spatially coincidents with intense FACs and soft electron precipitation. Another ionospheric ion upflow study (Lu *et al.*, 1992), emerging from nearly simultaneous DE-1 and DE-2 datasets, included parallel and perpendicular shears in the ion velocities. This time, the ions outflows were observed over the nightside auroral regions. Furthermore, Kivanc and Heelis (1999) undertook a statistical study of DE-2 vertical and horizontal ion drift measurements from which both parallel and perpendicular shears were evident. The maximum shears in perpendicular drift velocities calculated over a minimum sampled scale size of 500 *m* was 1.4 Hz. The authors also suggested that some instability processes using the free energy available through sheared plasma flow configurations may have contributed to ion heating and subsequently to ion upflows.

Several perpendicular velocity shear measurements have been reported in the literature. We briefly describe some of them for completeness even though the following sections/chapters deal with perpendicular gradients in FA ion drift velocity or parallel velocity shears. For example, an intense shear in plasma convection velocities of magnitude 20 $ms^{-1}m^{-1}$(Hz) was detected by rockets at the edge of a nightside auroral arc (Kelley and Carlson, 1977), at altitudes ranging between approximately $250-550$ km, in the same region where FACs and broadband low-frequency electrostatic waves were also reported. Later, the largest perpendicular shears recorded in the literature were also uncovered from a rocket experiment (Earle *et al.*, 1989). During that rocket flight, perpendicular velocity

shears on the order of 25 Hz, in conjunction with broadband low-frequency electrostatic waves (10-1000 Hz), were reported in the auroral F-region. Coordinated observations from the Chatanika ISR and the Atmosphere Explorer C (AE-C) satellite at the poleward edge of the auroral zone, at F-region heights and in the post-midnight sector, provided evidence of ion velocity spikes, coincident with the convection reversal region (de La Beaujardiere *et al.*, 1984). The maximum velocity reached 2000 *m/s*. These observations hint at the presence of parallel electric fields occuring in regions of large shears in the convection flow.

Many authors have invoked large velocity shears in parallel ion beams detected with the Fast Auroral Snapshot Explorer (FAST) satellite in the low altitude auroral acceleration region as a motivation for studying plasma instability threshold conditions based on kinetic dispersion relations that involve Maxwellian distribution functions (e.g.: Gavrishchaka *et al.*, 1999, 2000). In one instance, Amatucci (1999) calculated parallel shears in $O^+$ drifts to be $\sim 10\Omega_i$, where $\Omega_i$ is the ion gyrofrequency. In another case, assuming a spatial dependence of the ion beam energy, Gavrishchaka *et al.* (2000) estimated that $dV_{di}/dx \approx 1.3\Omega_i$ for a $O^+$ plasma, where $V_{di}$ is the ion drift velocity. The magnitude of these shears is enormous compared to typical perpendicular shear values measured at lower altitudes with rockets. Assuming an $O^+$ gyrofrequency of approximately 200 Hz, the reported parallel shears would be in excess of 2000 Hz. In contrast with the observations that were discussed in previous paragraphs, these shears correspond to ion populations which have undergone some energization processes, bringing their energies to a few orders of magnitude above thermal levels. As a result, we chose to disregard these types of shear magnitudes in our calculations since they are representative of the thermal population. A summary of the different shears that are inferred from rocket, satellite or radar experiments is shown in Table 2.1. This table is limited to shears that have been observed in the high-latitude ionosphere.

| Rocket | Satellite | Radar | $V'_{di\perp}$ | $V'_{di\parallel}$ | Refs |
|--------|-----------|-------|---------|----------|------|
| No | Hawkeye 1 | No | Yes | No | Kintner (1976) |
| Yes | No | No | Yes | Yes | Whalen *et al.* (1974) |
| Yes | No | No | 20Hz | No | Kelley and Carlson (1977) |
| No | AE-C | Chatanika | Yes | Yes | De La Beaujardiere *et al.* (1984) |
| No | AE-D | No | Yes | No | Basu *et al.* (1984) |
| No | HILAT | EISCAT, STARE | Yes | No | Basu *et al.* (1986) |
| No | DE-2 | No | 1,10Hz | Yes | Basu *et al.* (1988) |
| No | HILAT | No | Yes | Yes | Tsunoda *et al.* (1989) |
| Yes | No | No | 25Hz | Yes | Earle *et al.* (1989) |
| No | DE-2 | No | Yes | Yes | Loranc *et al.* (1991) |
| No | DE-1,2 | No | Yes | Yes | Lu *et al.* (1992) |
| No | DE-2 | No | Yes | Yes | Kivanc and Heelis (1999) |

Table 2.1: Summary of ion velocity shears detected by rocket, satellite or radar in the high-latitude ionosphere. $V'_{di\perp}$ is the spatial derivative in perpendicular ion drift velocity, or "perpendicular" shears, and $V'_{di\parallel}$ is the spatial (perpendicular) derivative in parallel ion drift velocity, or "parallel" shears.

## 2.1.4 Ion temperature anisotropies

In addition to FACs, density gradients and velocity shears, temperature anisotropies may be encountered in space plasmas when there is a preferred direction, for instance, a strong magnetic or electric field. In the high-latitude F-region, the perpendicular ion temperature is often observed to be larger than the parallel temperature ($T_{\perp i} > T_{\parallel i}$). At low altitudes, one mechanism to heat the ions is the frictional heating of ions as they convect through the neutral gas, in presence of a DC electric field. A review of the theory relevant to ion velocity distributions in the high-latitude F-region is provided by St-Maurice and Schunk (1979). In that work, St-Maurice and Schunk (1979) found that to lowest order, the ion velocity distributions in the high-latitude ionosphere are better represented by bi-Maxwellian distributions than by one-temperature Maxwellians, with different ion temperatures parallel and perpendicular to the geomagnetic field. In particular, for the polarization and resonant charge exchange collision models, $T_{\perp i} > T_{\parallel i}$, indicating that the ion velocity distribution decreases more slowly in the perpendicular velocity plane with increasing ion velocity than in the parallel velocity plane. A point of interest is that ion

distribution functions can be seriously distorted in the presence of a strong enough perpendicular electric field. In fact, theory predicts that when the relative ion-neutral drifts exceed the neutral thermal velocity, the ion distribution function in velocity space becomes toroidal in shape (St-Maurice and Schunk, 1979). For moderate values of the relative ion-neutral drift ($V_{di/n} < 0.75\sqrt{2k_B T_n/m_n}$ where $T_n$ and $m_n$ are the neutral temperature and mass), the ion distribution is better represented by a bi-Maxwellian distribution (two temperatures) than by a Maxwellian (St-Maurice and Schunk, 1979, Raman *et al.*, 1981).

The first experimental indication of non-Maxwellian distributions in the auroral F-region was provided by St-Maurice *et al.* (1976) using a retarding potential analyser on-board the AE-C satellite. Later, anisotropic ion temperatures with $T_{\perp i}/T_{\| i} \geq 2$ were observed in the high-latitude F-region, using the tri-static European Incoherent Scatter (EIS-CAT) UHF system (e.g.: Perraut *et al.*, 1984, Løvhaug and Flå, 1986, Glatthor and Hernandez, 1990). In particular, using the EISCAT UHF system, Perraut *et al.* (1984) found that a bi-Maxwellian ion velocity distribution was present at 312 km of altitude and during strong electric field events. Also, Løvhaug and Flå (1986) found ion anisotropy ratios ($T_{\perp i}/T_{\| i}$) in the auroral F-region of 1.8 for the average situation and reaching above 2.5 in some cases. Likewise, EISCAT radar observations at a variety of aspect angles inferred ion temperature anisotropies in excess of 2 (Winser *et al.*, 1987, Lockwood and Winser, 1988).

Another proposed mechanism for perpendicular ion heating is associated with plasma waves or instabilities. For example, simultaneous European Incoherent Scatter (EISCAT) Svalbard Radar (ESR) and EISCAT VHF observations at 665 km in the dayside cusp, showed that ion upflows can be, at times, linked with significant ion temperature anisotropy (e.g.: Ogawa *et al.*, 2000). For the event considered in their paper, Ogawa *et al.* (2000) suggested that waves heated ions transversely to an anisotropy ratio of $T_{\perp i}/T_{\| i} \sim 2$ and as a result, drove F-region ion upflows. Furthermore, velocity shear-driven instabilities are a plausible mechanism for perpendicular ion heating and upflows, at least in the dayside auroral region (Tsunoda *et al.*, 1989, Liu and Lu, 2004). As indicated in St-Maurice and Hamza (2009), ion outflows appear to be, at times, located on the edges of arcs, coexist-

ing with regions of intense FAC densities, according to observations reported by Tsunoda *et al.* (1989), Wahlund *et al.* (1992a) and Kagan and St-Maurice (2005). This suggests that sheared current-driven electrostatic ion-acoustic (CDEIA) instabilities could take place near the edges of auroral structures, assuming that the current is borne by thermal particles and that the instability threshold conditions are met. Also, the existence of ion temperature anisotropies sometimes linked with ion upflow processes is an important motivation for investigating its possible contribution in enhancing sheared CDEIA waves and possibly, destabilizing the plasma.

Ion temperature anisotropies were also observed in laboratory experiments (Scime *et al.*, 2002, Spangler *et al.*, 2002, and references therein). In particular, laboratory experiments demonstrated that ion temperature anisotropy can significantly increase the growth rate of shear-driven ion-acoustic (IA) waves (Teodorescu *et al.*, 2003, Koepke *et al.*, 2003, Koepke, 2004) and modify its propagation angle. The increase in growth rate with thermal anisotropy suggests that the plasma was unstable to smaller critical drifts. Another experiment performed in the Naval Research Laboratory's Space Physics Simulation Chamber, under plasma conditions resembling those of the natural space environment, provided measurements of perpendicular ion heating by velocity-shear driven waves (Walker *et al.*, 1997). In this example, a factor of two increase in the perpendicular ion temperature was detected.

### 2.1.5  Ion upflow processes

The ionosphere represents a source population of ion outflows. A substantial body of litterature covers the subject of FA ion upflows and/or outflows. In this section, we can only touch upon a few examples of ion upflow processes that were linked to temperature anisotropies, velocity shears or a combination thereof. For a more in-depth review of the different sources of ion outflow from the high-latitude ionosphere, we refer the reader to the review by Yau and André (1997).

Several ion outflow events originate from the high-altitude F-region. Other mechanisms can operate at higher altitudes to further energize the ions into conics, beams or transversely accelerated ions (TAI) features, to name a few. As far as thermal ion upflows (TIU) are concerned, Wahlund *et al.* (1992a) divided them into two categories based on EISCAT ISR measurements in the topside auroral F-region. Type-1 TIU events (convection-driven) are associated with strong convection electric fields, elevated and anisotropic ion temperatures, hardly any auroral precipitation (low electron density) and altitudes below approximately 300 km. In this case, ion-neutral frictional heating due to perpendicular electric fields is believed to be the cause of enhanced ion temperatures, ion temperature anisotropies with $T_{\perp i} > T_{\parallel i}$, enhanced pressure gradients along the magnetic field lines and consequently, upward motions of the expanding thermal plasma (Loranc *et al.*, 1991, Wahlund *et al.*, 1992a, Loranc and St-Maurice, 1994, Kagan and St-Maurice, 2005). Furthermore, anisotropic ion temperature with $T_{\perp i} > T_{\parallel i}$ can contribute to the motion of ions along the field lines through the "magnetic mirror force" (Suvanto *et al.*, 1989, Wahlund *et al.*, 1992a). These proccesses are illustrated in Fig. 2.1

Type-2 TIU events (precipitation-driven) are associated with electron precipitation and auroral arcs, elevated electron temperature, weak convection electric fields and isotropic ion temperatures. Type-2 FA ion outflows appear to occur more frequently than type-1 events and result in larger FA ion fluxes (Wahlund *et al.*, 1992a). Although precipitation (and thermal expansion) is believed to play a role in driving the upflows, the exact generation mechanism for type-2 TIU is still a subject of debate.

In contrast with Wahlund *et al.* (1992a)'s observations, Ogawa *et al.* (2000) reported observations at 665 km in the dayside cusp, from which ion upflows were associated with significant ion temperature anisotropies, elevated and isotropic electron temperatures and soft particle precipitation. As mentionned in the previous section, the authors concluded that a wave-induced transverse heating source was driving the F-region upflows.

Other authors proposed that velocity shear-driven instabilities could heat ions at lower

altitudes and subsequently, drive ion upflows (Liu and Lu, 2004). In one particular experiment, strong ion upflows with FA velocities in excess of 1 km/s were observed by the EISCAT UHF Radar, in the dayside auroral region and at heights between 500–600 km. Indeed, the authors ruled out precipitation and Joule heating as possible direct sources for ion upflows due to low electron temperatures, low electron densities and because of the presence of small electric fields and low Joule heating rates. This proposed shear-driven source mechanism strikes one as being plausible since ion upflows associated with velocity shears had also been reported in Hilat satellite observations, in the cusp/cleft region and at 800 km altitude (Tsunoda *et al.*, 1989, Liu and Lu, 2004).

Finally, as stated by St-Maurice *et al.* (2007) and St-Maurice and Hamza (2009), ionospheric ion outflows also appear to be, at times, located on the edges of arcs, coexisting with regions of intense parallel current densities, at least based on observations reported by Tsunoda *et al.* (1989), Wahlund *et al.* (1992a) and Kagan and St-Maurice (2005). Auroral boundaries also appear to be fertile regions for the production of NEIALs. In the following section, we review relevant NEIAL observations.

## 2.1.6   Naturally enhanced ion-acoustic lines (NEIAL)

Since their discovery more than 20 years ago (Foster *et al.*, 1988, Collis *et al.*, 1991, Rietveld *et al.*, 1991), a substantial number of papers have been published on the subject of NEIALs. These anomalous ISR spectra involve short-lived enhancements of either or both IA shoulders by 1-2 orders of magnitude above thermal fluctuation levels (Sedgemore-Schulthess and St-Maurice, 2001). Examples of NEIAL observations at different altitudes obtained with EISCAT UHF radar are provided in Fig. 2.2. Since NEIAL shoulders coincide with upshifted and downshifted ion-acoustic frequencies, the scattering appears to originate from IA waves propagating away and toward the radar probing direction. NEIALs are seen to occur with timescales of less than 50 to 100 ms (Michell and Samara, 2010), at altitudes that could be as low as 140 km (Rietveld *et al.*, 1991, Sedgemore-Schulthess and St-Maurice, 2001), and as high as 1900 km (Ogawa *et al.*, 2006). Interferometric studies have shown that NEIALs were associated with extremely small horizontal spatial scales
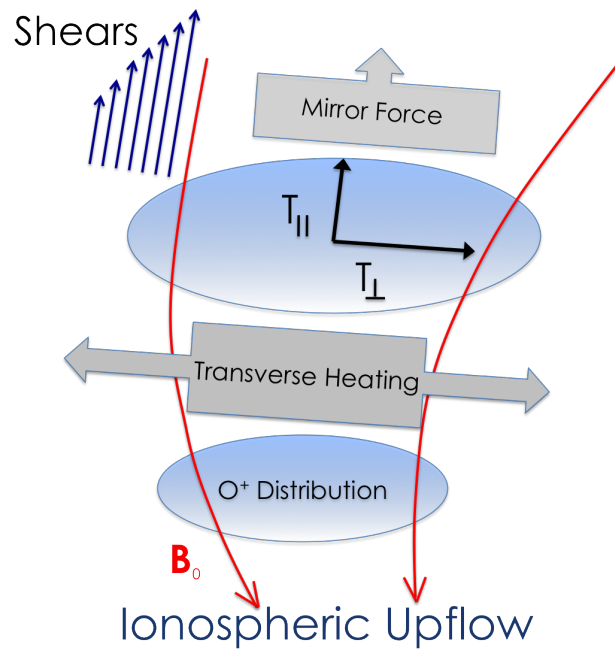
Figure 2.1: Cartoon representation of some processes associated with ion outflows. Upwelling (upflow) can first occur from ionosphere transverse heating and subsequently, the mirror force leads to motion upward and outflows. Ion velocity shears associated with ion upflows have also been observed. Adapted from a presentation by Dr.M. Zettergren during the 2013 AGU Fall Meeting.
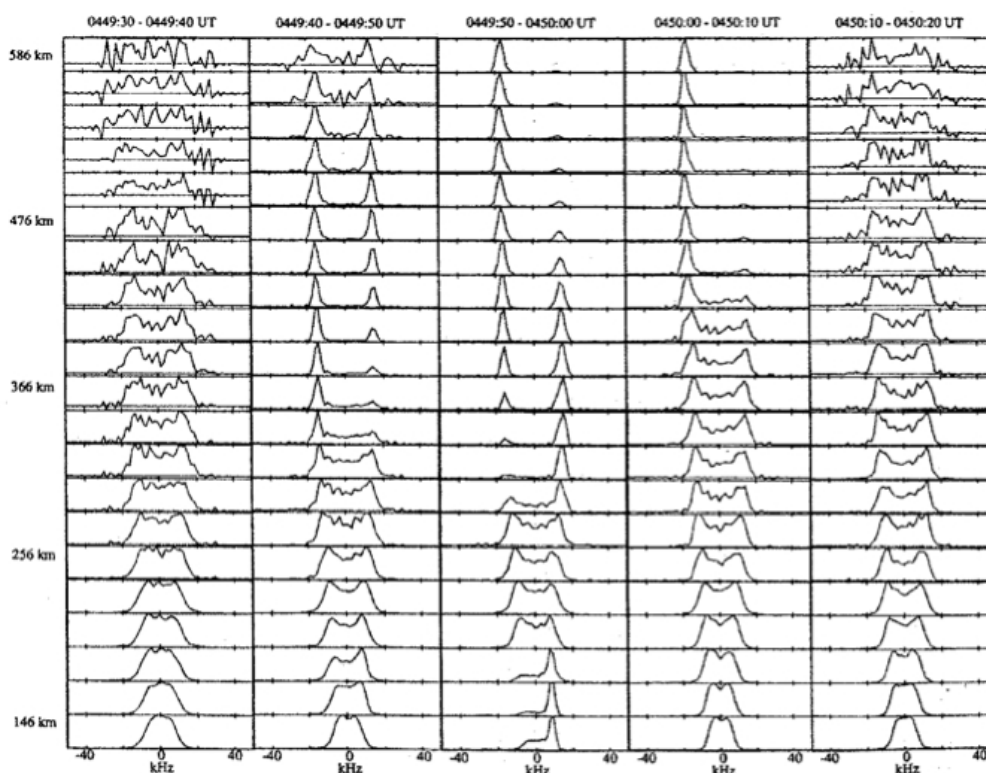
Figure 2.2: Sequence of five successive intervals of EISCAT UHF spectra showing enhanced ion-acoustic lines varying on timescales shorter than the 10 s radar integration period. Reproduced from Rietveld *et al.* (1991), Sedgemore-Schulthess and St-Maurice (2001)

of a few hundreds meters or less (Grydeland *et al.*, 2004), at an altitude of 500 km. Yet, the generation mechanism for NEIALs is still an unresolved problem and a subject of debate. Nonetheless, it appears likely that several processes play a role in the production of NEIALs, given the various ionospheric conditions, locations, altitudes and auroral morphologies under which NEIALs are detected. A thorough review of NEIALs observations made with the Millstone Hill, mainland EISCAT and EISCAT Svalbard radars (ESR) during the first decade, is presented in Sedgemore-Schulthess and St-Maurice (2001), along with a description of basic ISR theory and proposed generation mechanisms. Also, a summary of recent combined high resolution optical and radar observations with ESR and Poker Flat ISR (PFISR) is provided in the introduction of Michell and Samara (2013).

First of all, NEIALs have been observed in the nightside auroral zone, associated with

dynamic small-scale dark auroral structures (Michell *et al.*, 2008). This suggests that NEIALs may be occurring in small-scale downward current regions (DCR) associated with these dark auroral structures (Michell *et al.*, 2008). NEIALs were also detected near the edges of larger scale bright auroral structures (Collis *et al.*, 1991, Sedgemore-Schulthess and St-Maurice, 2001, Michell *et al.*, 2009, Michell and Samara, 2010) or at the polar cap-auroral oval boundary region (Michell *et al.*, 2008). Michell *et al.* (2008) also suggested a possible connection between NEIALs and broadband extremely low frequency (BBELF) wave activity, as observed in-situ by satellites and rockets at higher heights in the topside, during similar auroral morphologies and conditions. In addition, NEIAL events often coincided with elevated electron temperature and ion outflow processes (Rietveld *et al.*, 1991, Sedgemore-Schulthess and St-Maurice, 2001). In fact, intense ion outflows associated with NEIALs were reported by Rietveld *et al.* (1991), Wahlund *et al.* (1992a) and Forme *et al.* (1995). The ionospheric conditions behind the occurence of this type of NEIALs were very similar to the morphology of type-2 TIU events (Wahlund *et al.*, 1992a), as described in Sect. 2.1.5. In these cases, ISR spectra were typically asymmetric with the downshifted line preferentially enhanced (Forme *et al.*, 1995, Sedgemore-Schulthess and St-Maurice, 2001). By contrast, a second type of NEIALs, occuring at altitudes below 200 km, corresponds to slightly enhanced electron temperatures, no ion outflows and an apparent lack of precipitating particles of less than 1 keV (Forme *et al.*, 1995). In this case, both IA lines were generally seen to be enhanced.

NEIALs have also been observed in the dayside cusp with EISCAT ESR (for example, see Sedgemore-Schulthess *et al.*, 1999, Buchert *et al.*, 1999, Ogawa *et al.*, 2000, Grydeland *et al.*, 2004, Blixt *et al.*, 2005, Ogawa *et al.*, 2006, Lunde *et al.*, 2007, Sullivan *et al.*, 2008). Often in the dayside cusp, NEIALs were observed in conjunction with "flaming", dynamic and thin rayed auroral forms. Several of these identified features were directly related to the presence of low energy (10–100 eV) precipitating electrons in addition to the higher energy population producing most of auroral emissions (Blixt *et al.*, 2005). Several authors argued that low energy precipitation is essential for the formation of NEIAL's in the dayside cusp region (Blixt *et al.*, 2005, Sullivan *et al.*, 2008). In contrast with Forme

*et al.* (1995)'s study, enhancements in both IA shoulders were often observed at high altitudes above the F-region peak in the dayside cusp (Grydeland *et al.*, 2003, St-Maurice and Hamza, 2009). Interestingly, Ogawa *et al.* (2000)'s experiment demonstrated an empirical relation between ion upflows and NEIAL's however, in this case, ion temperature anisotropies were associated with the previous two phenomena.

### 2.1.7   Summary of observations

We can summarize previous observations of the high-latitude ionosphere as follows:

- Small-scale auroral structures having widths of a few metres to several decameters have been observed. NEIALs were also associated with extremely small horizontal spatial scales of a few hundreds meters or less.

- Strong and localized parallel current densities appear to exist at times despite the presence of much lower large-scale average current densities.

- Ion velocity shears also exist, often in association with low frequency waves near auroral arc edges and in presence of TIUs. Several authors proposed that velocity shear-driven instabilities could contribute in heating ions at low altitudes and produce ion upflows.

- At low altitudes where collisions with neutrals are important, ion temperature anisotropies with $T_{\perp i}/T_{\parallel i} \geq 2$ can occur due to ion-neutral frictional heating in presence of perpendicular convection electric fields. Type-1 TIU events are also associated with strong convection electric fields, elevated and anisotropic ion temperatures and low electron density.

- Ion temperature anisotropies can also be produced at higher altitudes. One proposed mechanism is perpendicular heating in presence of waves or instabilities.

- Type-2 TIU events are associated with electron precipitation and auroral arcs, elevated electron temperature, weak convection electric fields and isotropic ion temperatures. NEIAL events in the auroral zone (asymmetric with downshifted line

enhanced) often coincided with type-2 TIU conditions. Nonetheless, there are instances of ion upflows empirically linked with significant ion temperature anisotropy and NEIAL's above 600 km, at least in the dayside cusp.

- Ion upflows appear to be, at times, located near the edges of arcs, coexisting with regions of intense parallel current densities. NEIAL's were often detected near the edges of auroral structures or at the polar cap-auroral oval boundary region.

- Laboratory experiments have shown that ion temperature anisotropy can significantly increase the growth rate of shear-driven ion-acoustic (IA) waves.

In conclusion, the detection of NEIALs by ISRs near the edges of auroral structures, often linked with ion upflows and parallel current densities, suggests that shear-modified CDEIA instabilities could take place in these regions. Also, the existence of ion temperature anisotropies linked with type-1 TIUs, and sometimes with type-2 conditions, is an important motivation for investigating its possible contribution in enhancing IA waves and possibly, destabilizing the plasma.

## 2.2   Theoretical Motivation

### 2.2.1   Estimation of temperature anisotropies from theoretical considerations and numerical simulations

Numerical simulations provided evidence of ion temperature anisotropies in the auroral ionosphere. For example, Monte-Carlo studies by Winkler *et al.* (1992) created temperature anisotropies $T_{\perp i}/T_{\parallel i}$ of the order of 4/3 for $NO^+$ colliding with O. Anisotropies were more important for $O^+$ colliding with O. Indeed, for electric fields in excess of 50 $mV/m$ the resulting anisotropies $T_{\perp i}/T_{\parallel i}$ varied between 2.86 and 1.43 depending on composition (Winkler *et al.*, 1992, St-Maurice, 2003). Another Monte-Carlo simulation involving $O^+$ ions and a mixture of O and $N_2$ neutrals resulted in an anisotropy factor up to 1.5 depending on the electric field strength (Gaimard *et al.*, 1998). Furthermore, temperature anisotropies were also generated above the neutral exobase, which corresponds to the transition region

from a weakly ionized plasma (ion-neutral collisions cannot be neglected) to a fully ion-ized plasma (ion-neutral collisions can be neglected). In one particular instance, temperature anisotropies were obtained above the neutral exobase as a result of simulations from a single-component ($O^+$) time-dependent gyro-kinetic model of the high-latitude F-region response to frictional heating, between 500 km and 2500 km (Loranc and St-Maurice, 1994). This ion upflow model simulates the response of the passage of a flux tube, under various conditions, through a spatially localized heating region for which the neutral exobase is a discontinuous boundary between fully collisional and collisionless plasmas. In one particular case, an anisotropy factor of $T_{\perp i}/T_{\|i} \sim 11$ was produced after 500 $s$ and at an altitude of 1000 km. Anisotropies with parallel enhancements were also observed. For the case under consideration, the ion parallel temperature increased sharply after approximately 100 $s$ following the initial exobase heating up to transient values in excess of $2 \times 10^4$ K and then decreased abruptly at approximately 200 $s$. Nonetheless, only temperature anisotropies with $T_{\perp i} > T_{\|i}$ are studied in this thesis. Based on these numerical estimations, ion temperature anisotropies with $T_{\perp i} > T_{\|i}$ are plausible in the high latitude F-region, even at altitudes high enough that collisions with neutrals can be considered to be unimportant.

We can estimate the ion temperature anisotropy based on theoretical considerations from St-Maurice and Schunk (1977). The complete expressions for $T_{\|i}$ and $T_{\perp i}$ are respectively

$$T_{\|i} = T_n + \frac{1}{4}\left(1 + \frac{m_n}{m_i}\right)\frac{Q_{in}^{(2)}}{Q_{in}^{(1)}}\left[1 + \frac{3}{4}\frac{m_n}{m_i}\frac{Q_{in}^{(2)}}{Q_{in}^{(1)}}\right]^{-1}\frac{m_n D^2}{k_B} \tag{2.1}$$

and

$$T_{\perp i} = T_n + \frac{1}{2}\left[1 + \frac{1}{4}\left(2\frac{m_n}{m_i} - 1\right)\frac{Q_{in}^{(2)}}{Q_{in}^{(1)}}\right]\left[1 + \frac{3}{4}\frac{m_n}{m_i}\frac{Q_{in}^{(2)}}{Q_{in}^{(1)}}\right]^{-1}\frac{m_n D^2}{k_B} \tag{2.2}$$

where $Q_{in}^k$ is the generalised ion-neutral collisional cross section and where $k$ is an integer (see St-Maurice and Schunk (1979) for details), $m_i$ is the ion mass and $D$ is the magnitude of the ion $\mathbf{E} \times \mathbf{B}$ drift velocity. For $O^+$ ions colliding with their parent neutrals O (so that $m_i \approx m_n$), letting $M^2 = D^2/(2k_B T_n/m_n)$, the anisotropy ratio $T_{\perp i}/T_{\|i}$ in the limit for which

$M \gg 1$ reduces to

$$\frac{T_{\perp i}}{T_{\parallel i}} \approx \frac{1 + Q_{in}^{(2)}/4Q_{in}^{(1)}}{Q_{in}^{(2)}/Q_{in}^{(1)}} \tag{2.3}$$

We use the new set of cross sections extracted from more recent Monte Carlo results by Gaimard *et al.* (1998). These improved cross sections lead to enhanced accuracy of the analytical temperatures that are usually based on collision models that are independent of the relative energy between colliding particles (while the Monte Carlo calculations do not have this limitation). From Gaimard *et al.* (1998), $Q_{in}^{(2)}/Q_{in}^{(1)} \approx 1/5$ for $M^2 \gg 1$. As a result, Eq. (2.3) reduces to $T_{\perp i}/T_{\parallel i} \sim 5$ when the ion drifts are much larger than the neutral thermal velocity ($M^2 \gg 1$). Similarly, for a moderate value of $M^2 \simeq 2$, $Q_{in}^{(2)}/Q_{in}^{(1)} \approx 1/3$ according to Gaimard *et al.* (1998)'s results. In this case, from Eqs (2.1)-(2.2), the anisotropy is estimated to be $T_{\perp i}/T_{\parallel i} \sim 1.8$.

### 2.2.2  Electrostatic plasma instability theories

Plasma instabilities play an important role in producing small-scale irregularities in the high-latitude F-region. Several competing plasma instabilities, triggered by field-aligned drifts or horizontal shears in vertical velocity, have been invoked to explain high-latitude F-region irregularities observed by coherent or incoherent scatter radars. In this section, we present several linear instability theories that involve parallel thermal drifts, ion velocity shears under local analysis or ion temperature anisotropies and we explain how this thesis generalizes previous instability theories.

First, it is well known that a two-stream instability can arise in presence of an electron-ion relative drift across a cold unmagnetized plasma (Buneman, 1959), given that the wavelength is larger than the marginally stable Buneman wavelength $\lambda_{Bun}$ given by

$$\lambda_{Bun} = 2\pi V_{de}/\omega_{pe}[1 + (m_e/m_i)^{1/3}]^{-3/2}$$

where $V_{de}$ is the electron drift velocity with respect to the ion fluid, $\omega_{pe}$ is the electron plasma frequency and $m_{e,i}$ is the electron/ion mass. CDEIA waves can also be excited

when electrons having a finite temperature are drifting with respect to the ions (Fried and Gould, 1961). The CDEIA instability as it applies to the topside ionosphere was further investigated by Kindel and Kennel (1971). If FACs are sufficiently strong, we could expect IA waves propagating along the direction parallel to the geomagnetic field ($\mathbf{B}_0$) and current, which could translate into field-perpendicular density irregularities. As pointed out by Kindel and Kennel (1971), ion-cyclotron (IC) waves could become unstable at a lower relative drift threshold values, especially when $T_e \sim T_i$. These IC waves would propagate in a nearly perpendicular direction with respect to $\mathbf{B}_0$.

The role of parallel ion velocity shears in the excitation of plasma instabilities using a fluid theory was first investigated by D'Angelo (1965). The D'Angelo's zero frequency purely growing mode was recently extended to small wavelengths by Chibisov *et al.* (2011), using a kinetic formalism, into the so called "Ion-kinetic D'Angelo" mode. Also, Basu and Coppi (1988, 1989) developed a fluid theory of collisional electrostatic modes destabilized by sheared field-aligned ion velocity. The kind of waves that were destabilized are also near zero frequency, in the $\mathbf{E} \times \mathbf{B}$ frame of reference, and propagating perpendicularly to $\mathbf{B}_0$. This mode is referred to as "small frequency ion shear driven instability."

The role of parallel ion velocity shears on electrostatic IA instability eigenmodes and threshold conditions required for the onset of instability were studied by Gavrishchaka *et al.* (1998, 1999), using a kinetic theory that was developed by Ganguli *et al.* (1988) in the local approximation. In particular, they suggested that infinitesimally weak velocity shears could significantly lower the threshold current of the CDEIA instability even when $T_i \sim T_e$. St-Maurice *et al.* (2007) generalized Gavrishchaka *et al.* (1998)'s results by adding collisional terms and finite Larmor radius (FLR) corrections to the isotropic kinetic dispersion relation, which were ignored by previous authors. In St-Maurice *et al.* (2007) they developed a generalized kinetic-based framework using a local expansion of a drifting Maxwellian about a particular position in space, a procedure that differs from Gavrishchaka *et al.* (1998)'s approach. By taking the fluid, weakly collisional and shear-free CDEIA limit of St-Maurice *et al.* (2007)'s dispersion relation, an expression for the eigenfrequency that

is equivalent to Ossakow and Chaturvedi (1979)'s mode when ion inertia is inserted into the current-convective fluid derivation was obtained. The eigenfrequency of this inertial mode free of shear in the absolute frame of reference $\omega_R^A$ is given by (St-Maurice *et al.*, 2007)

$$\omega_R^A = \mathbf{k}_\perp \cdot \mathbf{V}_{\perp 0} + k_\parallel V_{di} \pm \frac{k_\parallel C_s}{\sqrt{k_\perp^2 C_s^2 / \Omega_i^2}} \qquad (2.4)$$

where $k_\perp$ and $k_\parallel$ are the perpendicular and parallel components of the wave number respectively, $\mathbf{V}_{\perp 0}$ is the plasma E×B drift and $C_s$ is the ion-acoustic speed. This frequency mode contains a mixture of parallel IA and IC modes, which could be detected with Super-DARN radar geometries more easily than pure cyclotron modes (wavevector nearly exactly perpendicular to the magnetic field) or pure IA modes (wavevector along $\mathbf{B}_0$). The significance of this result is that it is not aspect sensitive. As long as the parallel electron drifts are large enough, radars could observe an instability for a large range of possible directions. Consequently, the presence of such non-E×B F-region plasma waves could provide an explanation for Doppler discrepancies between FAI and E×B velocities (see Sect.1.4.1) by contributing an additional Doppler shift in the E×B moving frame [second term of Eq. (2.4)].

Perron *et al.* (2009) systematically studied the instability threshold requirements from St-Maurice *et al.* (2007)'s kinetic dispersion relation for different ion to electron temperature ratios. The picture that emerged from St-Maurice *et al.* (2007) and Perron *et al.* (2009)'s results is more complicated than what was predicted by Gavrishchaka *et al.* (1999). In some cases, realistic values of ion velocity shears contribute to reduce the instability threshold relative drift, but for very specific wave vector directions that are near perpendicular to $\mathbf{B}_0$.

More recently, Mikhailenko *et al.* (2006, 2012) presented a kinetic dispersion relation equivalent to Gavrishchaka *et al.* (1998, 1999) and studied the ion-cyclotron branch analytically. Mikhailenko *et al.* (2008) added the effects of collisions to Mikhailenko *et al.* (2006)'s work, but their published kinetic dispersion relation does not include the FLR ef-

fects uncovered by St-Maurice *et al.* (2007).

Gavrishchaka *et al.* (1998, 1999)'s work was extended by Spangler *et al.* (2002), who derived a dispersion relationship for a Maxwellian plasma that included temperature anisotropy and shears. They showed that an ion temperature anisotropy alters the frequency modes of the sheared CDEIA instability by solving the dispersion equation numerically. They also demonstrated that ion thermal anisotropy increases the maximum growth rate. This result was consistent with the laboratory results of Teodorescu *et al.* (2003). Spangler *et al.* (2002)'s findings involved numerical solutions of the dispersion relationship in terms of real frequency and growth rate, but they did not consider threshold conditions. Perron *et al.* (2013) studied the instability threshold conditions with anisotropies, for the limiting case in which collisions are neglected and FLR corrections are small. They showed that ion temperature anisotropy may significantly lower the drift threshold required for instability, for a large range of aspect angles and under small and realistic shears.

In order to better picture the physics involved with each kind of instability discussed thus far, a summary of linear electrostatic plasma instability theories that could be relevant to high-latitude F-region irregularities is displayed in Fig. 2.3. The instabilities are organized along the following categories: kinetic or fluid, presence of parallel currents densities carried by thermal populations, ion velocity shears, ion temperature anisotropies, collisions and FLR corrections. In this figure, the instabilities grouped under "fluid" also belong to the "kinetic" category since fluid-like modes can be obtained as a limiting case of the kinetic treatment (see App.A for more information). Although some of these instability theories were put together from fluid equations, a kinetic-based framework must be used if one wishes to study instability threshold conditions in situations for which Landau damping effects are taken into account. Hence, the kinetic formulation presented in Chap.3 regroups all the instability theories discussed previously into one single generalized kinetic framework, which includes the possibility of temperature anisotropies and the FLR effects brought forward by St-Maurice *et al.* (2007). Furthermore, this thesis expands the analysis of Spangler *et al.* (2002) and Perron *et al.* (2013) by adding collisional and FLR effects to
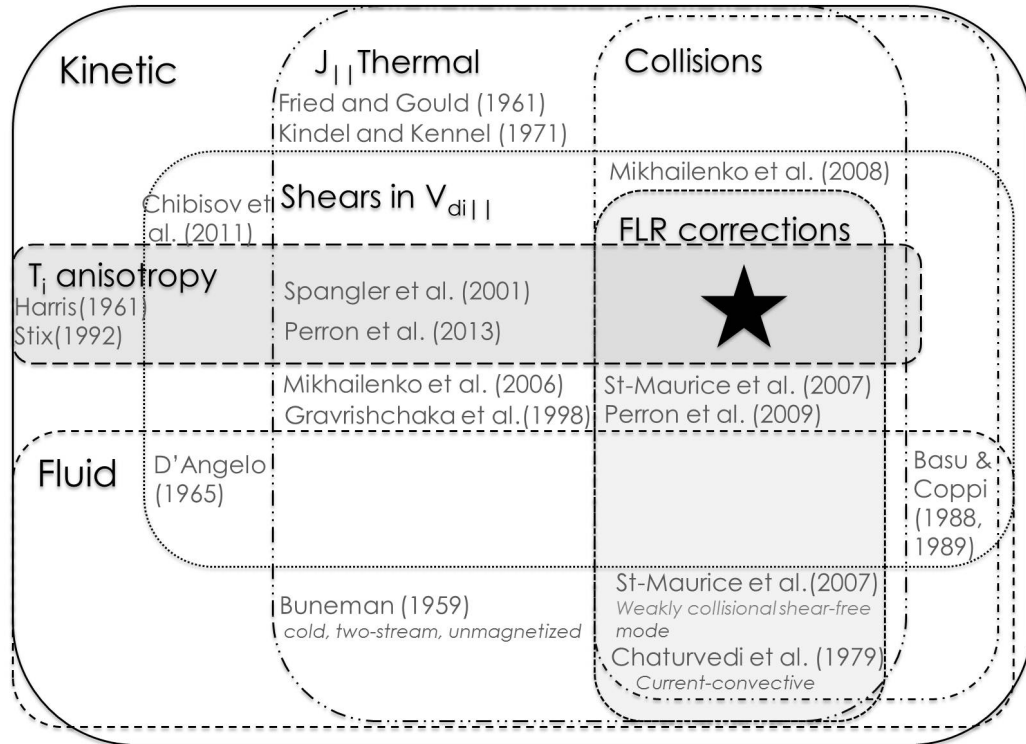
Figure 2.3: Summary of linear electrostatic plasma instability kinetic (solid line) and fluid (dashed line) theories, in presence of parallel current densities ($J_\parallel$) borne by thermals (dash-double-dot line), shears in parallel ion velocity ($V_{di\parallel}$) under local analysis (dot-line), ion temperature ($T_i$) anisotropies (long-dash line, dark grey area), collisions (dash-dotted line) or FLR corrections (short-dash line, light grey area), relevant to high-latitude F-region irregularities. The sub-region marked with a star, which corresponds to Chap.3 of the present work, generalizes all other theories.

the anisotropic dispersion relations.

### 2.2.3  Theories for NEIAL's

Several generation mechanisms have been proposed to explain NEIALs. The simplest theory is the standard CDEIA (or two-stream) instability (Kindel and Kennel, 1971), which can be triggered when a thermal electron population is streaming at a high enough velocity with respect to the ion frame (Collis *et al.*, 1991, Rietveld *et al.*, 1991, Sedgemore-Schulthess and St-Maurice, 2001). The simplest source of streaming arises from parallel electric fields that exist in auroral precipitation regions (Sedgemore-Schulthess and St-

Maurice, 2001). One possible way to produce the required parallel electric field is the presence of a sharp cut-off in auroral precipitation (100-200 m horizontal scale), resulting in a correspondingly large conductivity gradient (St-Maurice and James, 1996, Noël *et al.*, 2000, 2005). Electron-ion relative thermal drifts can also be produced from FA ion upflow motions set up by perpendicular electric fields, gradients in electron temperature or shears in the $\mathbf{E} \times \mathbf{B}$ drifts (Sedgemore-Schulthess and St-Maurice, 2001). This direct excitation mechanism agrees with the numerous observations of NEIALs near the edges of auroral arcs rather than in the middle of the arcs. The seemingly higher NEIAL's occurence rates at elevated electron temperatures and for smaller ISR operating frequencies (or longer wavelengths) is consistent with the notion that CDEIA instabilities are more easily triggered when $T_e/T_i$ is large and at longer wavelengths (Buneman, 1959, Kindel and Kennel, 1971, Sedgemore-Schulthess and St-Maurice, 2001). Lastly, the frequent detections of NEIALs at high altitudes, in conjunction with higher downshifted enhancement occurences (for example, see Fig. 10 of Grydeland *et al.*, 2004), agrees well with the scenario in which thermal electrons escape near the altitude where precipitating electrons are stopped.

The main criticism for CDEIA is the fact that the threshold current densities have to be several hundred $\mu A/m^2$, hence 2 orders of magnitude greater than the average larger-scale currents that have been measured by space-borne instruments. Nonetheless, such large FA currents appear to exist at times, at least locally, as mentioned in Sect. 2.1.1. Furthermore, although this mechanism can explain the enhancement of one IA shoulder, it fails to amplify both peaks in close proximity in space and time. Finally, another proposed mechanism based on streaming instabilities relies on relative drift between two ion thermal populations (ion-ion two stream) (Wahlund *et al.*, 1992b).

In contrast with streaming instabilities, a third theory is based on the parametric decay of Langmuir waves into ion-acoustic waves through the "bump-on-tail" instability (Forme, 1993, Forme *et al.*, 1995, Forme, 1999, Guio and Forme, 2006). In this case, beams of soft non-thermal electron precipitation of the order of a few tens of eV appear to be sufficient

to excite the required Langmuir turbulence (Sedgemore-Schulthess and St-Maurice, 2001). An important advantage of this theory is the capacity to enhance both IA shoulders simultaneously. However, it is not clear how this mode-coupling mechanism could destabilize both upshifted and downshifted IA waves (double IA excitation) from precipitation, at least at lower altitudes, since soft electrons should be stopped by the atmosphere at approximately 250 km (St-Maurice and Hamza, 2009). A likely scenario suggested by St-Maurice and Hamza (2009) is that CDEIA could operate at lower altitudes while higher up, runaway electrons could take over the currents, producing Langmuir turbulence and therefore, enhance both peaks. However, as described previously, NEIALs with double IA excitation were also observed at altitudes below 200 km in the nightside auroral zone (Forme *et al.*, 1995). Furthermore, more complex nonlinear models on the theme of cascading from enhanced Langmuir waves were proposed by Kontar and Pécseli (2005) and Daldorff *et al.* (2007). Diaz *et al.* (2010, 2011) studied beam plasma instability effects on ISR spectra and suggested that Langmuir harmonics could be detected by a properly configured ISR.

Based on numerical simulations, Bahcivan and Cosgrove (2008) suggested that enhanced IA waves could be being driven by electrostatic IC waves through a two-step mechanism. In their paper, they also considered the effect of transverse velocity shears on the IA instability on ISR spectra from the generalized dispersion relation developed by Ganguli *et al.* (1988). However, according to their simulation results the transient gradient in the relative magnetic field aligned drift as driven by the electrostatic IC wave had a negligible effect on the amplitude of IA oscillations. Additionally, they considered the role of ion temperature anisotropy in the growth of shear-modified IA waves based on the work of Spangler *et al.* (2002) and Teodorescu *et al.* (2003). Since the shear effect as part of electrostatic IC wave oscillations was not significant for a large range of angles, they concluded that ion temperature anisotropy needs to be addressed independently from the shear effect using an advanced higher-dimensional numerical simulation code.

## 2.3 Objectives and Outline

### 2.3.1 Objectives

The observations and theoretical considerations described in this chapter support the notion that intense and localized FACs that could be in excess of 1000 $\mu A/m^2$, ion velocity shears on the order of 1-20 m s$^{-1}$ m$^{-1}$(Hz) and ion temperature anisotropies $T_{\perp i}/T_{\parallel i}$ on the order of 2-5 can be sustained in the high-latitude F-region. In addition to these observations, the generation of NEIALs is still an unresolved research topic. The clear detection from VHF and UHF radars of coherent echoes when the wavevector is not perpendicular to the magnetic field (not field-aligned) suggests that unexpectedly large FACs or shears are present at times. Therefore, it appears relevant to include additional physics by exploring the possible contribution of temperature anisotropies in lowering the threshold requirements for sheared CDEIA instabilities in the high-latitude F-region where collisions exist at lower altitudes. We chose to analyze marginally stable conditions because plasma destabilisation is already a challenging task by itself. Moreover, as far as E-region radar observations are concerned, there is a tendency for the phase speed of the largest amplitude irregularities to saturate at the drift threshold, at least for structures less than 10 m in size (St-Maurice and Hamza, 2009).

In terms of plasma instabilities, there is a requirement to generalize previous electrostatic theories, as shown in Fig. 2.3, into a single kinetic-based dispersion relation that includes the possibility of temperature anisotropies and the FLR effects brought forward by St-Maurice *et al.* (2007). We restricted the scope of this thesis to FA current densities borne by thermal particles before considering more complex situations involving nonthermal populations.

The first important objective of this thesis was to investigate whether ion temperature anisotropy could lower the threshold conditions of ion shear CDEIA instabilities in both a collisionless and collisional F-region. To this end, we generalized the electrostatic kinetic dispersion relationship presented by St-Maurice *et al.* (2007) to a bi-Maxwellian plasma

and we derived analytical expressions for the threshold relative drift and ion velocity shears in the fluid limit. Moreover, we explored kinetic threshold solutions at a higher ion to electron temperature ratio, which could better represent F-region plasmas, by numerically solving the new kinetic dispersion relation that includes the ion temperature anisotropy.

Another objective was to study the effects of both ion velocity shears and temperature anisotropies on the ISR spectrum density function to determine whether this additional physics could enhance the IA spectrum. To accomplish this, we derived the ISR spectral density function for stable, magnetized and collisionless plasmas, using a bi-Maxwellian distribution function and following the kinetic approach presented in Froula *et al.* (2010). We computed ISR spectra under various ion temperature anisotropies and velocity shears.

### 2.3.2 Outline of the remainder of this thesis

- **Chapter 3:** In this chapter, we first generalize the electrostatic kinetic dispersion relationship of St-Maurice *et al.* (2007) to a bi-Maxwellian plasma and we derive analytical expressions for the threshold relative drift and ion velocity shears in the fluid limit. We then assess how CDEIA threshold conditions in the long wavelength limit are affected by the inclusion of ion velocity shears and ion temperature anisotropies. Finally, we discuss some implications in terms of the production of plasma irregularities in the F-region and their possible observation with coherent scatter radars. The content of this chapter has led to the following articles:

  - P.J.G. Perron, J.-M. Noël, J.-P. St-Maurice and K. Kabin, Ion temperature anisotropy effects on the dispersion relation and threshold conditions of a sheared current-driven electrostatic ion-acoustic instability with applications to the collisional high-latitude F-region, *J. Plasma Phys.*, submitted 9 January 2014.

  - P.J.G. Perron, J.-M. Noël, K. Kabin and J.-P. St-Maurice, Ion temperature anisotropy effects on threshold conditions of a shear-modified current driven electrostatic ion-acoustic instability in the topside auroral ionosphere, *Ann. Geophys.* **31**

(3), 451-457, 2013, doi:10.5194/angeo-31-451-2013.

- **Chapter 4:** In this chapter, we explore the possible contribution of additional physics (ion velocity shears and temperature anisotropy) in modifying the incoherent scatter spectral density function. First, we study the effects of ion temperature anisotropy on the shear-free spectrum when ion gyroresonances are taken into account. Then, we investigate possible spectral modifications due to the presence of ion velocity shears. We discuss the conditions under which these calculations are valid and we explain the implications of these results in terms of enhanced IA spectra that could be observed with ISRs. This chapter corresponds to the following manuscript in preparation:

  - P.J.G. Perron, J.-M. Noël, J.-P. St-Maurice and K. Kabin, An assessment of how incoherent scatter radar spectra can be enhanced by small shears associated with large drift velocity gradient scale lengths, Manuscript in prep. for *J. Geophys. Res.* or *Ann. Geophys.*

- **Chapter 5:** This chapter summarizes the main results and proposes a plan for additional research to undertake.

As a final note, although the following paper is not related to the content of this thesis, the research and writing was completed during the PhD sponsorship period:

- P.J.G. Perron, On the requirement of space weather situational awareness to achieve effects in a joint, interagency, domestic and arctic environment, *Canadian Military Journal*, submitted 14 August 2013 (Expected to be published in Fall 2014).

Chapter 3

# Ion Temperature Anisotropy Effects on the Dispersion Relation and Threshold Conditions of sheared CDEIA Instabilities in the High-Latitude F-Region

In this chapter, we generalize the electrostatic kinetic dispersion relation presented by St-Maurice *et al.* (2007) to a bi-Maxwellian plasma and we investigate how CDEIA marginal stability conditions (zero growth rate) in the long wavelength limit are affected by ion velocity shears and temperature anisotropies. In Sect. 3.1, we present the main derivation features leading to the final kinetic dispersion relation that includes ion temperature anisotropy, FLR corrections and collisions, following the same procedure as set out in St-Maurice *et al.* (2007). In Sect. 3.2, we study the fluid limit and we compare the results with previous theories. In Sect. 3.3, instability threshold conditions that we obtained from the generalized kinetic dispersion relation at higher perpendicular ion to electron temperature ratios are described. Finally, in Sect. 3.4, we summarize the main results and discuss some implications in terms of F-region irregularity observations of coherent echoes by ionospheric radars.

## 3.1 The Generalized Kinetic Derivation with Ion Temperature Anisotropy

In this section, we introduce the derivation leading to the anisotropic kinetic dispersion relation. We follow the same procedure that was laid out in St-Maurice *et al.* (2007). In other words, we perform a spatial expansion of a drifting bi-Maxwellian distribution in the weak shear limit and we use the local approximation ($k_x = 0$). In this model, the drift velocity is aligned with the geomagnetic field $\mathbf{B}_0$ and the gradient in the drift velocity (i.e. the shear) is perpendicular to $\mathbf{B}_0$, in the $x$-direction. The wave vector $\mathbf{k}$ lies in the $y - z$ plane at an angle $\theta$ with respect to the direction perpendicular to $\mathbf{B}_0$. The geometry of this model is shown in Fig. 3.1. We have also restricted the study to shears in ion drift velocity ($V'_{di}$) in order to relate to actual ionospheric observations associated with ion upflows processes.
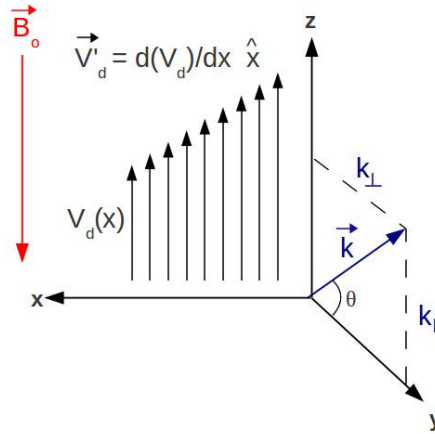
Figure 3.1: Geometry of the model. The drift velocity is aligned with the geomagnetic field $\mathbf{B}_0$ and the gradient in the drift velocity is perpendicular to $\mathbf{B}_0$, in the $x$ direction. The wave vector $\mathbf{k}$ lies in the $y-z$ plane at an angle $\theta$ with respect to the direction perpendicular to $\mathbf{B}_0$. The perpendicular and parallel components of $\mathbf{k}$ are $k_\perp$ and $k_\parallel$.

Moreover, realistic electron velocity shears appear to have a negligible effect on the shear-free solutions (Perron *et al.*, 2013, and references therein). Furthermore, we assume that the electron temperature is isotropic and that the modes are electrostatic. Similarly to St-Maurice *et al.* (2007)'s approach, collisional effects are described with a Bhatnagar-Gross-Krook (BGK) particle conserving collision model (Bhatnagar *et al.*, 1954, Froula *et al.*, 2010). The simple BGK collision operator is primarily used to represent electron-neutral or ion-neutral collisional effects and, in some cases, electron–ion collisions (Froula *et al.*, 2010, page 59). As a result, the RHS of Boltzmann equation (1.3) takes the form

$$\left(\frac{\delta f_j}{\delta t}\right)_c = -\nu_j \left[f_{1j} - \frac{n_{1j}}{n_j} f_{0j}(\mathbf{v})\right] \tag{3.1}$$

where $f_j$ is the average distribution function of species $j$, $\nu_j$ is the collision frequency of species $j$ and $n_j$ is the number density of species $j$.

### 3.1.1 Derivation of the kinetic dispersion relation

We follow the same steps as St-Maurice *et al.* (2007), emphasising the new contributions that originates from the use of an anisotropic bi-Maxwellian distribution function. Starting from the linearized Boltzmann-Poisson system of equations in Fourier-Laplace space, the

dispersion relation for electrostatic modes in a magnetized and collisional plasma is given by

$$\frac{H_i(k,\omega)}{1+U_i(k,\omega)} + \frac{H_e(k,\omega)}{1+U_e(k,\omega)} + 1 = 0. \tag{3.2}$$

The $j^{th}$ component susceptibility is

$$H_j(\mathbf{k},\omega) = \frac{\omega_{pj}^2}{k^2} \int_{-\infty}^{+\infty} d\mathbf{v} \int_0^{+\infty} i\mathbf{k} \cdot \frac{\partial f_{0j}'}{\partial \mathbf{v}} e^{ib_j(\xi)} d\xi \tag{3.3}$$

where $b_j(\xi) = -\mathbf{k} \cdot (\mathbf{r} - \mathbf{r}') + \xi(\omega + i\nu_j)$ and $\xi = t - t'$. In the previous equations, $k = (k_\perp^2 + k_\parallel^2)^{1/2}$ is the wave number, $\omega_{pj}$ is the $j^{th}$ species plasma frequency and $\omega$ is the wave frequency. The function $U_j$, which arises from the inclusion of the BGK collision model (Eq. 3.1) in Boltzmann equation, is given by

$$U_j(\mathbf{k},\omega) = -\frac{\nu_j}{n_j} \int_{-\infty}^{+\infty} d\mathbf{v} \int_0^{+\infty} f_{0j}' e^{ib_j(\xi)} d\xi. \tag{3.4}$$

For the remainder of this section, we drop the subscript $j$ to simplify the equations. In order to account for possible differences between thermal velocities in the directions parallel and perpendicular to the magnetic field, we select a bi-Maxwellian distribution drifting along $z$ for $f_{0j}$. As mentionned previously, we use the local approximation with a plane wave ansatz in the $y - z$ plane and we expand the drifting bi-Maxwellian around a particular position in space to first order in $x$ and in the weak shear limit. In this case, the vertical drift is a function of the horizontal position $x$ and we write

$$f \approx f_{0bm}(x) + \Delta x \frac{\partial f_{0bm}}{\partial x} \approx f_{0bm} + f_{0bm}\Delta x V_d' \left(\frac{m}{k_B T_\parallel}(v_\parallel - V_d)\right) \tag{3.5}$$

where $f_{0bm}$ denotes a bi-Maxwellian distribution function, $V_d' = \partial V_d/\partial x$ is the shear in the vertical drift velocity ($V_d$), $T_\parallel$ is the temperature in the direction parallel to $z$ and $k_B$ is the Boltzmann constant. In the calculation of the $H_j$ functions, we evaluate $\mathbf{k} \cdot \partial f_{0j}'/\partial \mathbf{v}$ using the method of integration over unperturbed trajectory and the characteristics of the motion. Keeping only the linear (average) contribution we get

$$k_y \frac{\partial f}{\partial v_y} = \left[ -\frac{m}{k_B T_\perp} k_y v_\perp \sin(\Omega\xi + \phi) - \left(\frac{m}{k_B}\right)^2 \frac{1}{T_\parallel T_\perp} V_d'(v_z - V_d) \frac{k_y v_\perp^2}{2\Omega} \right] f_{0bm} \tag{3.6}$$

where $\phi$ is the velocity initial angle in the $x - y$ plane and $\Omega = qB/m$ is the gyrofrequency. After having performed the Bessel decomposition in the exponential of the phase term and

the angular and time ($\xi$) integrations, Eq. (3.3) can now be expressed as

$$H = \frac{\omega_p^2}{k^2} 2\pi \int_{-\infty}^{+\infty} dv_\parallel \int_0^\infty v_\perp \, dv_\perp \sum_n \frac{m/k_B T_\parallel \left(A + \frac{T_\parallel}{T_\perp} n\Omega\right) J_n^2 \left(k_\perp v_\perp / \Omega\right) f_{0bm}}{\omega - |k_\parallel| v_\parallel - n\Omega + i\nu} \qquad (3.7)$$

where $A = |k_\parallel|(v_\parallel - V_d)\left(1 - \frac{1}{2}\frac{k_\perp}{|k_\parallel|}\frac{mv_\perp^2 V_d'}{k_B T_\perp \Omega}\right)$. The $v_\perp$ integration gives

$$H = \frac{\omega_p^2}{k^2}\left(\frac{m}{2\pi k_B T_\parallel}\right)^{3/2} \times \qquad (3.8)$$

$$\sum_n \int_{-\infty}^{+\infty} dv_\parallel \frac{|k_\parallel|(v_\parallel - V_d)\left[\Gamma_n(b) - \frac{k_\perp}{|k_\parallel|}\frac{V_d'}{\Omega}\Gamma_n^*(b)\right] + \frac{T_\parallel}{T_\perp}n\Omega\Gamma_n(b)}{\omega - |k_\parallel| v_\parallel - n\Omega + i\nu} \times$$

$$\exp\left(-\frac{m}{2k_B T_\parallel}(v_\parallel - V_d)^2\right)$$

where $b = k_\perp^2 v_{\perp t}^2 / \Omega^2 = k_\perp^2 \rho_L^2$ is the argument of the exponentially scaled modified Bessel function of the first kind $\left[\Gamma_n(b) = I_n(b)e^{-b}\right]$, $\rho_L = \sqrt{\frac{k_B T_\perp}{m\Omega^2}}$ is the Larmor radius and $v_{\perp t}^2 = k_B T_\perp / m$ is the perpendicular thermal velocity. Note that $b$ is different than the variable $b_j$ used in Eqs. (3.3)–(3.4). The expression $\Gamma_n^*$, which results from the integration of the second term in Eq. (3.7) and accounts for additional FLR contributions (St-Maurice *et al.*, 2007), is given by

$$\Gamma_n^*(b) = \left[(1-b)I_n(b) + bI_n'(b)\right]e^{-b}. \qquad (3.9)$$

For small Larmor radius corrections, or $b = k_\perp^2 \rho_L^2 \ll 1$, $\Gamma_n^*$ becomes $\approx \Gamma_n$. The anisotropy effects appear in Eq. (3.8) through the additional ratio $T_\parallel/T_\perp$ that multiplies the third term of the integrand. Furthermore, we note that the relevant temperature in the denominator of the $H$ function is the parallel one ($T_\parallel$).

### 3.1.2 The final kinetic dispersion relation

Integrating in $v_\parallel$ along the Landau contour, we can express the susceptibility for the ions ($H_i$) in terms of the plasma dispersion function Z, which gives

$$H_i = \frac{1}{k^2\lambda_{Di\perp}^2}\left[\frac{T_{\perp i}}{T_{\parallel i}} + \sum_n \Gamma_n(b_i)\left(\frac{1}{\sqrt{2}|k_\parallel|v_{\parallel ti}}\right) \times \right.$$

$$\left[n\Omega_i\left(1 - \frac{T_{\perp i}}{T_{\parallel i}}\right) + \omega\frac{T_{\perp i}}{T_{\parallel i}}\right]Z\left(\frac{\omega + i\nu_i - n\Omega_i}{\sqrt{2}|k_\parallel|v_{\parallel ti}}\right) -$$

$$\left.\sum_n \Gamma_n^*(b_i)\frac{T_{\perp i}}{T_{\parallel i}}\frac{k_\perp V_{di}'}{|k_\parallel|\Omega_i}\left[1 + \frac{\omega + i\nu_i - n\Omega_i}{\sqrt{2}|k_\parallel|v_{\parallel ti}}Z\left(\frac{\omega + i\nu_i - n\Omega_i}{\sqrt{2}|k_\parallel|v_{\parallel ti}}\right)\right]\right]. \tag{3.10}$$

where $\lambda_{Di\perp}$ is the ion perpendicular Debye length, $\Omega_i = q_i B/m_i$ is the ion gyrofrequency and $b_i = k_\perp^2 v_{\perp ti}^2/\Omega_i^2 = k_\perp^2 \rho_{Li}^2$. Also, in this expression, the charge for ions is assumed to be equal to 1 since we have ionospheric applications in mind with $O^+$ as being the major constituent. For the electron susceptibility, since we are considering low-frequency waves ($\omega \ll \Omega_e$), or equivalently $\rho_{Le} = \sqrt{v_{te}/\Omega_e} \to 0$, we get

$$H_e = \frac{1}{k^2\lambda_{Di\perp}^2}\frac{T_{\perp i}}{T_e}\left[1 + \left(\frac{\omega - k_\parallel V_{de} + i\nu_e}{\sqrt{2}|k_\parallel|v_{te}}\right)Z\left(\frac{\omega - k_\parallel V_{de} + i\nu_e}{\sqrt{2}|k_\parallel|v_{te}}\right)\right]. \tag{3.11}$$

The expressions for $U_i$ and $U_e$ are respectively

$$U_i = \frac{i\nu_i}{\sqrt{2}|k_\parallel|v_{\parallel ti}}\left[\sum_n \Gamma_n(b_i)Z\left(\frac{\omega + i\nu_i - n\Omega_i}{\sqrt{2}|k_\parallel|v_{\parallel ti}}\right)\right] \tag{3.12}$$

and

$$U_e = \frac{i\nu_e}{\sqrt{2}|k_\parallel|v_{te}}Z\left(\frac{\omega - k_\parallel V_{de} + i\nu_e}{\sqrt{2}|k_\parallel|v_{te}}\right). \tag{3.13}$$

In Eqs. (3.10)–(3.13), the parallel and perpendicular thermal velocities for ions (electrons) are respectively $v_{\parallel ti,e} = \sqrt{k_B T_{\parallel i,e}/m_{i,e}}$ and $v_{\perp ti,e} = \sqrt{k_B T_{\perp i,e}/m_{i,e}}$, $V_{de}$ is the electron parallel drift velocity with respect to the ion frame of reference (or electron-ion relative drift) and finally, $\nu_{i,e}$ is the ions (electrons) collision frequency with the neutrals. Indeed, the ion temperature anisotropy modifies the ion susceptibility ($H_i$) expression through the correction term $n\Omega_i(1 - T_{\perp i}/T_{\parallel i})$. Moreover, anisotropy acts to enhance $H_i$ since each term is multiplied by $T_{\perp i}/T_{\parallel i}$. By contrast, the electron susceptibility ($H_e$) does not depend on ion anisotropy. For shear-free situations ($V_{di}' \to 0$) and small Larmor radius corrections such

that $k_\perp \rho_{Li} \ll 1$, the linear dispersion relation for electrostatic waves in anisotropic magnetised hot plasmas is recovered (e.g. Stix, 1992, chap. 11).

## 3.2  The Fluid-Like Limit

### 3.2.1  Fluid-like dispersion relation

In this section, we begin by studying the fluid-like limit of the $k_y = 0$ finite-Larmor-radius kinetic and anisotropic electrostatic dispersion relation. Following standard procedures, we apply the small electron and large ion argument polynomial expansion to the plasma dispersion functions Z and we use the small Debye-length approximation ($k\lambda_{Di\perp} \to 0$). Consequently, for the $n = 0$ mode, $T_{\parallel i}/T_e \ll 1$ and to leading order in $b_i$, Eq. (3.2), along with Eqs. (3.10)–(3.13), reduces to

$$\omega\left(\omega + i\nu_i\right) - k_\parallel^2 C_s^2 + A_i b_s \left(\omega + i\nu_i\right)^2 + \frac{k_\perp |k_\parallel| C_s^2}{\Omega_i} V'_{di}\left(1 - 2b_i - 2A_i b_s \frac{(\omega + i\nu_i)^2}{k_\parallel^2 C_s^2}\right) \quad (3.14)$$

$$+ i\sqrt{\pi}\left(\frac{\omega + i\nu_e - |k_\parallel| V_{de}}{\sqrt{2}|k_\parallel| v_{te}}\right)\left(\omega + i\nu_i\right)\left(\omega + i\nu_i b_i\right) = 0.$$

where $A_i = T_{\perp i}/T_{\parallel i}$, $b_s = k_\perp^2 C_s^2/\Omega_i^2 = b_i/\tau$ and where $\tau = T_{\perp i}/T_e$ (in the fluid-like limit $C_s^2 \approx k_B T_e/m_i$.) Details on the procedure to derive the fluid-like dispersion are provided in Appendix A. The resulting collisional fluid dispersion equation (3.14) can be compared to its isotropic version (see Eq. (3.18) of St-Maurice *et al.*, 2007).

Equation (3.14) generalizes several cases, which were considered in previous publications. Firstly, when FLR corrections are small ($k_\perp \rho_{Li} \ll 1$) and collisions are neglected, we recover the fluid dispersion studied by Perron *et al.* (2013). If we drop the influence of temperature anisotropy ($A_i \to 1$), and collisional and FLR effects, the fluid-like results of Gavrishchaka *et al.* (1998) are retrieved. For shear-free and isotropic situations ($V'_{di} = 0$ and $A_i \to 1$), $V_{de} \sim C_s$ is required to destabilize the plasma, a threshold condition in agreement with the CDEIA instability (Kindel and Kennel, 1971). Finally, for sheared, collisional and isotropic conditions, if we approach the zero frequency limit and for propagation angles almost perpendicular to the magnetic field, Eq. (3.14) reduces to Basu and Coppi (1988,

1989)'s minimum shear condition for the onset of the ion shear-driven instability, which they derived directly a using fluid treatment.

## 3.2.2 Threshold conditions for a collisional, sheared and anisotropic plasma

In this section, we derive expressions for the threshold drift ($V_{de}/C_s$) and ion shear ($S_i = V'_{di}/\Omega_i$) associated with the fluid-limit of the generalized kinetic expression for zero growth rate conditions. For simplicity, we further define a new shear parameter as $\zeta_i = k_\perp S_i/|k_\parallel| = S_i/\tan\theta$ where $\tan\theta = |k_\parallel|/k_\perp$. Taking the real part of Eq. (3.14) yields the following expression for the ion shears at threshold

$$\zeta_i = \frac{1 - (\omega_R/k_\parallel C_s)^2(1 + A_i b_s) + A_i b_s (v_i/k_\parallel C_s)^2 + \varepsilon_t}{1 - 2b_i - 2A_i b_s(\omega_R/k_\parallel C_s)^2 + 2A_i b_s(v_i/k_\parallel C_s)^2} \tag{3.15}$$

where

$$\varepsilon_t = \varepsilon \frac{\omega_R v_i}{(k_\parallel C_s)^2}(1 + b_i)\left(\frac{\omega_R}{k_\parallel C_s} - \frac{V_{de}}{C_s}\right) + v_{et} \tag{3.16}$$

and

$$v_{et} = \varepsilon \frac{v_e}{k_\parallel C_s}\left[(\omega_R/k_\parallel C_s)^2 - \tau b_s(v_i/k_\parallel C_s)^2\right] \tag{3.17}$$

and

$$\varepsilon = \sqrt{\frac{\pi m_e}{2m_i}} \ll 1. \tag{3.18}$$

Similarly, taking the imaginary part gives the following expression for the threshold drift

$$\frac{V_{de}}{C_s} = \frac{\omega_R}{|k_\parallel|C_s} + \frac{\omega_R v_i/(kC_s)^2}{\varepsilon}\frac{2A_i b_s(1 - 2\zeta_i) + 1}{(\omega_R/kC_s)^2 - b_i(v_i/kC_s)^2} - v_{er} \tag{3.19}$$

where

$$v_{er} = \frac{v_e}{v_i}\frac{v_i}{kC_s}\frac{\omega_R}{|k_\parallel|C_s}\frac{b_i + 1}{(\omega_R/k_\parallel C_s)^2 - b_i(v_i/k_\parallel C_s)^2}. \tag{3.20}$$

Note that the previous equations for the ion shears and threshold drift are coupled through the term $\varepsilon_t$ (see Eq. 3.16). Equations (3.15)–(3.20) are generalizations of the equations published by St-Maurice *et al.* (2007). As stated by these authors, unless shear contributions are large and positive, adding collisions to the fluid sheared CDEIA modes tends to put a larger requirement on the threshold conditions in terms of the relative drift. This result is expected since collisions generally produce a dampening effect on waves. There is

a significant difference between the collisionless and collisional cases because of the amplification produced by the $1/\varepsilon$ factor in Eq. (3.19). In the present study, the anisotropy factor multiplies four terms in the ion shear threshold expression (3.15), in addition to the $1/\varepsilon$ term (second) in the critical relative drift equation (3.19).

We further examine the effects of ion temperature anisotropy on the fluid-like threshold conditions by plotting them for different values of the wave vector angle $\theta$ and for $A_i = T_{\perp i}/T_{\|i} = 1, 2, 5$ and 10. For all calculations, we used $O^+$ as the major ion constituent with $m_i/m_e = 29166$. In Perron *et al.* (2009), they presented a detailed analysis of instability threshold conditions corresponding to the isotropic case ($T_{\perp i}/T_{\|i} = 1$), in the kinetic and collisional regime. In this thesis, since we are primarily interested in comparing threshold conditions in the presence of temperature anisotropy with the isotropic case, we chose to present curves of threshold velocity shears as a function of relative drifts for different anisotropy ratios ($A_i = 1, 2, 5$ and 10). For a more comprehensive analysis of the instability threshold conditions as a function of the wave vector angle, for $A_i$=1 and under various ion to electron temperature ratios, we refer the reader to the publication by Perron *et al.* (2009).

In Fig. 3.2, we present the threshold conditions for the fluid sheared CDEIA instability in a collisional plasma for different values of anisotropies. Similarly to previous work, rather than solving for the frequency as a function of shears and drift parameters, the wave frequency and the gyrofrequency were fixed to $\omega_R/kC_s = 0.5$ and $\Omega_i/kC_s = 2$ respectively, and the associated threshold shears and drifts were calculated for different values of $\theta$, using Eqs. (3.15)–(3.20). These input parameters were chosen in order to compare with previous results of St-Maurice *et al.* (2007) and Perron *et al.* (2009, 2013). Also, setting $\Omega_i/kC_s = 2$ ensures that $b_s$ remains smaller than 1, for consistency with the $n = 0$ ion-acoustic mode and with the FLR correction (St-Maurice *et al.*, 2007). In Fig. 3.2, the *y*-axis shows how the threshold conditions change with ion shear, while the *x*-axis represents the corresponding threshold values of $V_{de}/C_s$. Each curve is traced by sweeping over the aspect angle $\theta$ from 90° to 0°. The angle $\theta$ is equal to 90° when the wavevector is parallel to $\mathbf{B}_0$ and 0° when perpendicular to it. It should be mentioned that there is a specific angle that

| Frequency | ion to electron mass ratio | Ion Gyrofrequency |
|---|---|---|
| $\omega/kC_s = 0.5$ | $m_i/m_e = 29166$ | $\Omega_i/kC_s = 2$ |
| Ion collision frequency | Electron to ion collision frequency ratio | Angles |
| $\nu_i/\Omega_i = 0.01$ | $\nu_e/\nu_i = 10$ | $0° < \theta = \text{atan}(|k_\parallel|/k_\perp) < 90°$ |

Table 3.1: Summary of parameters that have been kept constant for the calculation of instability threshold conditions for Fig. 3.2.

does not yield a solution because of the presence of a singularity. This singularity, which will be shown graphically hereafter, was discussed extensively in St-Maurice *et al.* (2007).

The selected collision frequencies for the case under study, which are representative of F-region situations below approximately 400 km, are also identical to those of previous work by Perron *et al.* (2009). The parameters that were fixed for this study are summarized in Table 3.1.

Note that we neglected the small $-V_{de}/C_s$ term in Eq. (3.16) when computing the threshold conditions in the fluid-like limit. This contribution turned out to be non-negligeable only for small frequencies, when $\omega/kC_s \lesssim 0.1$ (St-Maurice *et al.*, 2007, Perron *et al.*, 2009). In the same fashion as the collisionless case, the validity of Eqs. (3.15)–(3.20) was confirmed by solving the kinetic dispersion relation (3.2), along with Eqs. (3.10)–(3.13), at low temperature ratios ($\tau$) and within $|S_i| \lesssim 1$. The exact numerical solutions were in excellent agreement with the analytical solutions for $A_i = 1, 2, 5$ and 10, in the limit $\tau \lesssim 0.01$. For consistency with the numerical solutions of the kinetic dispersion relation (see Sect. 3.3), we traced those threshold curves that correspond to intermediate and large angles $\theta$ in red.

The red traces of Fig. 3.2 clearly show that anisotropies push the threshold loci up to higher drift requirements for intermediate and large angles, as expected from Eq. (3.19)

(except for the $A_i = 10$ curve that behaves differently). However, as the aspect angle approaches $0°$ (direction perpendicular to $\mathbf{B}_0$), past the singularity, threshold drifts and shears become small in spite of collisions. In fact, the small angle portion (black traces) of Fig. 3.2 exhibits solutions restricted to very narrow angular intervals (fractions of a degree) that deviates from perpendicularity by less than $10°$. It was suggested by St-Maurice *et al.* (2007) that these solutions were equivalent to the small frequency ion shear driven instability (Basu and Coppi, 1988, 1989). Interestingly, in the collisional regime, increasing the anisotropy lowers the narrow angles minima to smaller shear requirements. For instance, an anisotropy of $A_i = 2$ acts to reduce the shear threshold from $S_i \approx 0.22$ to $0.15$. To better present how the threshold conditions vary with the wave vector angle, we have plotted the threshold shear and drift separately in the upper and lower panel of Fig. 3.3, respectively, as a function of angle $\theta$. The minima in threshold drift at $\theta \sim 5°$ are clearly visible in the lower panel. The corresponding threshold shears in the upper panel are associated with $S_i \lesssim 0.22$. Based on this case, we are led to conclude that ion temperature anisotropies reduce the threshold drift minima of the small frequency ion shear driven modes to smaller shear requirements.

### 3.2.3 The weakly collisional shear-free and anisotropic limit

In their paper, St-Maurice *et al.* (2007) explored the regime $\zeta_i \to 0$, $\omega_R > v_i$ and for which the wave vector direction is sufficiently far from perpendicularity ($k_\perp/k_\parallel \ll 1$). They obtained an eigenfrequency expression equivalent to Ossakow and Chaturvedi (1979)'s mode when ion inertia is inserted into their fluid equations. From Eq. (3.15), we consider the same limiting case for which $\zeta_i \to 0$, $\omega_R > v_{in}$ and $k_\perp/k_\parallel \ll 1$. The resulting frequency mode that allows ion temperature anisotropy in the frame of reference moving with the ions is given by

$$\omega_R = \frac{|k_\parallel| C_s}{\sqrt{1 + (T_{\perp i}/T_{\parallel i}) k_\perp^2 C_s^2/\Omega_i^2}}. \tag{3.21}$$

Assuming that $C_s = 1500 \ ms^{-1}$ in the F-region, the second term in the denominator of Eq. (3.21) is large compared to 1 (for waves with $\lambda \sim 10 \ m$), so that Eq. (3.21) can be
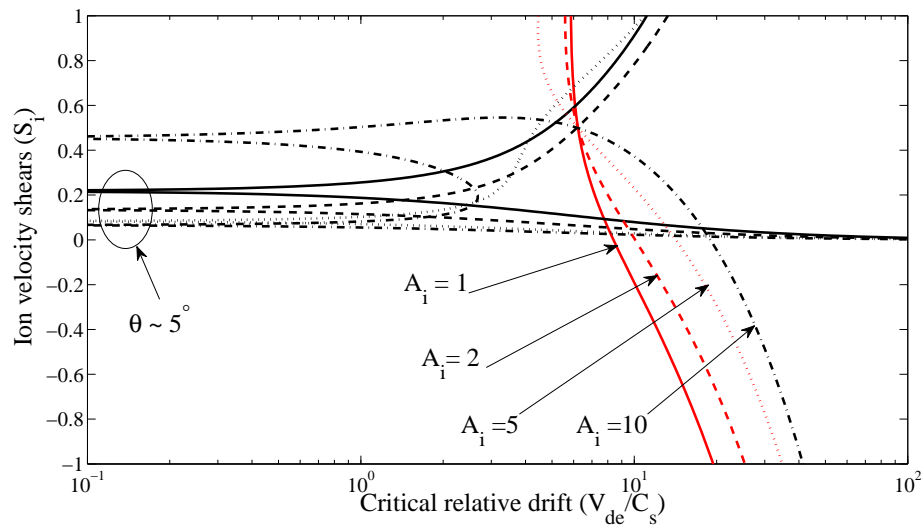
Figure 3.2: Threshold conditions for the fluid sheared CDEIA instability in an anisotropic, collisional $O^+$ plasma using Eqs. (3.15)–(3.20). Threshold values of $S_i$ as a function of $V_{de}/C_s$ are traced for $A_i = T_{\perp i}/T_{\parallel i}$ from 1 (solid), 2 (dashed), 5 (dotted) and 10 (dashed-dotted). The near vertical threshold curves in red correspond to oblique waves with $30° \lesssim \theta \lesssim 60°$, $\theta$ decreasing from top to bottom. The threshold curves in black are associated with small angles ($\theta \lesssim 30°$). Parameters that were fixed for this study are summarized in Table 3.1.
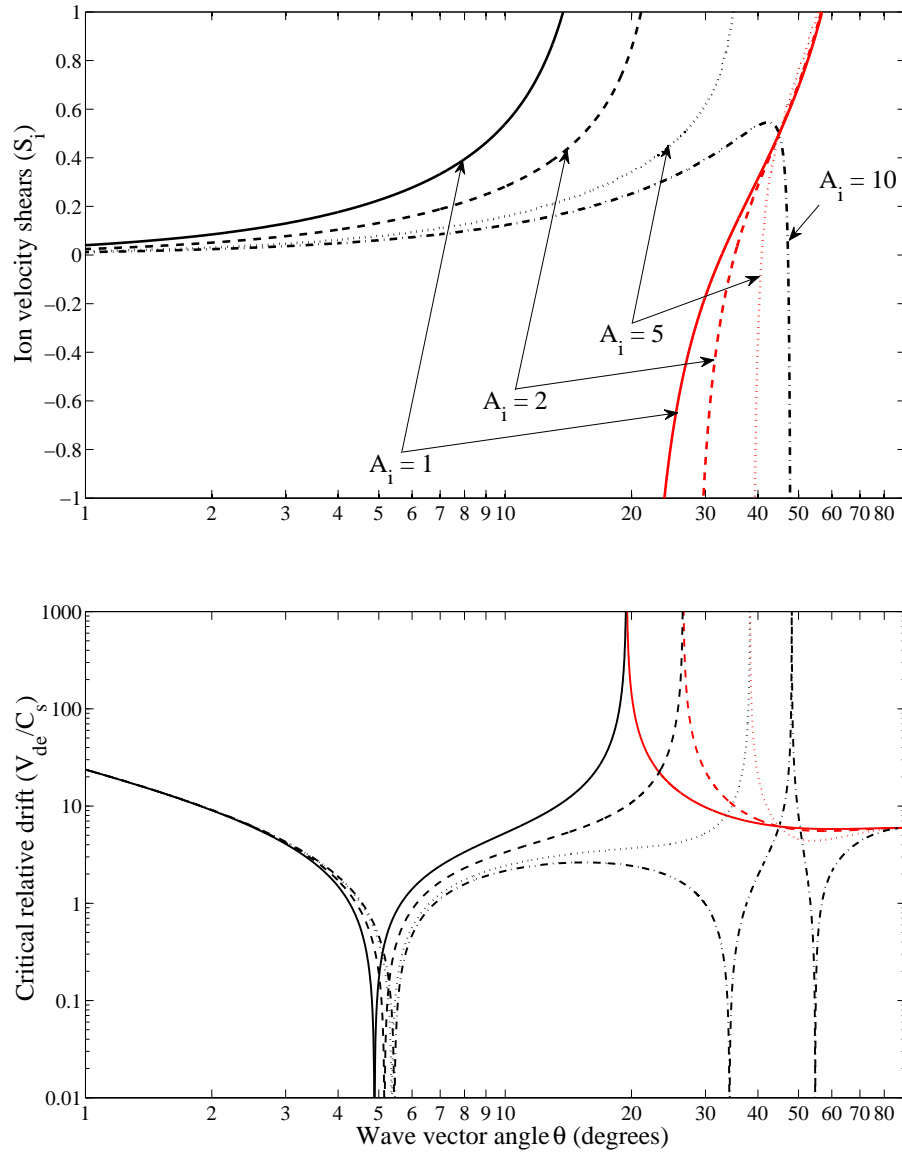
Figure 3.3: Variation of the threshold shear $S_i$ (upper panel) and drift $V_{de}/C_s$ (lower panel) with the wave vector angle for the fluid sheared CDEIA instability in an anisotropic, collisional $O^+$ plasma using Eqs. (3.15)–(3.20). Threshold conditions are traced for $A_i = T_{\perp i}/T_{\parallel i}$ from 1 (solid), 2 (dashed), 5 (dotted) and 10 (dashed-dotted). The threshold curves in black are associated to small angles (except for $A_i = 10$ that behaves differently). Parameters that were fixed for this study are summarized in Table 3.1.

simplified to

$$\omega_R \approx \frac{|k_\parallel|}{k_\perp} \frac{T_{\parallel i}}{T_{\perp i}} \Omega_i. \tag{3.22}$$

This result suggests that under shearless and weakly collisional conditions, ion temperature anisotropy plays a role in setting the Doppler frequency shift that could be detected with SuperDARN HF radars. Equation (3.22) predicts a lowering of frequency shift for larger anisotropies.

From Eq. (3.19), the electron drift requirement (with respect to the ion frame) under the same conditions becomes

$$\frac{V_{de}}{C_s} = \frac{\omega_R}{|k_\parallel|C_s} + \frac{v_i}{\omega_R} \frac{1 + 2A_i b_s}{\varepsilon} \tag{3.23}$$

where, as in previous sections, $A_i = T_{\perp i}/T_{\parallel i}$. From Eq. (3.23) we conclude that ion temperature anisotropy can play an important role in determining the threshold conditions of the weakly collisional shear-free CDEIA mechanism since $\varepsilon$ is a small quantity.

## 3.2.4 The small frequency anisotropic ion shear-driven instability

We now consider the zero-frequency ion-shear driven instability that was studied by Basu and Coppi (1989), allowing for the possibility of ion temperature anisotropy with $T_{\perp i} \neq T_{\parallel i}$. From Eq. (3.15), in the limit where $v_i \gg \omega_R$ or $\omega_R \to 0$, we obtain the following expression for the shear required to destabilize the plasma

$$\frac{V'_{di}}{\Omega_i} = \frac{|k_\parallel|}{k_\perp} \frac{1 + A_i(v_i/\Omega_i)^2(k_\perp/|k_\parallel|)^2}{1 + 2A_i(v_i/\Omega_i)^2(k_\perp/|k_\parallel|)^2}. \tag{3.24}$$

From Eq. (3.24), $A_i$ lowers the shear threshold requirement by a small amount. However, for small angles such that $|k_\parallel| \ll k_\perp$, temperature anisotropy has no effect on the shear threshold values since in this case, $V'_{di}/\Omega_i \approx |k_\parallel|/2k_\perp$. While the threshold shears might be small near zero frequency for $|k_\parallel| \ll k_\perp$, the relative drift requirements might be large, given that some of the denominators in Eq. (3.19) are close to zero. As indicated by St-Maurice *et al.* (2007), the small frequency regime must be explored more carefully in the limit of small aspect angles $|k_\parallel| \ll k_\perp$ before drawing definitive conclusions.

From Eq. (3.24), if we assume that the second term in the denominator is much larger than unity $\left[2A_i(v_i/\Omega_i)^2(k_\perp/|k_\parallel|)^2 \gg 1\right]$, we obtain the following expression for the threshold shear

$$\frac{V_{di}'}{\Omega_i} = \frac{|k_\parallel|}{k_\perp} + \frac{T_{\perp i}}{T_{\parallel i}}\left(\frac{v_i}{\Omega_i}\right)^2 \frac{k_\perp}{|k_\parallel|}. \tag{3.25}$$

This assumption might not prove to be consistent since $v_i/\Omega_i$ can be very small for F-region conditions. As a curiosity and for comparison purposes with the work of Basu and Coppi (1989), the minimum shear condition can be obtained by differentiating Eq. (3.25) with respect to $|k_\parallel|/k_\perp$ and setting the resulting expression equal to zero, which gives

$$\tan\theta = \frac{|k_\parallel|}{k_\perp} = \frac{v_i}{\Omega_i}\sqrt{\frac{T_{\perp i}}{T_{\parallel i}}} \tag{3.26}$$

As a result, the minimum shear threshold condition of Basu and Coppi (1989), allowing for the presence of ion temperature anisotropy, is recovered

$$\left(\frac{V_{di}'}{\Omega_i}\right)_{min} = 2\frac{v_i}{\Omega_i}\sqrt{\frac{T_{\perp i}}{T_{\parallel i}}}. \tag{3.27}$$

### 3.2.5 The collisionless sheared and anisotropic limit

#### 3.2.5.1 Fluid-like threshold conditions without neglecting FLR corrections

Starting from Eq. (3.15), the collisionless limit ($v \to 0$) yields the following eigenfrequency

$$\omega_R = |k_\parallel|C_s\sqrt{\frac{1-\zeta_i}{1+A_ib_s(1-2\zeta_i)}}. \tag{3.28}$$

Similarly, Eq. (3.19) reduces to

$$\frac{V_{de}}{C_s} = \frac{\omega_R}{|k_\parallel|C_s} \tag{3.29}$$

allowing us to express the critical drift required for instability as a function of ion shears and anisotropy

$$\frac{V_{de}}{C_s} = \sqrt{\frac{1-\zeta_i}{1+A_ib_s(1-2\zeta_i)}}. \tag{3.30}$$

Expressions (3.28)–(3.30) generalize the results of Spangler *et al.* (2002) and Perron *et al.* (2013) through the inclusion of FLR corrections. The contribution due to FLR effects is the

factor $(1-2\zeta_i)$ that multiplies $A_i b_s$ in the denominator of Eq. (3.28) and (3.30). This correction, which arises only in presence of shears, matters mostly for near-perpendicular modes. Depending on the sign of the ion shears ($\zeta_i$) and the angle of propagation ($\tan\theta = |k_\parallel|/k_\perp$), the threshold drift required for the onset of instability may be elevated or reduced. Similarly to the collisional case, there will be a specific angle that will not yield a solution because of the presence of a singularity. The new contribution due to anisotropy comes from the product of $(1-2\zeta_i)$ with $A_i b_s$. In addition to shifting the singularity at a slightly different angle, the anisotropy factor is capable of lowering the threshold drift under small shear values.

In Fig. 3.4, we present the threshold conditions for the sheared CDEIA instability in a collisionless plasma for the same values of anisotropies as before ($A_i = 1, 2, 5$ and 10). On the left hand side of Fig. 3.4, the threshold loci below $V_{de}/C_s = 1$ correspond to oblique waves with aspect angles in the approximate range $30° \lesssim \theta \lesssim 50°$, $\theta$ decreasing from top to bottom. The new contribution due to FLR corrections [factor $(1-2\zeta_i)$ in Eq. (3.30)] corresponds to the threshold loci on the right hand side, which display aspect angles in the range $\theta \lesssim 10°$, decreasing from top to bottom. These "small angles" curves are traced in black in Fig. 3.4. The range of $S_i$ was reduced to $\lesssim 0.1$ in order to better display the threshold variations with $A_i$. The validity of Eqs. (3.28)–(3.29) was confirmed by solving the kinetic dispersion equation (3.2), along with Eqs. (3.10)–(3.11), at low temperature ratios $\tau$ and within $|S_i| \lesssim 1$. The exact numerical solutions were in excellent agreement with the analytical solutions for $A_i = 1, 2, 5$ and 10, in the limit $\tau \lesssim 0.01$, as expected.

Inspecting the vertical loci (red curves) on the left hand side of Fig. 3.4, there is a small decrease of critical drift as the anisotropy factor is increased from 1 to 10, similarly to previous results with no FLR effects (Perron *et al.*, 2013). For intermediate angles and for the parameters considered herein, this anisotropy effect is not significantly sensitive to shears since the threshold curves remain almost parallel to each other. Although FLR corrections bring the threshold drift requirements up to higher values for small angles (close to perpendicularity), temperature anisotropy, combined with positive shears, act to reduce the

Figure 3.4: Threshold conditions for the fluid sheared CDEIA instability in an anisotropic, collisionless ($v_i = v_e = 0$) $O^+$ plasma using Eqs. (3.28)–(3.29). Other parameters that were fixed for this calculation are presented in Table 3.1. The line scheme is the same as in Fig. 3.2. The near vertical threshold curves on the left hand side (red) correspond to oblique waves with $30° \lesssim \theta \lesssim 50°$, $\theta$ decreasing from top to bottom. The threshold curves on the right hand side (black) correspond to small angles $\theta \lesssim 10°$ decreasing from top to bottom.

small angle threshold loci (black curves) by a significant amount. For example, a shear of $S_i \approx 0.1$ is capable of lowering $V_{de}$ by a factor of almost 2, assuming that $C_s$ remains constant. Nevertheless, in this case, the threshold drift requirement is still high ($V_{de}/C_s \approx 7.5$) and it is more likely that waves propagating at intermediate angles would become unstable before waves propagating almost perpendicularly to the magnetic field.

To better see the variation of threshold drift with ion temperature anisotropy, we consider two examples where we fix the propagation angle. Equation (3.30) is plotted in the upper panel of Fig. 3.5 for $\theta = 47°$ and in the lower panel for $\theta = 1°$. The normalized critical drift $V_{de}/C_s$ is traced as a function of $A_i$ for negative ($S_i = -0.05$), zero ($S_i = 0$) and positive ($S_i = 0.05$) shears. The upper panel curve exhibits a lowering of critical drift requirement as a function of $A_i$ in presence of negative shear. This reduction in threshold drift is expected by inspection of Eq. (3.30). For comparison purposes, the zero-shear curve, which is identical to the one presented in Perron *et al.* (2013), is also traced in the upper panel. While still considering the intermediate angle ($\theta = 47°$) case, we see that a combination of anisotropies and positive shears are capable of lowering the threshold drift when $A_i \lesssim 5$. For example, an anisotropy ratio of $\sim 2$ reduces the critical relative drift in the presence of a small positive or negative shear. When considering wave propagation very close to perpendicularity (lower panel), in this case $\theta = 1°$, both positive and negative shears enhance the decrease in the critical relative drift, especially when $A_i$ is larger than approximately 1.5. This decrease is shown to be more significant for positive shears. In fact, in this particular case, $V_{de}/C_s$ is decreased from approximately 3.2 to 0.6 as $A_i$ is doubled from 1 to 2. As a result, we are led to conclude that despite the fact that FLR corrections increase the threshold drift requirements for wave propagation near perpendicularity to $\mathbf{B}_0$, ion temperature anisotropy is capable, at least in some cases, of reducing the critical drift $V_{de}$ below the classical CDEIA threshold condition which is the ion-acoustic speed of the medium $C_s$ (Kindel and Kennel, 1971).
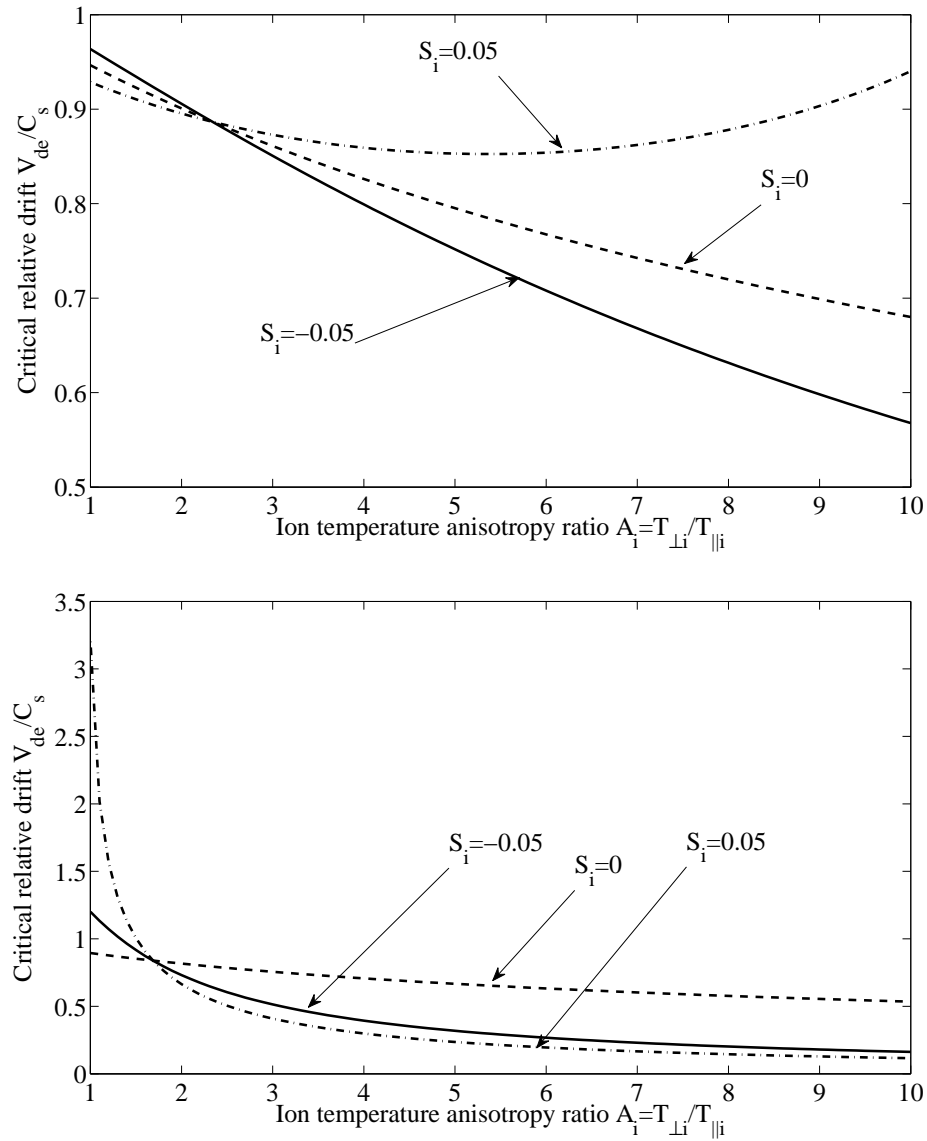
Figure 3.5: Variation of critical relative drift as a function of ion temperature anisotropy for the fluid sheared CDEIA instability in collisionless $O^+$ plasma with $\Omega_i/kC_s = 2$. Equation (3.30) is plotted in the upper panel for $\theta = 47°$ and in the lower panel for $\theta = 1°$. $V_{de}/C_s$ as a function of $A_i = T_{\perp i}/T_{\| i}$ is traced for $S_i$ from -0.05 (solid), 0 (dashed) and 0.05 (dashed-dotted).

### 3.2.5.2 Fluid-like threshold conditions when neglecting FLR effects

This section corresponds to a study published by Perron *et al.* (2013). We only summarize the main findings here. In that paper, we studied instability threshold conditions for the limiting case in which collisions are neglected ($v_{i,e} \to 0$, or equivalently $U_{i,e} \to 0$), and finite Larmor radius corrections are small ($k_\perp \rho_{Li} = k_\perp v_{\perp ti}^2 / \Omega_i^2 \ll 1$), so that $\Gamma_n^* \approx \Gamma_n$. These conditions could resemble topside F-regions, at high enough altitudes where collisions could be neglected, but below approximately 1000 km. In this limit, the kinetic dispersion presented by Spangler *et al.* (2002) is recovered. In their paper, Spangler *et al.* (2002), who added thermal anisotropy effects to Gavrishchaka *et al.* (1998) dispersion relation, derived a fluid-like mode after having performed the large ion and small electron argument expansions. They concluded that the fluid-like dispersion relation for ion-acoustic waves in an anisotropic plasma does not depend explicitly on ion temperature anisotropy. They essentially obtained an expression equivalent to the isotropic case except that the relevant electron temperature was the parallel electron temperature. However, in Perron *et al.* (2013), it was shown that a new fluid-like expression that depends explicitly on ion temperature anisotropy can be derived by keeping higher order terms in the expansion. The aforementioned paper also showed that anisotropy factors lower the critical drift requirement for instability in the quasi-fluid limit. It can be shown that in the fluid limit, the critical relative drift becomes

$$\frac{V_{de}}{C_s} = \frac{\sqrt{1 - \zeta_i}}{\sqrt{1 + b_s A_i}}. \tag{3.31}$$

Indeed, the inclusion of ion anisotropy lowers the critical drift by a relatively small correction ($\sqrt{1 + b_s A_i}$) in the denominator. The term $b_s A_i$ can be re-written as $(T_{\perp i}/T_{\parallel i}) k_\perp^2 T_e / \Omega_i^2$. Clearly, the anisotropy ratio ($T_{\perp i}/T_{\parallel i}$) contributes to lower the instability critical drift, although this effect will be more important when the wave vector is closer to the perpendicular direction than parallel (so that $k_\perp$ is not small). Since the balance of imaginary terms leads to $V_{de}/C_s = \omega_R/|k_\parallel|C_s$ (see Eq. 3.29), the fluid-like dispersion in this limit can be expressed as

$$\frac{\omega_R}{|k_\parallel|C_s} = \frac{\sqrt{1 - \zeta_i}}{\sqrt{1 + b_s A_i}}. \tag{3.32}$$

By neglecting the new contribution ($\sqrt{1 + b_s A_i}$), we recover an expression similar to the one published in Spangler *et al.* (2002), namely

$$\frac{\omega_R}{|k_\parallel|} = \sqrt{\frac{k_B T_e}{m_i}}(1 - \zeta_i).$$

(3.33)

Since Spangler *et al.* (2002) also considered electron temperature anisotropy, the relevant electron temperature in their expression is the parallel electron temperature.

## 3.3  Instability Threshold Conditions from the Kinetic Dispersion Relation

In this section, we investigate how the ion temperature anisotropy ratio $A_i = T_{\perp i}/T_{\parallel i}$ influences the kinetic threshold curves for an ion to electron temperature ratio that is more representative of F-region conditions than the fluid-like limit considered hereinbefore by numerically solving the kinetic dispersion relation (3.2), along with Eqs. (3.10)–(3.13). Similarly to the fluid study, we consider the long wavelength limit for which $k\lambda_{Di\perp} \to 0$. We first proceed by investigating the threshold conditions in the collisionless case before moving to a collisional situation. More details on the numerical procedure used to find zeros of the kinetic dispersion relation are provided in Appendix B.

### 3.3.1  Analysis of kinetic threshold conditions in the collisionless limit

#### 3.3.1.1  Without neglecting FLR corrections

In Fig. 3.6, we present the threshold conditions for the sheared CDEIA instability in a collisionless O$^+$ plasma with $v_i = v_e = 0$, for different anisotropy ratios $A_i$ and for a realistic perpendicular ion-to-electron temperature ratio of $\tau = 0.5$. The remaining input parameters are the same as the previous section (see Table 3.1). Figure 3.6 is comprised of two branches of solutions. The existence of the two branches in the kinetic regime is consistent with previous results from Perron *et al.* (2009). The first class of solutions corresponds to modes that are very sensitive to shears with nearly perpendicular wavevectors. We follow the same nomenclature as Perron *et al.* (2009) and name this group "lower branch" solutions because of their lower threshold drift requirements. The second class, which we
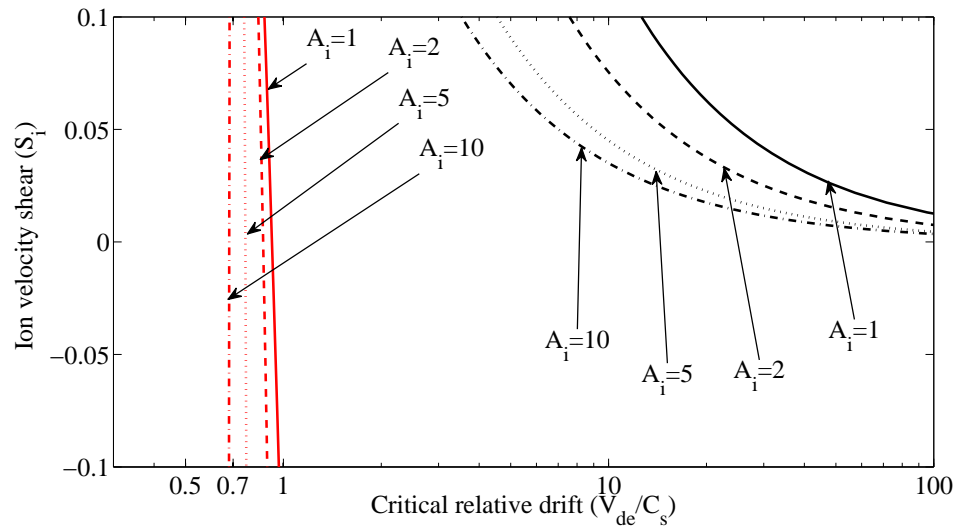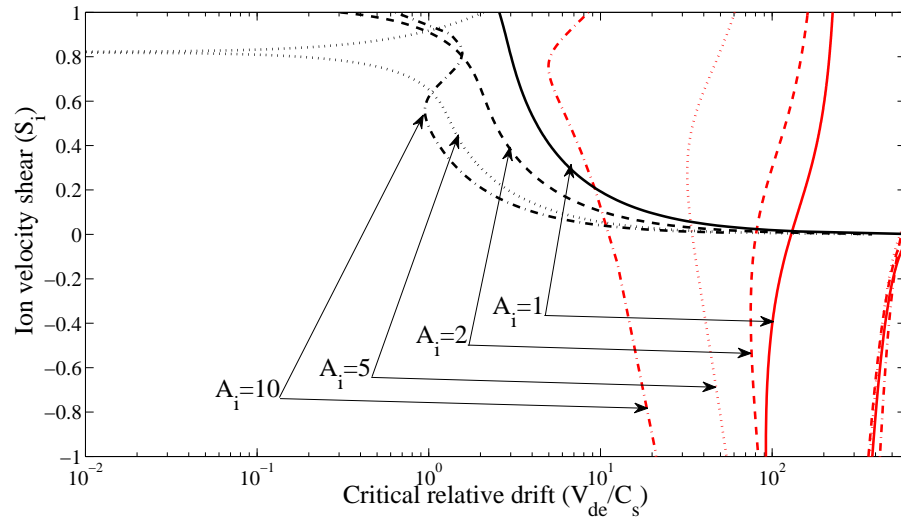
Figure 3.6: Threshold conditions for the sheared CDEIA instability in an anisotropic, collisionless $O^+$ plasma using the kinetic dispersion relation (3.2), with Eqs. (3.10)–(3.13), for $\tau = T_{\perp i}/T_e = 0.5$. Other input parameters are as per Table 3.1. The line scheme is the same as in Fig. 3.4. The red traces correspond to the upper branches solutions (large angles, decreasing from top to bottom, except for the folded portions at $V_{de}/C_s > 100$) and the black curves correspond to solutions for smaller angles (decreasing from top-left to bottom-right).

name "upper branch" solutions, refer to the modes that have more substantial deviations from perpendicularity and greater sensitivity to drifts. To differentiate these modes graphically in a manner consistent with the fluid study, upper branches solutions are traced in red and lower branches, in black. Note that there is only one set of red curves. Indeed, the latter curves are folded back to values of $V_{de}/C_s$ in excess of 300, for angles close to perpendicularity. This folding of the red traces is not apparent in Fig. 3.6 since it occurs at $S_i$ much larger (and negative) than -1. Nonetheless, since we are seeking to lower the drift requirements for possible instabilities, this portion of the red traces that involves large threshold drifts is of little physical interest. As far as near-perpendicular modes are concerned, the lower branches (black traces) are the only relevant ones.

In general, increasing the temperature ratio $\tau$ results in larger threshold drift requirements because of Landau damping. However, the lower branches are relatively insensitive to $\tau$ since they are still associated with significantly smaller drifts. In comparison with

previous results (Perron *et al.*, 2013), this is a new effect due to FLR contributions. For example, considering the isotropic case ($A_i = 1$), a shear of $S_i = 0.2$ lowers $V_{de}/C_s$ from approximately 100 to 10 (with respect to $S_i = 0$). Furthermore, Fig. 3.6 exhibits a lowering of both the upper and lower branches to smaller drifts as $A_i$ is increased from 1 to 10. For instance, an anisotropy ratio of 2 lowers the normalized critical drift ($V_{de}/C_s$) by 50% for near-perpendicular modes. Nonetheless, in this case, large shears with $S_i \sim 0.2$ are still required to achieve reasonable threshold relative drifts on the order of $V_{de} \sim$ 5-10$C_s$. From this, we can conclude that for a temperature ratio typical of F-region with $\tau = 0.5$, $A_i$ reduces the instability critical relative drift provided the wave speed $\omega/k$ is on the order of $0.5C_s$ and especially for modes propagating close to perpendicular to $\mathbf{B}_0$.

### 3.3.1.2 Neglecting FLR corrections

An example of kinetic threshold condition calculation in this limit is provided in Perron *et al.* (2013). Indeed, we showed that, in some cases, anisotropy significantly reduces the threshold drift for a large range of aspect angles, provided the wave speed is a fraction of the ion-acoustic speed ($\omega \sim 0.5kC_s$). For example, an anisotropy factor of 2 lowered the electron drift by a factor of approximately 50 (or approximately 40%) for $\tau = 0.5$, even with small or no shears.

### 3.3.2 Kinetic threshold conditions for a collisional plasma

In Fig. 3.7, we present the threshold conditions for the sheared CDEIA instability in a collisional O$^+$ plasma for $\tau = 0.5$ for the same parameters as before (Table 3.1). Similarly to the collisionless case (Sect. 3.3.1), two branches of solutions exist in the kinetic regime. The "lower branch" solutions are traced in black and the "upper branch" ones in red.

In the same way as the collisionless scenario, increasing the temperature ratio $\tau$ pushes the threshold loci up to higher drifts. Interestingly, in contrast with the fluid regime, the
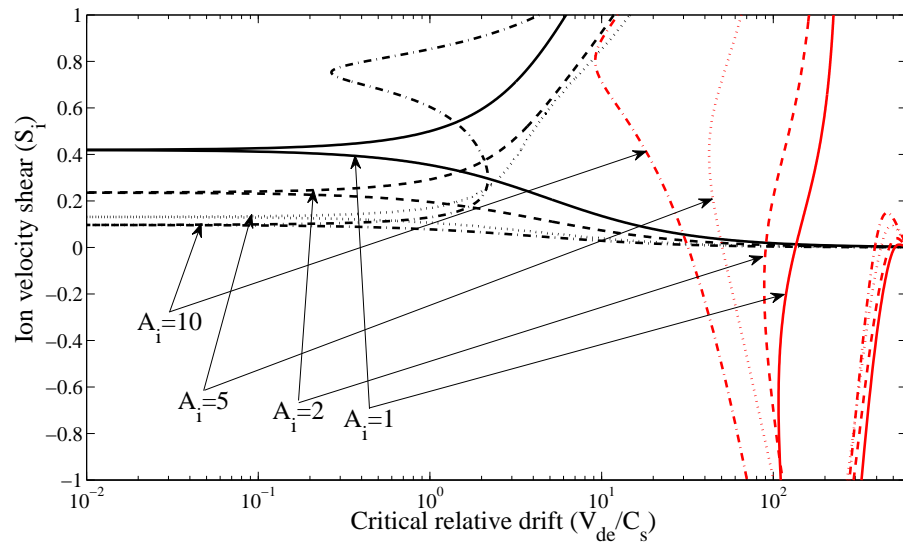
Figure 3.7: Threshold conditions for the sheared CDEIA instability in an anisotropic, collisional $O^+$ plasma using the kinetic dispersion relation (3.2), with Eqs. (3.10)–(3.13), for $\tau = 0.5$. Parameters that were held constant are as per Table 3.1. The line scheme is the same as in Fig. 3.6. The red traces correspond to the upper branche solutions (large angles, decreasing from top to bottom, except for the folded portions at $V_{de}/C_s > 100$) and the black curves correspond to solutions for smaller angles (decreasing from top to bottom).

effect of anisotropy on the "upper branches" mode is to lower the threshold drift require-ments. For example, the critical relative drift $V_{de}/C_s$ in zero-shear situations is decreased from approximately 150 to 100 as $A_i$ is increased from 1 to 2. Assuming that $C_s \sim 1500$ m/s, thermal electron drifts on the order of 150 km/s would still be required at threshold, a value that seems very high but not impossible based on recent reported FAC density mea-surements (assuming a plasma density of $n = 1 \times 10^{11} m^{-3}$, a relative drift of 150 km/s would be equivalent to a current density of $\sim 2.4 \ mA/m^2$). Therefore, for a temperature ratio typical of the F-region and for collisional situations, ion temperature anisotropy can lower the threshold drift required for the onset of CDEIA modes, with substantial deviation from perpendicularity.

In contrast with the "upper branches", the lower branch solutions are relatively insen-sitive to $\tau$, although the drift threshold minima are shifted up to slightly higher shears as compared with the fluid case (Fig. 3.2). Nonetheless, in a fashion similar to the fluid regime, increasing the anisotropy lowers the narrow angle minima of the small frequency ion shear driven mode to smaller shear requirements (the near-horizontal black curves are shifted to smaller values of $S_i$ as $A_i$ is increased). For example, minimal critical drifts could be achieved in presence of anisotropies $A_i \sim 2 - 10$ and shears $S_i \sim 0.1 - 0.4$. Assum-ing a gyrofrequency of $\Omega_i \sim 300 \ s^{-1}$, $V'_{di} \sim$ 30-120 m $s^{-1}$ m$^{-1}$ would still be required at threshold, a shear magnitude that appears to be larger than what has been observed to date in the high-latitude ionosphere. In the following section, we will investigate whether smaller shear threshold requirements for instability can be obtained by reducing the wave frequency since the fluid study indicated that the threshold conditions of the low-frequency ion shear-driven instability were mainly controlled by shears.

### 3.3.3 Reduction in threshold conditions when lowering the wave frequency under isotropic and anisotropic conditions

In Fig. 3.8, we present the kinetic threshold conditions corresponding to the "lower branches" as we reduce the wave frequency, under isotropic and anisotropic conditions with $A_i =$2 and for $\tau =$0.5. A summary of input parameters used here is provided in Table 3.2. In
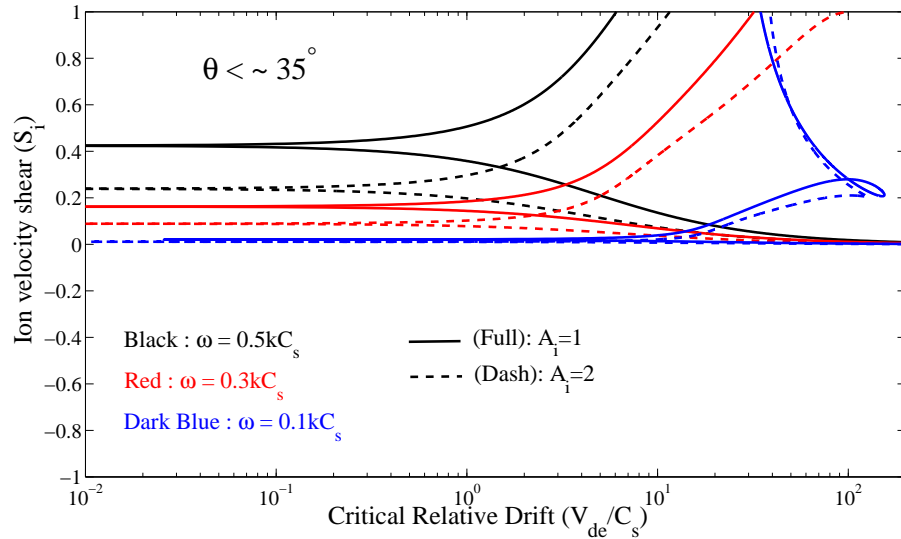
Figure 3.8: Reduction in threshold shear (associated with drift minima) when lowering the wave frequency under isotropic $A_i = 1$ (solid) and anisotropic conditions with $A_i = T_{\perp i}/T_{\parallel i} = 2$ (dashed), and for $\tau = 0.5$. $S_i$ as a function of $V_{de}/C_s$ is traced only for the lower branches solutions with $\theta \lesssim 35°$ for $\omega/kC_s = 0.5$ (black), 0.3 (red) and 0.1 (dark blue). The cyclotron and collision frequency parameters are as per Table 3.2.

Fig. 3.8, we show $S_i$ as a function of $V_{de}/C_s$ for $\omega/kC_s = 0.5$ (black), 0.3 (red) and 0.1 (dark blue) and for $A_i = 1$ (solid) and 2 (dashed). As expected, the decrease in frequency brings the threshold drift minima closer to zero shear. Additionally, a plausible ion temperature anisotropy of $A_i = 2$ contributes to the reduction in shear thresholds, although by a smaller amount as the wave frequency approaches zero. For example, threshold shears $S_i < 0.1$ can be attained for wave frequencies $\omega/kC_s \lesssim 0.3$ with ion anisotropies on the order of $A_i \sim 2$. Hence, for $\Omega_i \sim 300$ s$^{-1}$, our study suggests that $V'_{di} < 30$ m s$^{-1}$ m$^{-1}$ could be required at threshold. As we lower the frequency to $\omega/kC_s = 0.1$, the blue trace shows that the effects of anisotropy on the threshold conditions becomes vanishingly small. Interestingly, this effect is in line with what would be expected from the fluid expression (3.24) in spite of the fact that our calculations are not exactly complying with $\nu_i \gg \omega_R$.

| Frequencies | ion to electron mass ratio | Ion Gyrofrequency |
|---|---|---|
| $\omega/kC_s = 0.5, 0.3, 0.1$ | $m_i/m_e = 29166$ | $\Omega_i/kC_s = 2$ |
| Ion collision frequency | Electron to ion collision frequency ratio | Angles |
| $\nu_i/\Omega_i = 0.01$ | $\nu_e/\nu_i = 10$ | $0° < \theta = \mathrm{atan}(|k_\parallel|/k_\perp) \lesssim 35°$ |

Table 3.2: Summary of input parameters considered in Sect. 3.3.3.

### 3.3.4 Physical significance of varying the ion temperature anisotropy ratio

In this section, we discuss the physical significance of varying the ion temperature anisotropy ratio ($A_i = T_{\perp i}/T_{\parallel i}$). A similar consideration was presented by Spangler *et al.* (2002) and described in terms of real frequency and growth rate. In our calculations, we used normalization parameters that differ from those of Spangler *et al.* (2002) since we were interested in comparing our results with those of St-Maurice *et al.* (2007). The numerical solutions for the critical drift were normalized with the total ion-acoustic speed, using the total ion temperature expression $T_i = (T_{\parallel i} + 2T_{\perp i})/3$ (See Appendix B for more details). This permitted the expression of the kinetic dispersion relation in terms of dimensionless quantities such as $\tau = T_{\perp i}/T_e$ and $A_i$. Also, for given dimensionless input parameters, this normalization procedure allowed the comparison of solutions under various anisotropies while assuming that the total ion-acoustic speed remains constant.

In our computation of threshold conditions in the kinetic regime, we have held the perpendicular ion to electron temperature ratio $\tau$ constant while varying the anisotropy ratio $A_i$. Indeed, from Eq. B.2 (Appendix B), increasing $A_i$ while keeping $\tau$ constant would be equivalent to reducing $T_{\parallel i}$ and increasing $T_{\perp i}$ as well as $T_e$, assuming that $C_s$ remains constant. The increase in $T_{\perp i}$ affects the ion susceptibility $H_i$ (Eq. 3.10), in addition to $U_i$ (3.12), through the argument of the modified Bessel function $b_i = k_\perp^2 v_{\perp ti}^2/\Omega_i^2$. However, since $b_i$ is small for the ion-acoustic branch that we have considered herein, the effect of increasing

$T_{\perp i}$ on the instability threshold conditions should be also small, at least for large values of the wave vector angle. On the other hand, the effect of reducing $T_{\parallel i}$ on $H_i$ enters through the denominator of the argument of the plasma dispersion function Z. Furthermore, by taking the limit for which $k\lambda_{Di\perp} \to 0$, or equivalently $k\lambda_{De,i\parallel} \to 0$, we can express the dispersion relation such that $H_i/(1+U_i) + H_e/(1+U_e) = 0$. In this case, the relevant scaling factor between $H_i$ and $H_e$ becomes $A_i/\tau = T_e/T_{\parallel i}$. Therefore, we are led to a conclusion similar to Spangler *et al.* (2002) in that the lowering of instability threshold conditions might be explained, at least partly, by the reduced ion Landau damping that would be expected in a plasma with a lower parallel ion temperature with respect to the electron temperature.

We investigated the effects of varying the ion temperature anisotropy $A_i = T_{\perp i}/T_{\parallel i}$ while keeping the ratio $A_i/\tau = T_e/T_{\parallel i}$ constant on the kinetic threshold conditions. Put another way, the perpendicular ion to electron temperature ratio $\tau$ was increased by the same factor as $A_i$. This allows the verification of the contribution of $T_e/T_{\parallel i}$ in reducing the instability threshold conditions in presence of anisotropy. In Fig. 3.9, the threshold values of $S_i$ as a function of $V_{de}/C_s$ are traced for both the lower branches (black) with $\theta \lesssim 25°$ and the upper branches (red) for $A_i = 1, \tau = 0.25$ (solid); $A_i = 2, \tau = 0.5$ (dash); and $A_i = 4, \tau = 1$ (dot). As expected, under this restriction, increasing $A_i$ does not contribute significantly in reducing $V_{de}/C_s$ for modes propagating in directions far from perpendicular to $\mathbf{B}_0$ (red curves). Depending on the angle, the threshold drift is slightly upshifted or downshifted near $V_{de}/C_s \sim 100$. On the other hand, for $\theta \lesssim 25°$ (black curves), the effect of increasing $A_i$ is similar to the results of Sect. 3.3.2. Indeed, increasing $A_i$ leads to a reduction of the drift minimum to smaller shear requirements. Therefore, we are led to conclude that for directions close to perpendicular to the geomagnetic field, the increase in $T_{\perp i}$ plays a role more important than reducing the ratio $T_{\parallel i}/T_e$ in setting the conditions for instability.

## 3.4 Summary and Relevance to HF radar observations of ionospheric irregularities

In this chapter, we presented a new generalization of sheared and current-driven electrostatic ion-acoustic instability that includes ion temperature anisotropy, collisions and FLR
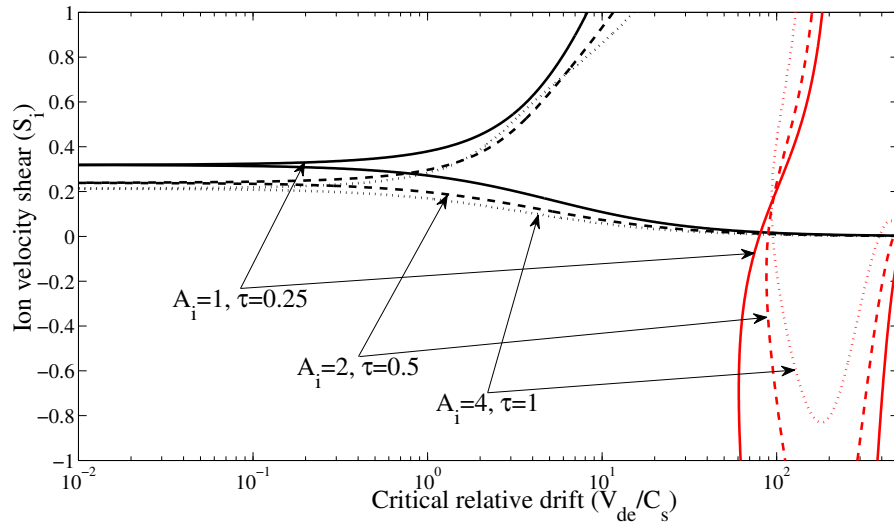
Figure 3.9: Effects of varying the ion temperature anisotropy $A_i = T_{\perp i}/T_{\|i}$ while keeping the ratio $A_i/\tau = T_e/T_{\|i}$ constant on the kinetic threshold conditions for $\omega/kC_s = 0.5$. Ion velocity shears $S_i$ as a function of $V_{de}/C_s$ is traced for both the lower branches (black) with $\theta \lesssim 25°$ and the upper branches (red) for $A_i = 1, \tau = 0.25$ (solid); $A_i = 2, \tau = 0.5$ (dash); and $A_i = 4, \tau = 1$ (dot). The cyclotron and collision frequencies are as per Table 3.2

corrections. This theory generalizes several mechanisms that have been proposed for the direct generation of decameter waves in the F-region.

We derived the final dispersion relation by considering electrostatic fluctuations and we used the local approximation ($k_x = 0$) in the weak shear limit. Also, we assumed quasi-neutrality, isotropic electron temperature, zero electron velocity shears and we allowed the ion temperature to be different in the direction parallel, $T_{\|i}$, and perpendicular, $T_{\perp i}$, to the magnetic field. Then, we investigated how the instability threshold conditions are affected by this new anisotropy consideration in the long wavelength ($k\lambda_{Di\perp} \to 0$) limit. The main findings are summarized.

### 3.4.1   In the topside F-region

In the topside ionosphere where we can neglect the influence of collisions, we have seen that, under fluid-like conditions, both ion temperature anisotropy and shears are capable of lowering the instability threshold drift requirements for oblique modes below the ion-acoustic speed of the medium

$$V_{de} = C_s \frac{\sqrt{1 - \zeta_i}}{\sqrt{1 + b_s A_i}}.$$

When FLR effects are included and for realistic anisotropy ratios, the instability appears to favor modes that are not propagating in a direction close to perpendicular to $\mathbf{B}_0$. This mechanism might contribute to the excitation of non field-aligned ion-acoustic waves that could be observed with ISRs, provided that the FAC densities are large enough.

As $T_e$ increases to a realistic value of $2T_{\perp i}$, the kinetic study showed that ion temperature anisotropy reduces the instability threshold drifts for a large range of intermediate aspect angles with respect to the direction perpendicular to the magnetic field. When FLR corrections are taken into account, anisotropies lower the threshold drift requirements for waves propagating almost perpendicularly to the geomagnetic field. Nevertheless, large ion velocity shears are required in order to attain threshold relative drifts on the order of $V_{de} \sim 5\text{-}10C_s$.

### 3.4.2   In the collisional F-region

In general, due to the dampening effect of collisions, the critical relative drifts are increased by approximately one order of magnitude. However, small drift and shear threshold conditions can be obtained in spite of collisions. In this case, the instability is restricted to very narrow angular intervals, close to the direction perpendicular to the geomagnetic field. This mode appears to be related to the small frequency ion shear driven instability discussed by Basu and Coppi (1988, 1989). In the fluid limit, anisotropies play a role in lowering the threshold conditions solely for modes close to being field-aligned, or propagating in a direc-

tion near perpendicular to the geomagnetic field. In fact, temperature anisotropies reduce the narrow angle threshold drift minima to smaller shear requirements.

When considering the weakly collisional shear-free and anisotropic limit $(\zeta_i \to 0, \omega_R > \nu_i)$ for which the wave vector direction is sufficiently far from perpendicularity $(k_\perp/k_\parallel \ll 1)$, we have shown that the resulting inertial low frequency mode in the absolute frame and in presence of ion temperature anisotropy is

$$\omega_R^A = \mathbf{k}_\perp \cdot \mathbf{V}_{\perp 0} + k_\parallel V_{di} \pm \frac{|k_\parallel| C_s}{\sqrt{1 + (T_{\perp i}/T_{\parallel i}) k_\perp^2 C_s^2/\Omega_i^2}}.$$

For SuparDARN applications at 10 meters, assuming that $C_s \sim 1500\ ms^{-1}$ in the F-region, the expression (3.34) can be simplified to

$$\omega_R^A = \mathbf{k}_\perp \cdot \mathbf{V}_{\perp 0} + k_\parallel V_{di} \pm \frac{|k_\parallel|}{k_\perp} \frac{T_{\parallel i}}{T_{\perp i}} \Omega_i. \tag{3.34}$$

Hence, under shearless and weakly collisional conditions, ion temperature anisotropy with $T_{\perp i} > T_{\parallel i}$ would lower the Doppler frequency shift that could be detected with SuperDARN HF radars. Once again, its aspect angle is such that the Doppler shift compared to the moving plasma is a substantial fraction of the ion acoustic speed. This mode would therefore not be seen to be drifting with the bulk perpendicular plasma flow. This mode would still require large parallel relative drifts [see Eq. (3.23)].

For a temperature ratio typical of F-region $(T_{\perp i}/T_e = 0.5)$, the anisotropy plays a role in lowering the threshold conditions of both the CDEIA mode, with substantial deviation from perpendicularity, and the small frequency ion shear-driven modes near perpendicular to the geomagnetic field. We found that increasing the ion temperature anisotropy lowers the narrow angle threshold drift minima to smaller shear requirements. Moreover, the threshold drift minima are further reduced to very small shear conditions for waves oscillating a lower frequencies. As a result, our study showed that $V_{di}' < 30\ ms^{-1}m^{-1}$ could be required at threshold, assuming that $\Omega_i \sim 300\ s^{-1}$, for wave frequencies $\omega/kC_s \lesssim 0.3$ and with ion anisotropies of the order $A_i \sim 2$. These modes have a ideal geometry to be observed with the Super Dual Auroral Radar Network (SuperDARN) array of HF radars,

which are pointing almost perpendicularly to the geomagnetic field. Nonetheless, these modes would be very aspect sensitive since they are restricted to very narrow angular intervals. In those situations, the Doppler shifts in the E×B moving frame would indeed be small ($\sim 45\ s^{-1}$ for $\lambda = 10\ m$ and $C_s \sim 1500\ ms^{-1}$). Nevertheless, this could account for discrepancies between the line-of-sight drifts and the line-of-sight component of the E×B drift of the order of several hundreds $ms^{-1}$. To our knowledge, there has not been a definitive experimental study of this possibility.

In closing, ion temperature anisotropy modifies the dispersion and threshold conditions of sheared and collisional CDEIA waves and instabilities. These instabilitites could take place, for instance, near the edges of auroral arcs, in presence of ion upflows and large parallel current densities. More importantly, realistic ion temperature anisotropies contribute to reduce the instability threshold velocity shears that are associated with relative drift minima for modes propagating almost perpendicularly to the geomagnetic field. Small shear thresholds that seem to be sustainable in the ionospheric F-region are obtained for low-frequency waves. Hence, this instability in the presence of ion temperature anisotropy might play a role in the direct generation of near field-aligned irregularities in the collisional F-region.

Chapter 4

# Effects of Ion Temperature Anisotropy and Shears on Theoretical Incoherent Scatter Radar (ISR) Spectra in the Topside High-Latitude F-Region

In the previous chapter, it was shown that ion temperature anisotropy modifies the dispersion and threshold conditions of sheared CDEIA instabilities. In collisional situations, ion temperature anisotropies contribute for the most part to reduce the threshold conditions of modes restricted to a very narrow angular interval and propagating in a direction near perpendicular to the geomagnetic field. Hence, this instability could play a role in the direct generation of near field-aligned irregularities that could potentially be observed with coherent HF radars. However, higher up in the topside ionosphere, we showed that the presence of ion temperature anisotropies (or at least the variation in the parallel ion to electron temperature ratio) lowers in some cases the threshold drift requirements for waves that are not necessarily field-aligned. In these cases, the instability would be propagating in oblique directions or close to being parallel to the magnetic field. This reduction in threshold conditions is particularly relevant for the present thesis since we are interested in possible generation mechanisms behind coherent ion-acoustic echoes, or NEIAL's, which are more often than not observed along the magnetic field or at large angles compared to the perpendicular. Therefore, owing to our interest in lowering the threshold conditions and to simplify the analysis, we chose to neglect the damping of small density fluctuations due to collisions.

In this chapter, we explore the possible contribution of additional physics (ion velocity shears and temperature anisotropy) in modifying the spectral density function (SDF). Although our original motivation is related to possible additional contributions in the CDEIA generation mechanism of NEIALs, using the linear theory only permits the computation of the SDF for a stable plasma. Nevertheless, these theoretical tools allow us to gain more insight on the extent for which the ISR spectrum can be affected by additional physics be-

fore the onset of microturbulences. In the process, we will investigate how the presence of a magnetic field affects ISR spectra especially for small aspect angles. In contrast with Chap. 3, we do not restrict our study to the IA branch. In other words, the argument of the exponentially scaled modified Bessel function of the first kind $k_\perp^2 \rho_{Li}^2$ is not limited to $\ll 1$, so that we ought to keep additional terms in the summation. First, we study the effects of ion temperature anisotropy on the shear-free SDF when ion gyroresonances are taken into account. Then we investigate possible spectral modifications that are due to the presence of ion velocity shears.

## 4.1 Basic Theory

In this section, we follow the kinetic approach for the theoretical calculation of ISR spectra given by Froula *et al.* (2010). The scattered power $P_s$ within frequency range $d\omega$ and solid angle $d\Omega$ is proportional to the spectral density function $S(\mathbf{k}, \omega)$

$$P_s d\omega d\Omega \propto n_{0e} S(\mathbf{k}, \omega) \tag{4.1}$$

where $n_{0e}$ is the unperturbed electron density. The SDF is defined as

$$S(\mathbf{k}, \omega) = \lim_{\gamma \to 0, V \to \infty} \frac{2\gamma}{V} \left\langle \frac{|n_e(\mathbf{k}, \omega - i\gamma)|^2}{n_{e0}} \right\rangle \tag{4.2}$$

where $\mathbf{k}$ is the difference between scattered and incident wavevectors ($\mathbf{k} = \mathbf{k}_s - \mathbf{k}_i$), $\omega$ is the frequency shift of the scattered radiation from the incident radiation ($\omega = \omega_s - \omega_i$), $\gamma$ is the wave growth rate, $V$ is the scattering volume and $n_e(\mathbf{k}, \omega - i\gamma)$ is the Fourier transform in space and Laplace transform in time of the fluctuating electron density. The brackets denote the ensemble average. Hence, the net scattering comes from the plasma fluctuations, which can be related to the Fourier-Laplace transform of the electron density.

### 4.1.1 Unmagnetized spectrum

The term "unmagnetized" does not mean that the unperturbed ion motion is not gyrating aroung magnetic field lines, but rather that the external magnetic field does not interfere

with the characteristics of the ion density fluctuations through ion gyroresonances (Raman, 1980). In taking the ensemble averages, the most probable initial velocity distribution functions, $f_{0i}(\mathbf{v}, 0)$ and $f_{0e}(\mathbf{v}, 0)$, are used as weighting factors. An expression for the fluctuating density, $n_e(\mathbf{k}, \omega - i\gamma)$, can be derived by performing a Fourier-Laplace transform of the Vlasov equation (Eq. 1.8). If the charges are initially uncorrelated, the cross terms in the ensemble average are zero (Froula *et al.*, 2010, page 53), and then

$$S(\mathbf{k}, \omega) = \frac{2\pi}{k} \left| 1 - \frac{\chi_e}{\varepsilon} \right|^2 f_{e0}\left(\frac{\omega}{k}\right) + \frac{2\pi Z}{k} \left| \frac{\chi_e}{\varepsilon} \right|^2 f_{i0}\left(\frac{\omega}{k}\right) \qquad (4.3)$$

where $Z$ is the ion charge, $\varepsilon = 1 + \chi_e(k, \omega) + \chi_i(k, \omega)$ is the longitudinal dielectric function in an unmagnetized plasma and $\chi_j$ is the permittivity of species $j$. The first term is the electron component and the second term corresponds to the ion component. The collective effects are contained in the longitudinal dielectric function $\varepsilon$. The SDF will be enhanced significantly when $|\varepsilon|^2$ is small, or at the natural resonances of the plasma. In the unmagnetized case, these resonances correspond to the electron plasma frequency and the ion-acoustic resonance. It should be emphasised that the previous expression for $S(\mathbf{k}, \omega)$ is also valid for initial nonequilibrium velocity distributions provided that the plasma is close to equilibrium (Froula *et al.*, 2010, page 53). For example, we can include the effects of a relative drift between populations or temperature anisotropy as long as the calculations for the SDF are done for a stable plasma.

## 4.1.2 Magnetized spectrum with ion gyroresonances

Assuming the plasma is initially close to equilibrium and the charges of which are uncorrelated, the SDF for a magnetized $O^+$ plasma (with a charge $Z = 1$) can be expressed as (Froula *et al.*, 2010, p.284)

$$S(\mathbf{k}, \omega) = 2 \lim_{\gamma \to 0} \gamma \left( \left| 1 - \frac{H_e}{\varepsilon} \right|^2 \int_{-\infty}^{\infty} \frac{d\mathbf{v} \sum_l J_l^2(k_\perp \rho_{Le}) f_{e0}(\mathbf{v})}{(\omega - k_\| v_\| - l\Omega_e)^2 + \gamma^2} + \qquad (4.4)$$

$$\left| \frac{H_e}{\varepsilon} \right|^2 \int_{-\infty}^{\infty} \frac{d\mathbf{v} \sum_m J_m^2(k_\perp \rho_{Li}) f_{i0}(\mathbf{v})}{(\omega - k_\| v_\| - m\Omega_i)^2 + \gamma^2} \right)$$

where $J(k_\perp \rho_{Lj})$ is the Bessel function of the first kind and $\rho_{Lj}$ is the $j$th species Larmor radius. The longitudinal dielectric function is $\varepsilon = 1 + H_e(k, \omega) + H_i(k, \omega)$ and $H_j$ is the permittivity of species $j$ in a magnetized plasma.

| Incident wavelength | Magnetic field | Plasma density |
| --- | --- | --- |
| $\lambda_0 \approx 1.34\ m$ | $B = 0.6 \times 10^{-4}\ T$ | $n_e = 1 \times 10^{11}\ m^{-3}$ |
| Electron temperature | Ion to electron mass ratio | Collision frequencies |
| $T_e = 2000\ K$ | $m_i/m_e = 29166$ | $\nu_e = \nu_i = 0$ |

Table 4.1: Summary of parameters that have been kept constant in the calculation of ISR spectra for EISCAT VHF at 224MHz.

### 4.1.3   Comparison of magnetized and unmagnetized spectra

Calculations of ISR spectra were done for EISCAT VHF radar, located near Tromsø, at a latitude of $\sim 66°$. Among the incoherent scatter radars operating at high-latitudes, the signal emitted by EISCAT VHF has the longest wavelength. Since IA waves are more easily destabilized at longer wavelengths, this choice should provide interesting examples of ISR spectra that are more enhanced than spectra corresponding to larger frequencies (smaller wavelengths). In the case of EISCAT VHF, the incident wavelength is $\lambda_0 = c/f_0 = 300/224 \approx 1.34\ m$. As we discussed in Chap. 1, for a monostatic radar with a probing wavelength $\lambda_0$, the corresponding wavelength matching Bragg condition for coherent scattering is $\lambda = \lambda_0/2$. Hence, EISCAT VHF radar is looking at waves modes propagating along the radar line-of-sight having a wavelength of $\approx 0.67\ m$. A summary of parameters that were fixed for our calculations in this chapter are presented in Table 4.1.

It is generally believed that the effects of the magnetic field are important only when the radar probing direction is almost perpendicular to the magnetic field $\mathbf{B}_0$ (for example, see Farley *et al.*, 1961, Froula *et al.*, 2010). For perpendicular directions, gyroresonance effects would be recognized through the appearance of Bernstein modes modulating the spectrum. This is illustrated in Fig. 4.1 where we compare the theoretical SDF for the EISCAT VHF radar in unmagnetized and magnetized Maxwellian $O^+$ plasmas at several wave vector angles. Indeed, the shape of the spectrum in a magnetized plasma begins to
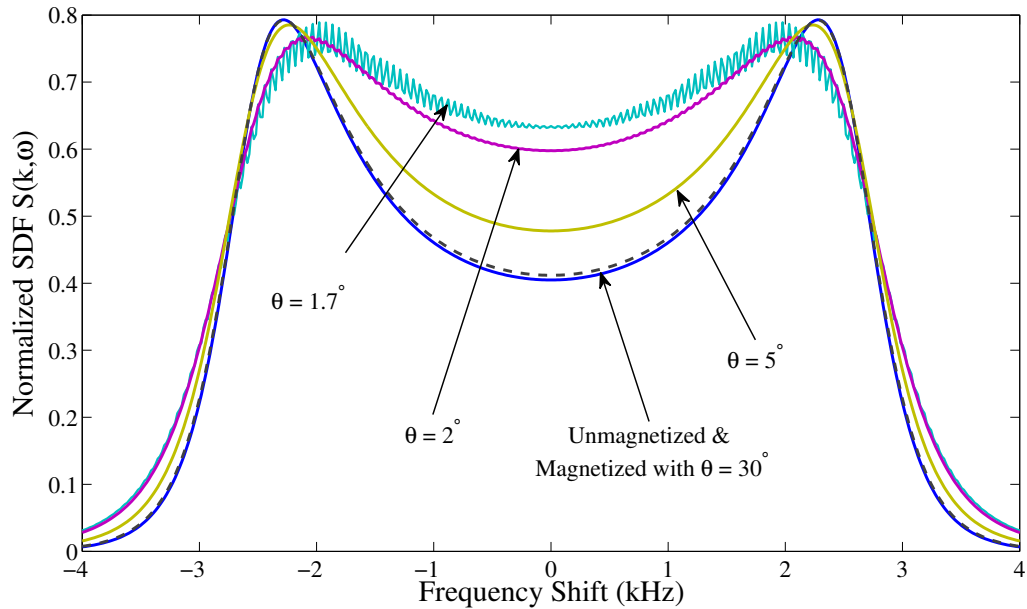
Figure 4.1: Comparison of theoretical EISCAT VHF 224MHz normalized SDF in unmagnetized (blue) and magnetized Maxwellian plasmas at $\theta = 30°$ (dash grey), $5°$ (gold), $2°$ (purple) and $1.7°$ (aquamarine). Equation (4.3) was used to compute the unmagnetized spectrum (blue) and Eq. (4.4) for the magnetized ones. Other input parameters are as per Table 4.1.

deviate significantly from the unmagnetized case when $\theta = 5°$. The Bernstein modes are noticeable at $\theta = 2°$ and are clearly evident for smaller angles.

## 4.2  Ion Temperature Anisotropy Effects on ISR Spectra

### 4.2.1  Derivation of the spectral density function $S(\mathbf{k}, \omega)$ for bi-Maxwellian plasmas with ion gyroresonances

Using a drifting Maxwellian distribution function for the electrons

$$f_{0e}(\mathbf{v}) = \left( \frac{m}{2\pi k_B T_e} \right)^{3/2} e^{-mv_{\perp}^2/2k_B T_e} e^{-m(v_{\parallel}-V_d)^2/2k_B T_e} \tag{4.5}$$

and a bi-Maxwellian for the ions

$$f_{0i}(\mathbf{v}) = \left( \frac{m}{2\pi k_B} \right)^{3/2} \frac{1}{T_{\perp i} T_{\parallel i}^{1/2}} e^{-mv_{\perp}^2/2k_B T_{\perp i}} e^{-mv_{\parallel}^2/2k_B T_{\parallel i}} \tag{4.6}$$

the previous integrals of the electron and ion components in Eq. 4.4 can be re-written respectively as

$$\int_{-\infty}^{\infty} \frac{d\mathbf{v} \sum_l J_l^2(k_\perp \rho_{Le}) f_{e0}(\mathbf{v})}{(\omega - k_\parallel v_\parallel - l\Omega_e)^2 + \gamma^2} = \tag{4.7}$$

$$\left(\frac{\beta_e}{\pi}\right)^{3/2} \int_0^{2\pi} d\phi \int_0^{\infty} v_\perp dv_\perp \sum_l J_l^2(k_\perp \rho_{Le}) e^{-\beta_e v_\perp^2} \int_{-\infty}^{\infty} \frac{dv_\parallel e^{-\beta_e(v_\parallel - V_{de})^2}}{(\omega - k_\parallel v_\parallel - l\Omega_e)^2 + \gamma^2}$$

where $\beta_e = m_e/2k_B T_e = 1/2v_{te}^2$, $\rho_{Le} = \sqrt{v_{te}/\Omega_e}$, and

$$\int_{-\infty}^{\infty} \frac{d\mathbf{v} \sum_m J_m^2(k_\perp \rho_{Li}) f_{i0}(\mathbf{v})}{(\omega - k_\parallel v_\parallel - m\Omega_i)^2 + \gamma^2} = \tag{4.8}$$

$$\frac{\beta_{\perp i}\sqrt{\beta_{\parallel i}}}{\pi^{3/2}} \int_0^{2\pi} d\phi \int_0^{\infty} v_\perp dv_\perp \sum_m J_m^2(k_\perp \rho_{Li}) e^{-\beta_{\perp i} v_\perp^2} \int_{-\infty}^{\infty} \frac{dv_\parallel e^{-\beta_{\parallel i} v_\parallel^2}}{(\omega - k_\parallel v_\parallel - l\Omega_e)^2 + \gamma^2}$$

where $\beta_{\parallel i} = m_i/2k_B T_{\parallel i} = 1/2v_{\parallel ti}^2$, $\beta_{\perp i} = m_i/2k_B T_{\perp i} = 1/2v_{\perp ti}^2$ and $\rho_{Li} = \sqrt{v_{\perp ti}/\Omega_i}$. Using the usual identity for the integrals of Bessel functions (Watson, 1944, p.396), Eq. (4.4) becomes

$$S(\mathbf{k}, \omega) = 2\lim_{\gamma \to 0} \gamma \left( \left|1 - \frac{H_e}{\varepsilon}\right|^2 \sqrt{\frac{\beta_e}{\pi}} \sum_l \Gamma(b_e) \int_{-\infty}^{\infty} \frac{dv_\parallel e^{-\beta_e(v_\parallel - V_{de})^2}}{(\omega - k_\parallel v_\parallel - l\Omega_e)^2 + \gamma^2} \right. \tag{4.9}$$

$$\left. + \left|\frac{H_e}{\varepsilon}\right|^2 \sqrt{\frac{\beta_{\parallel i}}{\pi}} \sum_m \Gamma(b_i) \int_{-\infty}^{\infty} \frac{dv_\parallel e^{-\beta_{\parallel i} v_\parallel^2}}{(\omega - k_\parallel v_\parallel - m\Omega_i)^2 + \gamma^2} \right)$$

where $b_e = k_\perp^2 \rho_{Le}^2$ and $b_i = k_\perp^2 \rho_{Li}^2 = k_\perp^2 v_{\perp ti}^2/\Omega_i^2$ is the argument of the exponentially scaled modified Bessel function of the first kind, following the same nomenclature as in Chap. 3. The previous integrals for the electron and ion components can be re-written, respectively, as

$$\int_{-\infty}^{\infty} \frac{dv_\parallel e^{-\beta_e(v_\parallel - V_{de})^2} \left(\frac{\beta_e}{k_\parallel^2}\right)}{(v_\parallel \sqrt{\beta_e} - (\omega - l\Omega_e)\sqrt{\beta_e}/k_\parallel)^2 + (\gamma\sqrt{\beta_e}/k_\parallel)^2} \tag{4.10}$$

and

$$\int_{-\infty}^{\infty} \frac{dv_\parallel e^{-\beta_{\parallel i} v_\parallel^2} \left(\frac{\beta_{\parallel i}}{k_\parallel^2}\right)}{(v_\parallel \sqrt{\beta_{\parallel i}} - (\omega - m\Omega_i)\sqrt{\beta_{\parallel i}}/k_\parallel)^2 + (\gamma\sqrt{\beta_{\parallel i}}/k_\parallel)^2}. \tag{4.11}$$

Using the following identity (Froula *et al.*, 2010, p.386)

$$\int_{-\infty}^{\infty} \frac{f(v)dv}{(v - z_{Re})^2 + z_{Im}^2} = \frac{\pi}{z_{Im}} f(z_{Re}) \tag{4.12}$$

the integration over $v_\parallel$ gives

$$S(\mathbf{k},\omega) = \frac{\sqrt{2\pi}}{k_\parallel v_{te}} \left| 1 - \frac{H_e}{\varepsilon} \right|^2 \sum_l \Gamma(b_e) e^{-\left(\frac{\omega - k_\parallel V_{de} - l\Omega_e}{\sqrt{2}k_\parallel v_{te}}\right)^2} + \frac{\sqrt{2\pi}}{k_\parallel v_{\parallel ti}} \left| \frac{H_e}{\varepsilon} \right|^2 \sum_m \Gamma(b_i) e^{-\left(\frac{\omega - m\Omega_i}{\sqrt{2}k_\parallel v_{\parallel ti}}\right)^2}.$$

$$(4.13)$$

For $\omega \ll \Omega_e$ or $\rho_{Le} \to 0$, the spectrum in the ionosphere is affected only by ion gyrores-onances since the electron Larmor radius is very small compared with the probing wave-length (Raman, 1980). In this case, the $l \neq 0$ terms in Eq. (4.13) become negligeable, $\Gamma_0(b_e) \to 1$, and we write

$$S(\mathbf{k},\omega) = \frac{\sqrt{2\pi}}{k_\parallel v_{te}} \left| 1 - \frac{H_e}{\varepsilon} \right|^2 e^{-\left(\frac{\omega - k_\parallel V_{de}}{\sqrt{2}k_\parallel v_{te}}\right)^2} + \frac{\sqrt{2\pi}}{k_\parallel v_{\parallel ti}} \left| \frac{H_e}{\varepsilon} \right|^2 \sum_m \Gamma(b_i) e^{-\left(\frac{\omega - m\Omega_i}{\sqrt{2}k_\parallel v_{\parallel ti}}\right)^2} \quad (4.14)$$

This result is equivalent to the expression that was derived by Shume (2000) using a differ-ent approach. However, Shume (2000) studied the effects of temperature anisotropies on the ISR gyro lines and did not consider anisotropy effects on the ion line.

## 4.2.2 Electrostatic dispersion relation for bi-Maxwellian plasmas

As indicated before, the electrostatic dispersion relation in a magnetized hot plasma, which corresponds to the zeros of the dielectric function, is given by

$$\varepsilon = 1 + H_e(k,\omega) + H_i(k,\omega) = 0. \quad (4.15)$$

From Eqs. (3.10) and (3.11), by taking the collisionless ($\nu_{i,e} \to 0$) and shear-free ($S_i \to 0$) limit, the ion susceptibility becomes

$$H_i = \frac{1}{k^2 \lambda_{Di\perp}^2} \left[ \frac{T_{\perp i}}{T_{\parallel i}} + \sum_n \Gamma_n(b_i) \left( \frac{\omega}{\sqrt{2}|k_\parallel| v_{\parallel ti}} \right) \left( \frac{n\Omega_i}{\omega} \left( 1 - \frac{T_{\perp i}}{T_{\parallel i}} \right) + \frac{T_{\perp i}}{T_{\parallel i}} \right) Z \left( \frac{\omega - n\Omega_i}{\sqrt{2}|k_\parallel| v_{\parallel ti}} \right) \right]$$

$$(4.16)$$

where, in this case, $b_i = k_\perp^2 v_{\perp ti}^2 / \Omega_i^2$, and the electron susceptibility is

$$H_e = \frac{1}{k^2 \lambda_{Di\perp}^2} \frac{T_{\perp i}}{T_e} \left[ 1 + \left( \frac{\omega - k_\parallel V_{de}}{\sqrt{2}|k_\parallel| v_{te}} \right) Z \left( \frac{\omega - k_\parallel V_{de}}{\sqrt{2}|k_\parallel| v_{te}} \right) \right]. \quad (4.17)$$

### 4.2.3 Computation of ISR spectra for stable plasmas under various ion temperature anisotropies

Inspecting Eq. (4.14), it appears that ion temperature anisotropy will contribute to $S(k,\omega)$ through the dielectric function $\varepsilon$ in the denominators of both terms. Also, the relevant temperature in the argument of the modified Bessel function of the first kind, $b_i$, is the perpendicular temperature, $T_{\perp i}$, whereas the relevant thermal velocity in the denominator of the second term (as well as in the denominator of the exponential) is the parallel temperature.

We undertook the computation of the EISCAT VHF (224MHz) SDF for different anisotropies ($A_i = 1, 2$ and 3) and in a direction close to parallel to the magnetic field, in this case $\theta = 80°$. In all our computations of Eqs. (4.14) and (4.16), we included terms in the summation of Bessel functions up to order $n = 200$. This proved to be sufficient since the terms become vanishingly small for $n \gtrsim 50$.

An example of ISR spectrum calculation is shown in the upper panel of Fig. 4.2. Indeed, for the same total ion temperature, $T_i$, both IA peaks are enhanced as the anisotropy ratio increases. This is probably due to the fact that, by increasing $T_{\perp i}/T_{\|i}$, we are effectively reducing the ratio $T_{\|i}/T_e$. This explanation goes along with the expected reduced ion Landau damping associated with a lower parallel ion temperature with respect to the electron temperature. Since we have ISR observations in mind, this example raises the question of how to properly interpret ISR data acquired along a particular line of sight. The distribution function being anisotropic, the "temperature" should also change with the radar probing direction. In the following section, we compare this result with unmagnetized spectra that would be associated with the effective temperature along the radar line of sight.
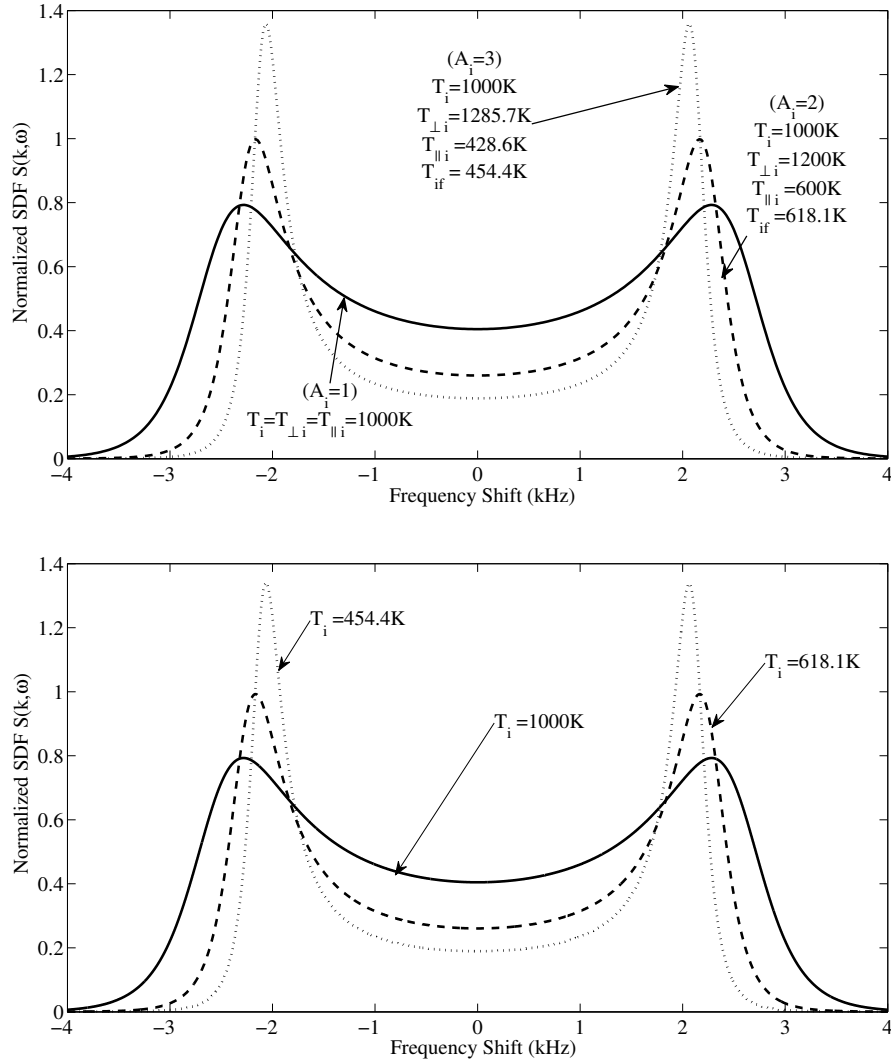
Figure 4.2: Variation of the EISCAT VHF 224MHz normalized SDF in a magnetized Maxwellian plasma with the ion temperature anisotropy ratio $A_i = T_{\perp i}/T_{\|i}$. Equation (4.4) is traced in the upper panel for $A_i$ from 1 (solid), 2 (dashed) and 3 (dotted). The equivalent effective ion temperature $T_{if}$ [Eq. (4.18)] is also indicated in the upper panel. In the lower panel, the SDF in an unmagnetized plasma [Eq. (4.3)] is plotted for $T_i$ from $1000K$ (solid), $618.1K$ (dashed) and $454.4K$ (dotted). In both panels, $\theta = 80°$ and $V_{de}/C_s = 0$. Other parameters are as per Table 4.1.

### 4.2.4 Using the critical angle to remove the ambiguity between effective and total ion temperatures

In their analysis, Raman *et al.* (1981) neglected ion gyroresonance effects in presence of a magnetic field assuming that the radar probing direction was more than $15°$ away from perpendicularity. In other words, they considered both the electrons and the ions to be "unmagnetized". In this case, they showed that SDF's for bi-Maxwellian ion velocity distributions are functionally similar to Maxwellian distributions, with the effective ion temperature, $T_{if}$, along the radar line-of-sight replacing the true ion temperature (Raman *et al.*, 1981). The effective ion temperature along the line of sight is related to the parallel and perpendicular temperatures via the following equation (Raman *et al.*, 1981)

$$T_{if} = T_{\parallel i}\cos^2\phi + T_{\perp i}\sin^2\phi \qquad (4.18)$$

where $\phi$ is the angle between $\mathbf{k}$ and $\mathbf{B}_0$. From Eqs. (1.12) and (4.18), we find that $T_i = T_{if}$ when $\phi = \phi_c = 54.7°$ or equivalently, when the aspect angle (with respect to the direction perpendicular to $\mathbf{B}_0$) is $\theta = 35.3°$. This critical angle proves to be useful since the ambiguity between the effective temperature and the true (average) temperature can be removed.

In the lower panel of Fig. 4.2, we plotted the SDF in an unmagnetized plasma [Eq. (4.3)] using the equivalent effective ion temperatures, $T_{if}$, that are associated with $\theta = 80°$. Surprisingly, comparing the ISR spectrum in the upper panel with the one in the lower panel, we find that they are effectively similar. We have verified this result for several aspect angles that are large enough. Consequently, we confirm that the assumption made by Raman *et al.* (1981) is in fact valid, namely that ion gyroresonance effects can be neglected even for a bi-Maxwellian plasma, at least when the radar probing direction is far from orthogonal to $\mathbf{B}_0$.

This previous result is presented differently in Fig. 4.3 where we computed the SDF for $A_i = 1$ and 2, but this time, at the critical angle. Indeed, this example shows that the presence of ion temperature anisotropy is in fact unimportant at the critical angle since the radar is measuring the same total ion temperature. In the following section, we explore
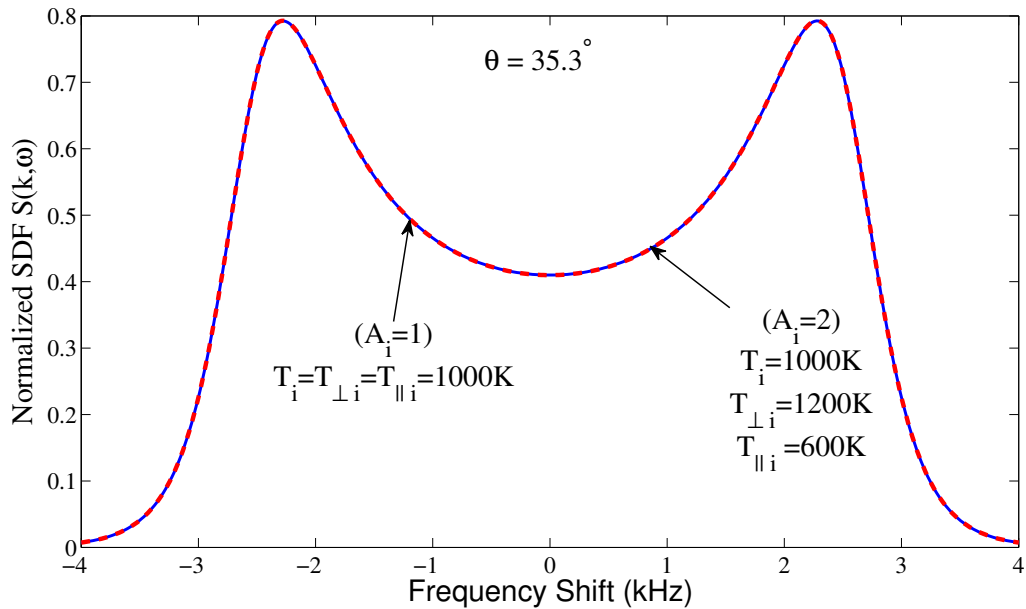
Figure 4.3: Theoretical EISCAT VHF 224MHz normalized SDF in a magnetized Maxwellian plasma [Eq. (4.4)] at the critical angle $\theta = 35.3°$. The blue curve corresponds to an isotropic ion temperature with $T_i = T_{\perp i} = T_{||i} = 1000K$. The red-dashed trace corresponds to an anisotropy ratio of $A_i = 2$ with $T_i = 1000K$, $T_{\perp i} = 1200K$ and $T_{||i} = 600K$. Other parameters are as per Table 4.1.

whether an anisotropic plasma could influence the spectrum for small aspect angles.

### 4.2.5 Effects of ion temperature anisotropies on ISR spectra for small aspect angles

Figure 4.4 shows the normalized SDF [Eq. (4.4)] at $\theta = 2°$. The blue curve corresponds to an isotropic ion temperature with $T_i = T_{\perp i} = T_{||i} = 1000K$. The green trace corresponds to an anisotropy ratio of $A_i = 2$ with $T_i = 1000K, T_{\perp i} = 1200K$, $T_{||i} = 600K$ and with an effective ion temperature of $T_{if} = 1199.3K$. The red line corresponds to an isotropic ion temperature with $T_i = T_{\perp i} = T_{||i} = T_{if} = 1199.3K$. By comparing the green and red curves, it is evident that, for angles close to perpendicular to $\mathbf{B}_0$, the spectrum "seen" by the radar (green) would be very different than the expected spectrum associated with the effective ion temperature. In this case, the effect of ion temperature anisotropy is to enhance the contribution from the gyroresonances. This enhancement in the Berstein modes might be an indication that the plasma could become unstable under the Harris instability mechanism
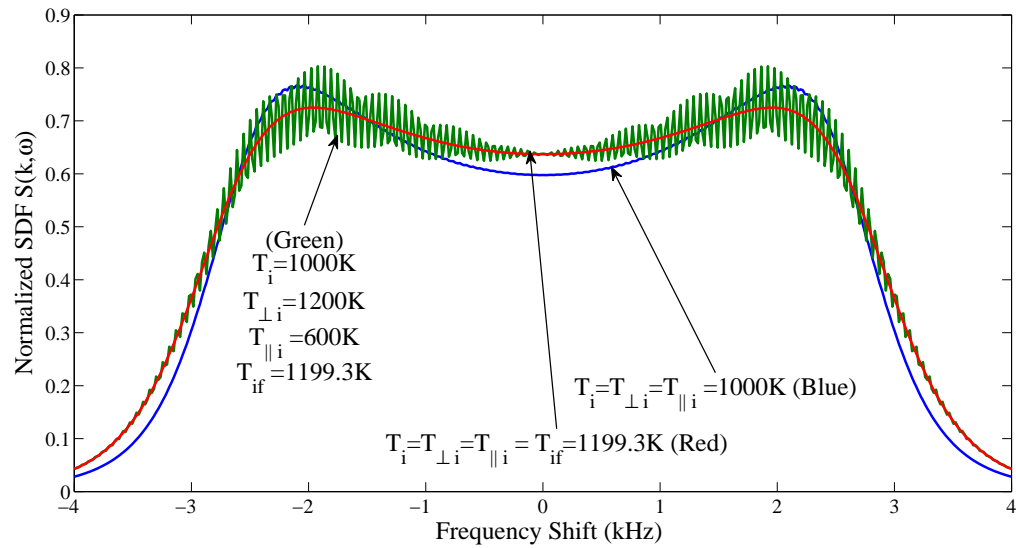
Figure 4.4: Theoretical EISCAT VHF 224MHz normalized SDF in a magnetized Maxwellian plasma [Eq. (4.4)] at $\theta = 2°$. The blue curve corresponds to an isotropic ion temperature with $T_i = T_{\perp i} = T_{\parallel i} = 1000K$. The green trace corresponds to an anisotropy ratio of $A_i = 2$ with $T_i = 1000K, T_{\perp i} = 1200K$, $T_{\parallel i} = 600K$ and with an effective ion temperature of $T_{if} = 1199.3K$. The red line corresponds to an isotropic ion temperature with $T_i = T_{\perp i} = T_{\parallel i} = T_{if} = 1199.3K$. Other parameters are as per Table 4.1.

in an anisotropic plasma (Harris, 1959, 1961). Indeed, McCune (1965) had shown that the plasma can be unstable when the perpendicular temperature is larger than the parallel one ($T_\perp > T_\parallel$) (see also the review by Hall *et al.*, 1965). This type of instability occurs near cyclotron frequency and its harmonics. We chose not to investigate this effect any further since there are very few ISR applications or observations near perpendicularity to $\mathbf{B}_0$ to our knowledge.

## 4.3   Ion Velocity Shears Effects on ISR spectra

In this section, we investigate how the presence of ion velocity shears could modify the shape of ISR spectra. It was suggested by Gavrishchaka *et al.* (1998) that the critical drift for the CDEIA instability is reduced significantly if there is a transverse gradient in the relative magnetic field aligned drift. However, it has been shown in St-Maurice *et al.* (2007) and Perron *et al.* (2009) that the situation is more complicated than previously claimed for

realistic shears and that instability threshold conditions are highly variable depending on wave vector angle. At any rate, the ion susceptibility function $H_i$ is modified by shears and it appears worthwhile to study how it might affect the shape of ISR spectra for stable modes. To this end, we must first determine the range of validity associated with the theoretical assumptions used to calculate the SDF for a weakly inhomogeneous plasma.

The local approximation allows the derivation of linear susceptibilities that are independent of position x for weakly inhomogeneous plasmas. According to Gary and Schwartz (1980), the local approximation in the case of velocity gradients requires that $\lambda = 2\pi/k < \varepsilon_{V_{dj}}^{-1}$ where $\varepsilon_{V_{dj}} = (1/V_{dj})dV_{dj}/dx$ is the inverse "drift velocity gradient" scale length. Stated differently, the condition $L_s k > 1$ must be satisfied, which means that the spatial scale length ($L_s$) associated with the hydrodynamic drift velocity gradient must be larger than the probing radar half-wavelength $L_s > \lambda$. In order to observe plasma collective effects, the probing half-wavelength must be larger than the Debye length. Hence, the previous condition can be further refined such that $L_s > \lambda > \lambda_{Di}$. Finally, in accordance with the local theory, the wave vector is aligned in a plane perpendicular to the spatial inhomogeneity ($k_x = 0$). This assumption would translate into having a radar looking in a direction perpendicular to the gradient in field-aligned drift velocity.

Since we assume that the plasma is initially close to equilibrium, we neglect the effects of correlations in the initial state (Froula *et al.*, 2010, page 53). This assumption also requires that the radar averaging integration time be larger than plasma characteristic time scales such that $T \gg 1/\omega_{pe}$ (Froula *et al.*, 2010, page 57). In a manner consistent with the local approximation, we assume that the shears are small. Therefore, in taking the ensemble average, we use a Maxwellian velocity distribution as the most probable initial state of the velocity weighting factor.

Swartz *et al.* (1988) investigated the spectral effects of large perpendicular velocity shears, unresolved within the radar scattering volume or time integration, in an attempt to find an alternative explanation to non-Maxwellian interpretation of spectral shapes. In

other words, they simulated an ISR spectrum that included the effects of unresolved shears. As pointed out by St-Maurice (2003), the main criticism for this study was the likely wrong assumption that Maxwellians provided valid description of the radar cross section in situations of mesoscale turbulence. A similar proposal was made by Knudsen *et al.* (1993) in an effort to explain large ion temperature anisotropies observed with EISCAT. In this case, the authors suggested that turbulent plasma flows with peak amplitudes of $\sim 2km/s$ unresolved within the scattering volume or time integration can explain the ion temperature amplitudes and anisotropy. Once again, this work was criticized based on the premise that a Maxwellian is an adequate starting point for the description of the velocity distribution (St-Maurice, 2003). Nevertheless, these papers showed that mesoscale shears affect ISR scattering through a convolution of spectra over a range of differing velocities.

In contrast with the previous studies, we consider smaller shears that are associated with larger gradient scale lengths. To be on the safe side, the velocity gradient scale length should be larger than the scales associated with the scattering volume, so that the homogeneity assumption is almost fullfiled. In ballpark numbers, the gradient should be larger than a few tens of km, depending on the altitude and range gate under consideration. In addition, for our analysis to be valid, the shears must be small enough for the plasma to be described with Maxwellian distribution functions. In addition, the shears and the drift velocities ought to be small enough for the plasma to remain stable, allowing the computation of SDF locally. In other words, we investigate how the presence of large-scale velocity gradients could influence the properties of $S(k, \omega)$ before the onset of microturbulences.

### 4.3.1  Electrostatic dispersion relation for sheared and Maxwellian plasmas

In this section, we limit our study to the case where $v_{i,e} \to 0$, or equivalently $U_{i,e} \to 0$, $A_i = T_{\perp i}/T_{\parallel i} \to 1$ and for which the argument of the modified Bessel function is small

$(k_\perp \rho_{Li} = k_\perp v_{ti}^2/\Omega_i^2 \ll 1)$, so that $\Gamma_n^* \approx \Gamma_n$. As a result, Eq. (3.10) is reduced to

$$H_i = \frac{1}{k^2\lambda_{Di}^2}\left[1 + \sum_n \Gamma_n(b_i)\left(\frac{\omega}{\sqrt{2}|k_\|||v_{ti}}\right)Z\left(\frac{\omega - n\Omega_i}{\sqrt{2}|k_\|||v_{ti}}\right) - \right.$$ (4.19)

$$\left. \sum_n \Gamma_n(b_i)\frac{k_\perp V'_{di}}{|k_\|||\Omega_i}\left(1 + \frac{\omega - n\Omega_i}{\sqrt{2}|k_\|||v_{ti}}Z\left(\frac{\omega - n\Omega_i}{\sqrt{2}|k_\|||v_{ti}}\right)\right)\right]$$

The previous equation can be further simplified using the fact that $\sum_n \Gamma_n(b_i) = 1$. Hence, the ion susceptibility becomes

$$H_i = \frac{1}{k^2\lambda_{Di}^2}\left[1 - \frac{k_\perp V'_{di}}{|k_\|||\Omega_i} + \sum_n \Gamma_n(b_i)\left(\frac{\omega}{\sqrt{2}|k_\|||v_{ti}}Z\left(\frac{\omega - n\Omega_i}{\sqrt{2}|k_\|||v_{ti}}\right) - \right.\right.$$ (4.20)

$$\left.\left. \frac{k_\perp V'_{di}}{|k_\|||\Omega_i}\left(\frac{\omega - n\Omega_i}{\sqrt{2}|k_\|||v_{ti}}\right)Z\left(\frac{\omega - n\Omega_i}{\sqrt{2}|k_\|||v_{ti}}\right)\right)\right].$$

From Eq. (4.17), in the isotropic limit ($T_i = T_{\perp i} = T_{\|i}$), the electron susceptibility reads

$$H_e = \frac{1}{k^2\lambda_{Di}^2}\frac{T_i}{T_e}\left[1 + \left(\frac{\omega - k_\|V_{de}}{\sqrt{2}|k_\|||v_{te}}\right)Z\left(\frac{\omega - k_\|V_{de}}{\sqrt{2}|k_\|||v_{te}}\right)\right].$$ (4.21)

The dispersion relation is obtained by setting the dielectric function equal to zero: $\varepsilon = 1 + H_i + H_e = 0$. Before proceeding to compute ISR spectra, we first search for minima in the magnitude of the dielectric function $\varepsilon$ that could be associated with ISR spectra enhancements.

In the regime relevant to ISR spectra (in this case, the Bragg scale corresponds to $\lambda \approx 0.67\ m$), after having studied the morphology of the dielectric function $\varepsilon$, we found that no zeros could be obtained at least for the shear magnitudes considered here. This means that shears alone are not sufficient to destabilize the plasma. Nonetheless, the $\varepsilon$ function contains minima that are in some cases associated with realistic shear values. We first study the behavior of the dielectric function at several angles of the wave vector without the presence of a relative drift. In Fig. 4.5, we plotted the logarithm of the magnitude of the dielectric function $\varepsilon$ as a function of real frequency $\omega$ and shears $S_i = V'_{di}/\Omega_i$, at $\theta = 60°$ (upper panel), $\theta = 50°$ (middle panel) and $\theta = 40°$ (bottom panel), using Eqs. (4.20)-(4.21). Indeed, despite the fact that the minima are located in regions where the shears are large with $S_i \gtrsim 0.3$, the magnitude of $\varepsilon$ is lowered for a large range of shears

at $\omega/kC_s \sim 1.5$. This reduction in $|\varepsilon|$ should lead to an enhancement of the SDF at this frequency as compared with shearless situations. We also note that minima are moved to lower shears as the aspect angle $\theta$ decreases.

As the wave vector angle is further reduced, the minima are moved to regions for which the shears can be as small as $S_i \lesssim 0.3$. This is illustrated in Fig. 4.6 where the logarithm of $|\varepsilon|$ is plotted for $\theta = 30°$ (upper panel), $\theta = 20°$ (middle panel) and $\theta = 10°$ (bottom panel). At these aspect angles, we should expect greater enhancement of IA shoulders in presence of shears $S_i \lesssim 0.3$. This will be investigated in the following section.

In Fig. 4.7, we plotted the logarithm of $|\varepsilon|$ for very small aspect angles that correspond to directions that are almost perpendicular to the geomagnetic field: $\theta = 5°$ (upper panel), $3°$ (middle panel) and $2°$ (bottom panel), still using Eqs. (4.20)–(4.21). Interestingly, an important minima corresponding to zero frequency is now present in the region for which $S_i \lesssim 0.2$. Hence, we should expect an enhancement of the zero Doppler portion of the ISR spectrum when looking in directions close to perpendicular to $\mathbf{B}_0$. This might be related to the zero-frequency shear-driven waves near perpendicularity that were discussed in Chap. 3.

## 4.3.2   Computation of ISR spectra for stable plasmas under various ion velocity shears

From Eq. (4.14), the SDF in the isotropic limit ($T_i = T_{\perp i} = T_{\parallel i}$) becomes

$$S(\mathbf{k},\omega) = \frac{\sqrt{2\pi}}{k_{\parallel}v_{te}}\left|1 - \frac{H_e}{\varepsilon}\right|^2 e^{-\left(\frac{\omega - k_{\parallel}V_{de}}{\sqrt{2}k_{\parallel}v_{te}}\right)^2} + \frac{\sqrt{2\pi}}{k_{\parallel}v_{ti}}\left|\frac{H_e}{\varepsilon}\right|^2 \sum_m \Gamma(b_i)e^{-\left(\frac{\omega - m\Omega_i}{\sqrt{2}k_{\parallel}v_{ti}}\right)^2} \qquad (4.22)$$

where $b_i = k_{\perp}^2 v_{ti}^2/\Omega_i^2$ and where $H_i$ and $H_e$ are given by Eqs. (4.20)–(4.21). Figure 4.8 shows an example of computation of ISR spectra for various small shears at the low-frequency range that corresponds to the ion line (IA fluctuations). The spectra are still double-humped similarly to the shearless version. For the same set of bulk plasma parameters such as $T_e$, $T_i$ or $n_e$, the area under the curve is increased by a factor of 2.57 as $S_i$ is varied from 0 to 0.3, indicating stronger total scattered power. Since the dielectric function
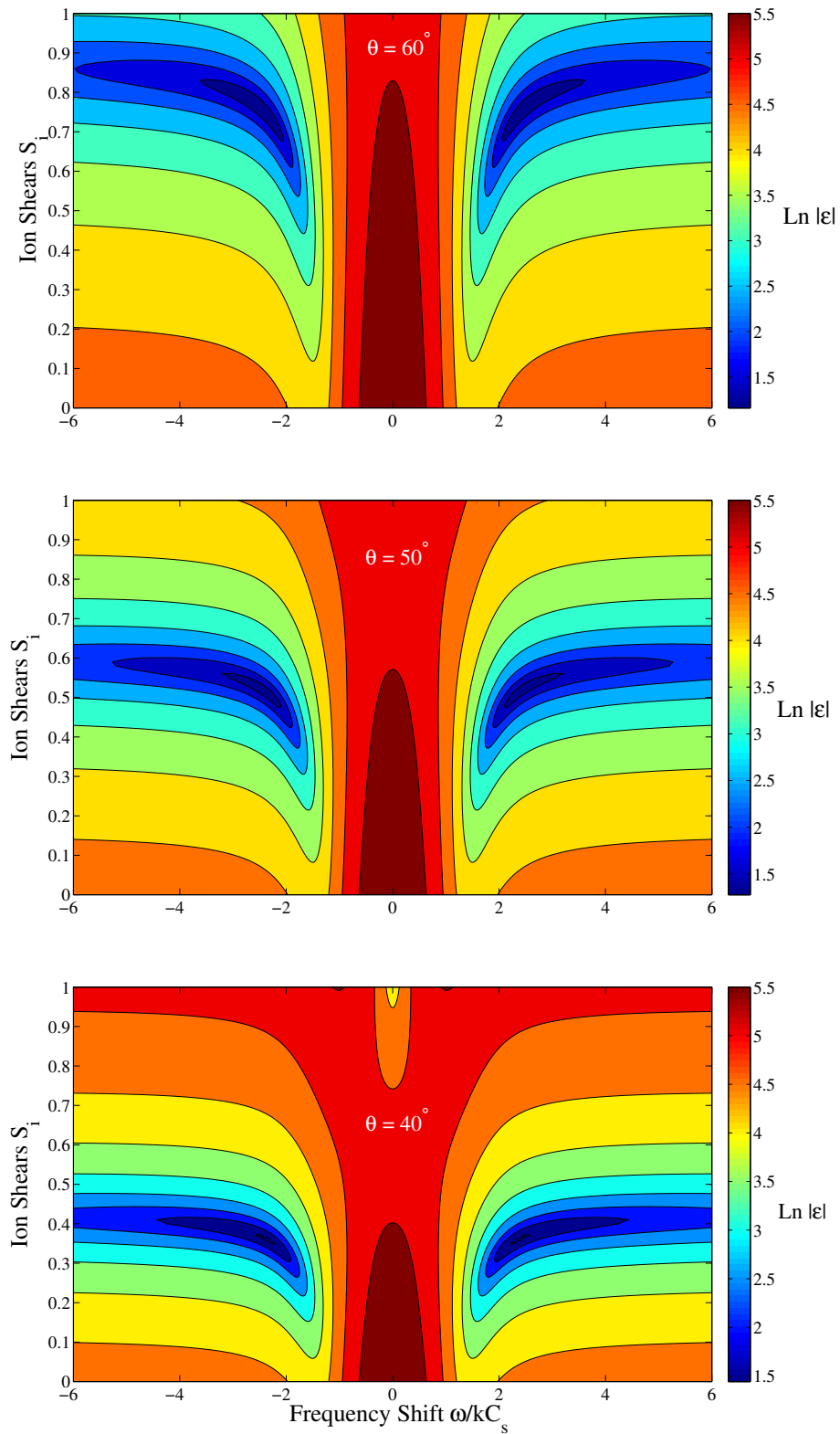
Figure 4.5: Search for minima in the the logarithm of the magnitude of the dielectric function $(\varepsilon = 1 + H_i + H_e)$ in presence of ion velocity shears $S_i = V'_{di}/\Omega_i$. Calculations were done for a Maxwellian plasma, in the case of EISCAT VHF 224MHz, at $\theta = 60°$ (upper panel), $\theta = 50°$ (middle panel) and $\theta = 40°$ (bottom panel), using Eqs. (4.20)–(4.21). Other parameters are as per Table 4.1.
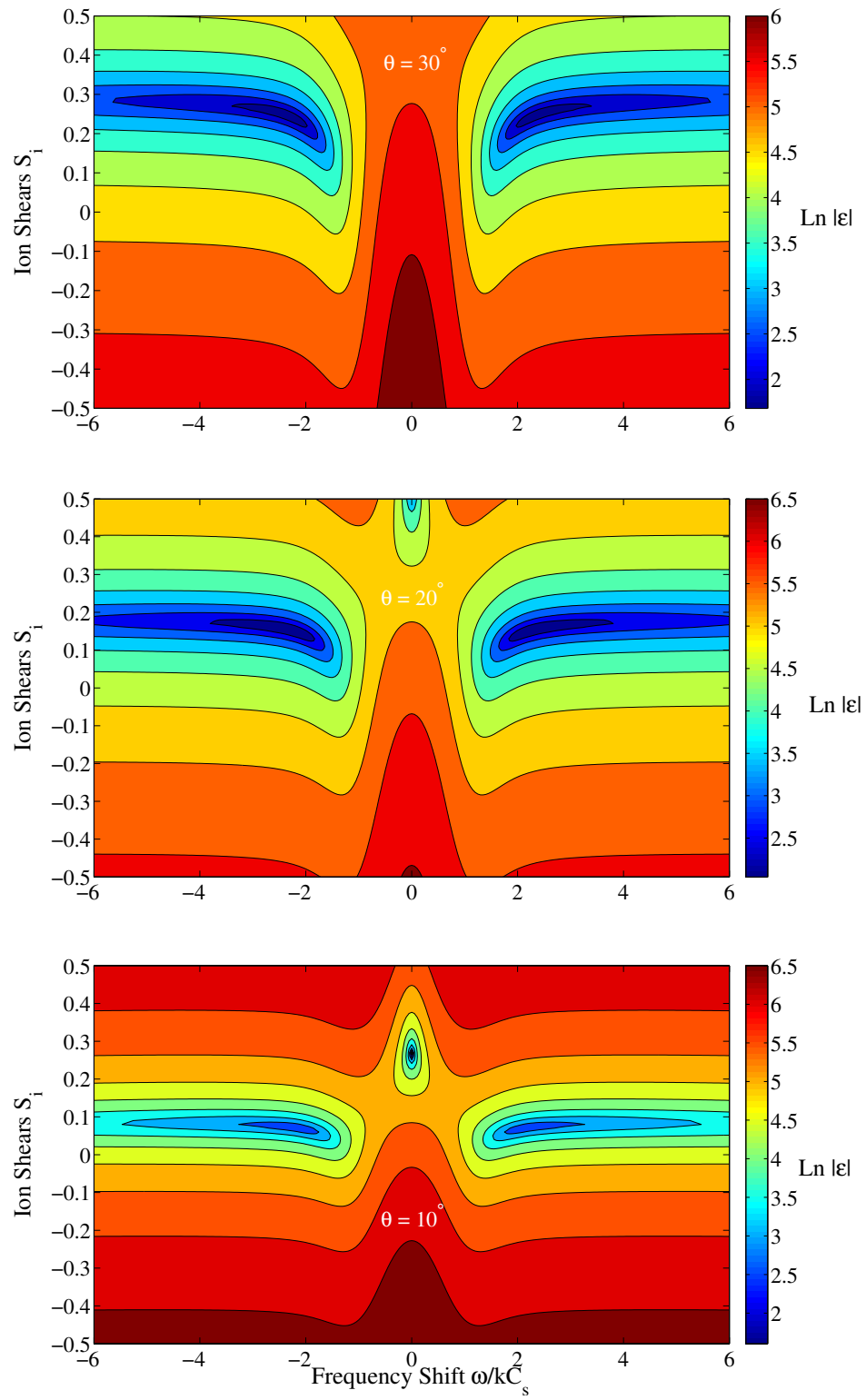
Figure 4.6: Same as Fig. 4.5, but for $\theta = 30°$ (upper panel), $20°$ (middle panel) and $10°$ (bottom panel).
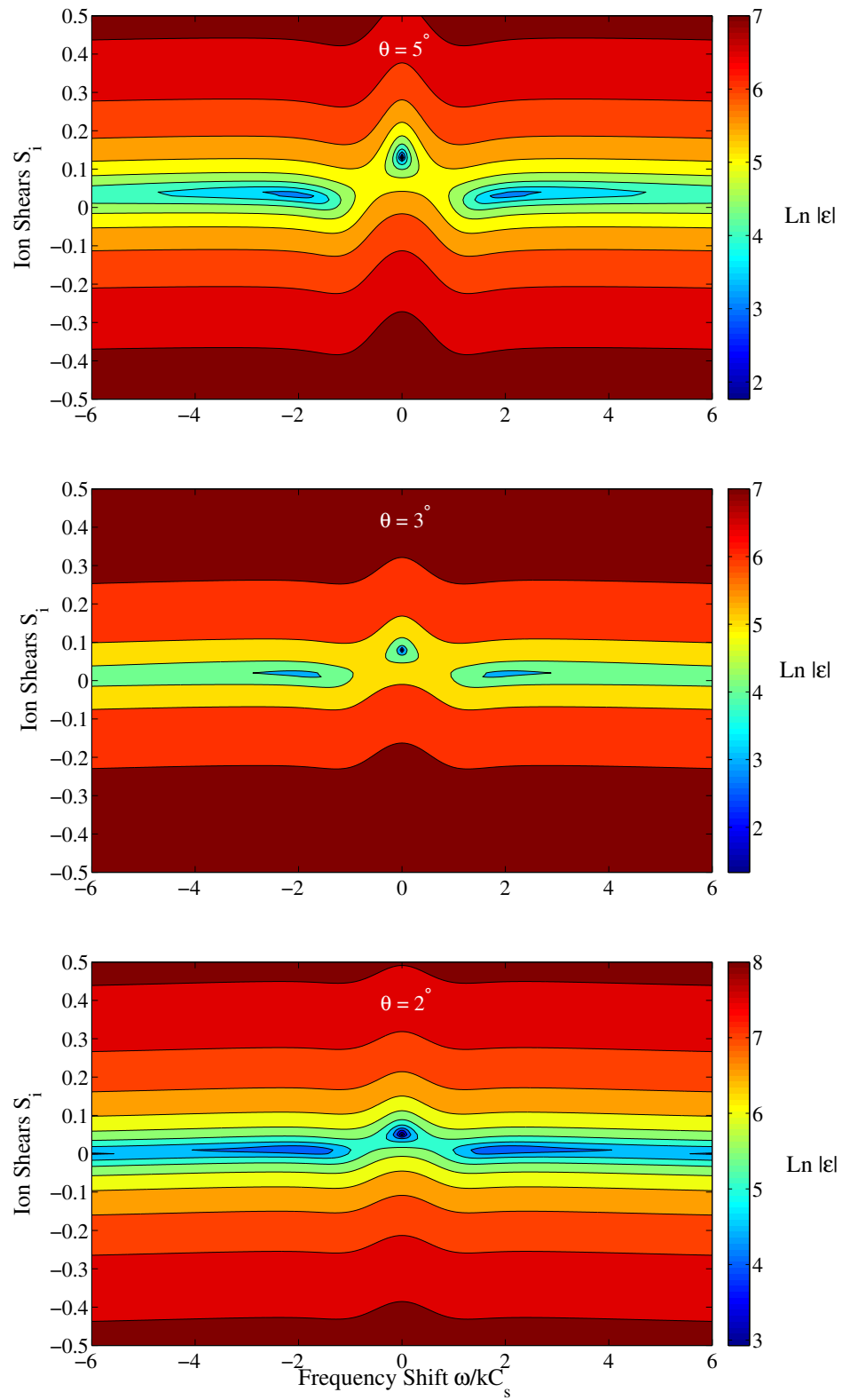
Figure 4.7: Same as Fig. 4.6, but for $\theta = 5°$ (upper panel), $3°$ (middle panel) and $2°$ (bottom panel).
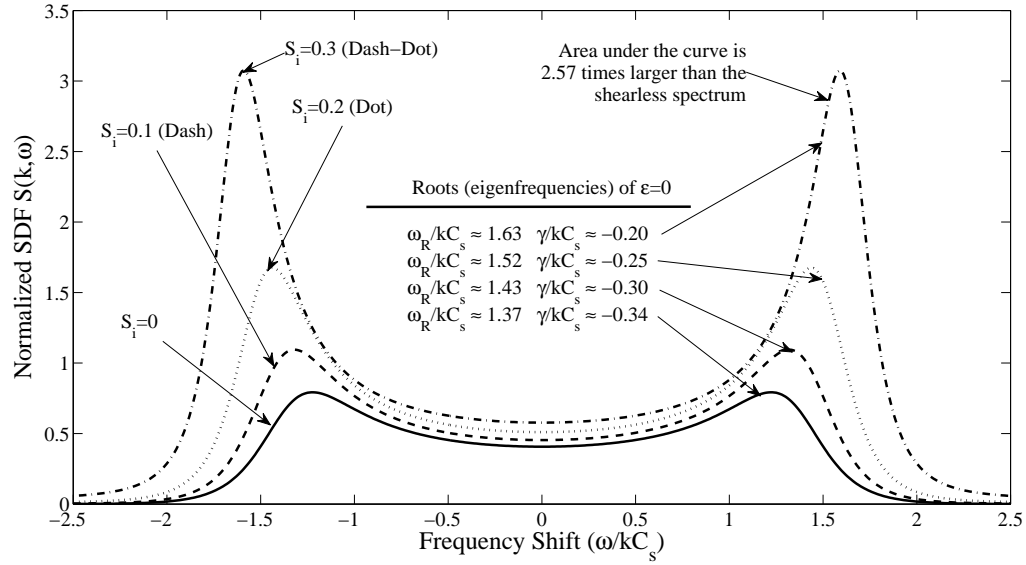
Figure 4.8: Effects of ion velocity shears on the theoretical EISCAT VHF 224MHz normalized SDF for a Maxwellian plasma at $\theta = 50°$. Eq. (4.4) is traced for $S_i = V'_{di}/\Omega_i$ from 0 (solid), 0.1 (dashed), 0.2 (dotted) and 0.3 (dash-dot). Other input parameters are as per Table 4.1.

$\varepsilon$ is in the denominator of the ion term [second term of Eq. (4.22)], an increase in the scattered power is expected when $|\varepsilon| \to 0$, that is, near the IA resonances of the plasma which, in this case, are modifed by shears. In addition, the spectral peaks are slighly upshifted and the peak-to-valley ratio is also augmented along with shears. The enhancement in the peak-to-valley ratio could lead to an overestimation of the electron-to-ion temperature ratio $T_e/T_i$ when fitting the spectrum with a shearless dielectric function (this will be further explored in Sect. 4.3.3). Similarly, the increase in spectral width could lead to an overestimation of the ion temperature to mass ratio $T_i/m_i$, or simply the ion temperature for equal ion masses.

To explain these ISR spectrum modifications due to shears, we have solved numerically the dispersion relation, $\varepsilon = 1 + H_i + H_e = 0$ along with Eqs. (4.20)–(4.21), in terms of real frequency $\omega_R/kC_s$ and damping rate $\gamma/kC_s$ (imaginary frequency). These roots are indicated on Fig. 4.8 and associated with each spectral peak using an arrow. Indeed, the real frequencies are upshifted as compared with the shearless spectrum and coincide well with spectral peaks. Moreover, the damping rates are weaker (smaller negative value) than the shearless case. This might explain the deepening of the valley between the two spectral

Figure 4.9: Effects of positive ion velocity shears on the theoretical EISCAT VHF 224MHz normalized SDF for a Maxwellian plasma at $\theta = 50°$. Equation (4.4) is traced as a contour plot for $0 \leq S_i = V'_{di}/\Omega_i \leq 0.4$. Other input parameters are as per Table 4.1.

peaks.

In Fig. 4.9, we show the effects of positive ion velocity shears on the normalized SDF at $\theta = 50°$ by tracing Eq. (4.4) as a contour plot for $0 \leq S_i = V'_{di}/\Omega_i \leq 0.4$. The spectral peaks enhancement with positive shears is clearly visible, in addition to the upshift in peak frequency. In contrast with these results, Fig. 4.10 shows how the SDF is modified by negative shears under the same conditions. In this case, we notice a flattening of the spectrum for larger negative shears. This result is consistent with the fact that $H_i$ (and $|\varepsilon|$) increases with negative shears as per Eq. (4.20).

In Fig. 4.11, we show how the SDF varies with the wave vector angle. In this example, we fixed the shears to $S_i = V'_{di}/\Omega_i = 0.1$ and we plotted Eq. (4.4) for $10° \leq \theta = \operatorname{atan}(|k_\parallel|/k_\perp) \leq 80°$. This contour plot shows that the effects of shears are increasingly important for directions close to perpendicular to $\mathbf{B}_0$. This can be understood from the fact that in Eq. (4.20), the normalized shear values $S_i = V'_{di}/\Omega_i$ are multiplied by the ratio

Figure 4.10: Effects of negative ion velocity shears on the theoretical EISCAT VHF 224MHz normalized SDF for a Maxwellian plasma at $\theta = 50°$. Equation (4.4) is traced as a contour plot for $0 \leq S_i = V'_{di}/\Omega_i \leq 0.4$. Other input parameters are as per Table 4.1.

$k_\perp/|k_\parallel|$. Hence, the contribution of shears on ion susceptibility becomes larger in directions closer to perpendicular to the magnetic field.

In Fig. 4.12, we present another example of computed ISR spectra at a smaller wave vector angle ($\theta = 30°$) in an attempt to find greater enhancements/modifications of the SDF. The normalized SDF (Eq. 4.22) is traced at $\theta = 30°$ and for $S_i = V'_{di}/\Omega_i$ from 0 (solid), 0.1 (dashed), 0.2 (dotted) and 0.25 (dash-dot). As shown in Fig. 4.6, we should expect significant spectral enhancements when $S_i \sim 0.25$ since this region is nearing a minima of the dielectric function $\varepsilon$. In this case, for the same set of parameters ($T_e$, $T_i$ or $n_e$), the area under the curve is increased by a factor of 15.18 as $S_i$ is varied from 0 to 0.25. This example shows that a velocity shear of $S_i \sim 0.2$ is sufficient to enhance both spectral peaks by an order of magnitude. In addition, the spectral peaks are upshifted significantly and the peak-to-valley ratio is also increased by a significant amount. The upshifts in real frequency are in good agreement with the roots of the dispersion relation obtained numerically and indicated in Fig. 4.12. Also, the deepening of the valley between the spectral
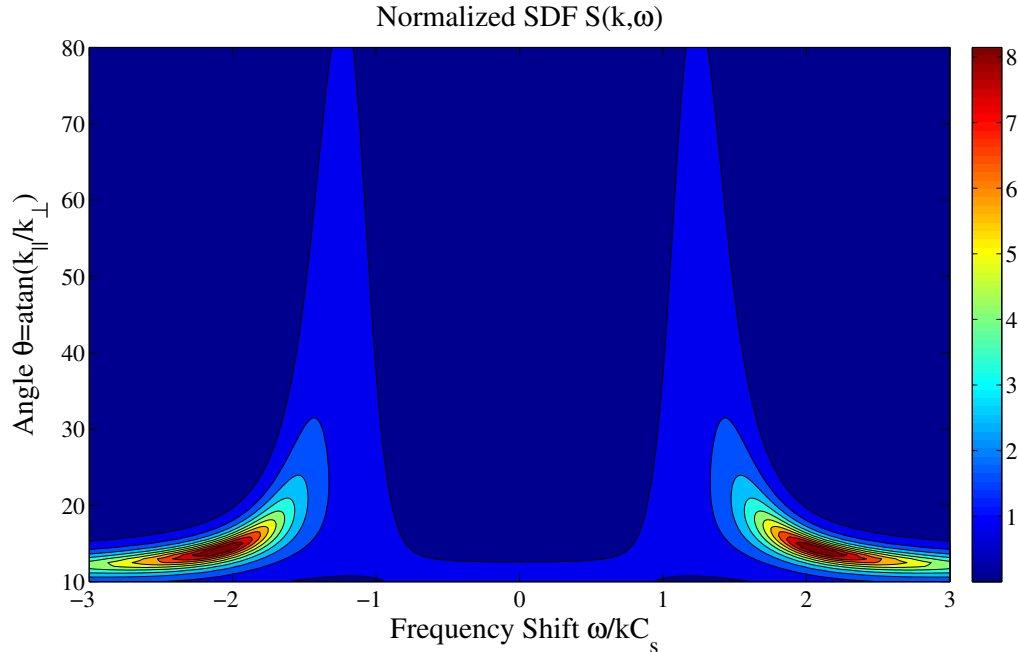
Figure 4.11: Theoretical EISCAT VHF 224MHz normalized SDF in a Maxwellian plasma for which $S_i = V'_{di}/\Omega_i = 0.1$. Equation (4.4) is traced as a contour plot for $10° \leq \theta = \mathrm{atan}(|k_\parallel|/k_\perp) \leq 80°$. Other input parameters are as per Table 4.1.

peaks is consistent with the damping rates, except at $S_i = 0.25$. In this case, we notice that the damping rate is increasing (larger negative value), suggesting that the plasma is becoming more stable. A close look at the upper panel of Fig. 4.6 shows that at $S_i = 0.25$, some portions of the spectrum correspond to a region slightly past the minimum in $|\varepsilon|$ (this can be seen by tracing a horizontal line at $S_i = 0.25$).

In summary, the previous figures suggest that under proper conditions, small perpendicular shears in parallel ion drift velocities, associated with "large" gradient scales, could be a meachanism leading to double peaks enhancement in ISR spectra, or NEIALs. Nevertheless, such spectra would be difficult to observe since they would be very sensitive to the aspect angle, in other words, the radar probing direction would need to be at an oblique angle of approximately $30 - 40°$ with respect to the direction perpendicular to $\mathbf{B}_0$ in order to detect an order of magnitude enhancement in spectral power. Despite the fact that NEIALs have been observed at oblique angles (for example, with Milestone Hill radar), more often than not, they are detected when the radar is looking almost parallel to the geomagnetic
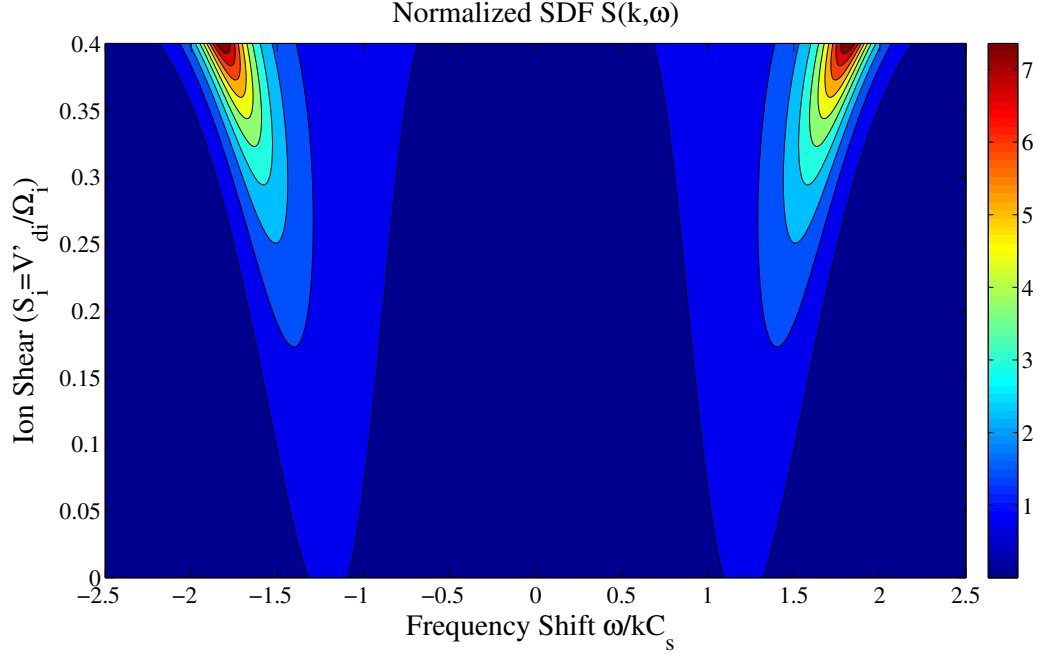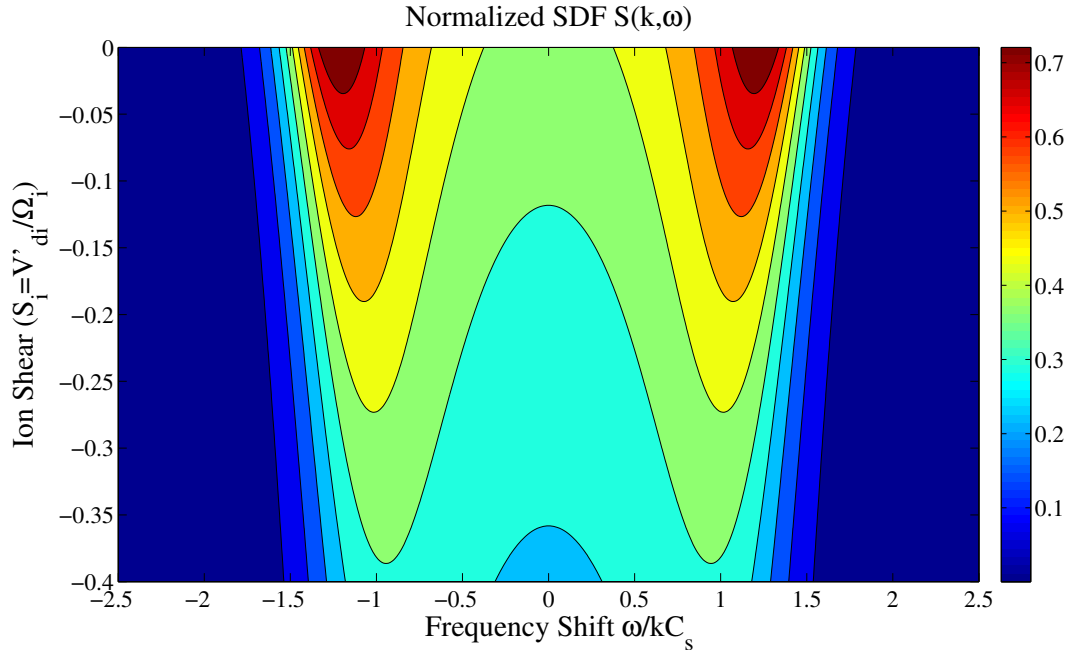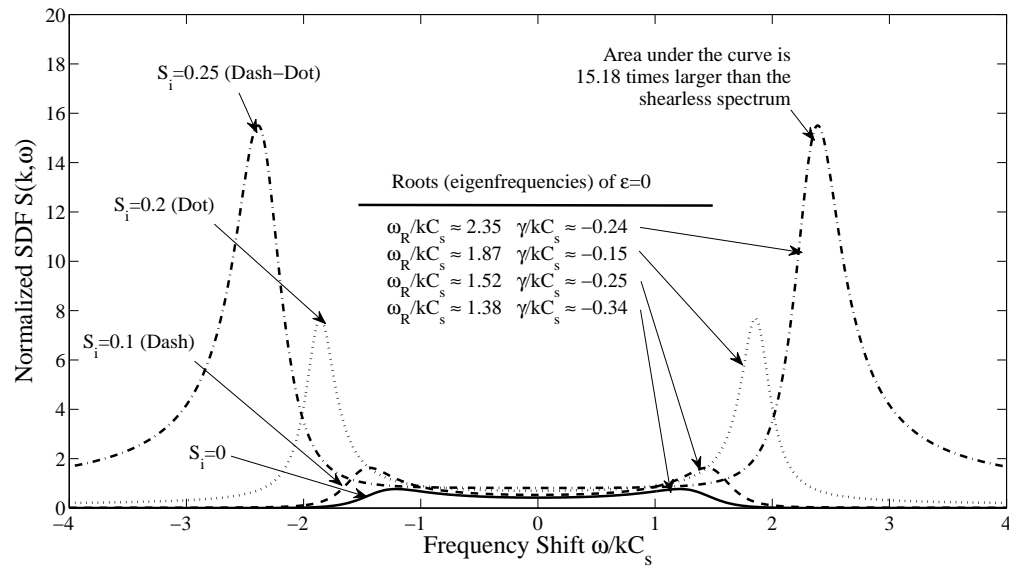
Figure 4.12: Effects of ion velocity shears on the theoretical EISCAT VHF 224MHz normalized SDF for a Maxwellian plasma at $\theta = 30°$. Equation (4.4) is traced for $S_i = V'_{di}/\Omega_i$ from 0 (solid), 0.1 (dashed), 0.2 (dotted) and 0.25 (dash-dot). Other input parameters are as per Table 4.1.

field. Furthermore, in accordance with the local approximation, the radar probing direction needs to be perpendicular to the velocity gradient direction (since $k_x = 0$). In addition to this severe constraint in observational geometry, these calculations would be valid in cases for which the velocity gradient scale length is larger than the scale length associated with the scattering volume. Also, as stated previously, these calculations are based on linear theory and consequently, are valid for a stable plasma. It is likely that NEIAL phenomena observed with ISRs involve non-linear physics as well. In spite of all these constraints, this is a first important step toward understanding how small velocity gradients could influence the ISR spectral properties before the onset of microturbulences.

### 4.3.3 Possible errors in interpreted plasma parameters when fitting with standard Maxwellian dielectric functions

Having computed a few examples of ISR spectra in presence of shears, we are facing the following question: if we apply the standard Maxwellian interpretation for retrieving the
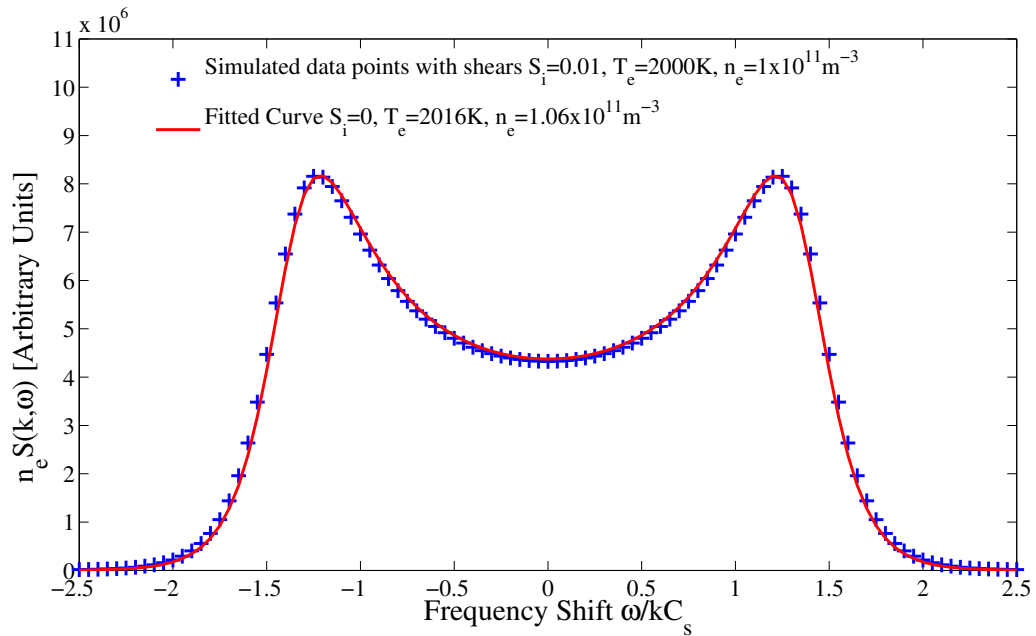
Figure 4.13: Example of fitting an ISR spectrum $[n_e S(k, \omega)]$ modified by a small shear ($S_i = 0.01$) with a standard Maxwellian dielectric function at $\theta = 30°$. The blue $+$ represent simulated data points in presence of shears ($T_e = 2000K, n_e = 1 \times 10^{11} m^{-3}$). The red curve is the fitted spectrum with $T_e = 2016K, n_e = 1.06x10^{11} m^{-3}$ Other input parameters are as per Table 4.1.

plasma parameters from incoherent scatter radars, what sorts of errors would one encounter by assuming that the ion susceptibilities are not effected by shears? To simplify this preliminary analysis, the parameters that were solved for in the process of obtaining a least square fit are the electron number density, $n_e$, and the electron temperature, $T_e$. Since we have kept the ion temperature constant, this is equivalent to varying the electron to ion temperature ratio, $T_e/T_i$. The ion composition $m_i$, which is assumed to be known, was also kept constant. We have used the Matlab nonlinear curve-fitting solver in the least-squares sense (lsqcurvefit), as part of the optimization toolbox. The tolerance on the objective function (TolFun) and the lower bound on the step size (TolX) were set to $1 \times 10^{-12}$. To ensure convergence of the solver, we have run a few simulations for very small values of shear ($S_i = 0.01, 0.02$ and $0.07$).

Figure 4.13 is an example of fitting a standard ISR spectrum based on Maxwellian dielectric functions to $n_e S(k, \omega)$ in presence of a very small shear $S_i = 0.01$. In this case,
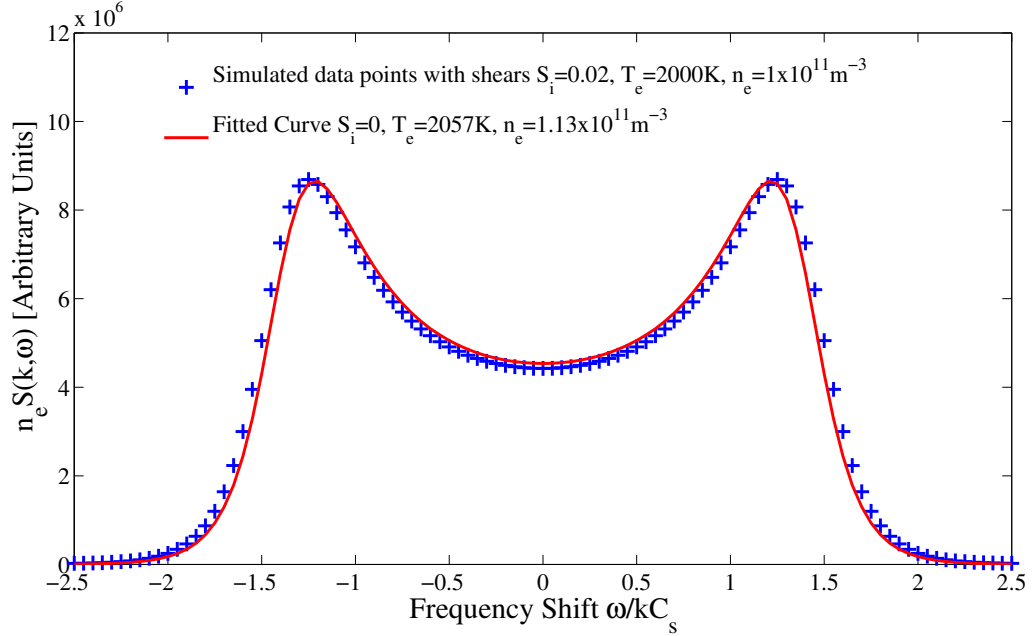
Figure 4.14: Example of fitting an ISR spectrum $[n_e S(k, \omega)]$ modified by a small shear ($S_i = 0.02$) with a standard Maxwellian dielectric function at $\theta = 30°$. The blue $+$ represent simulated data points in presence of shears ($T_e = 2000K, n_e = 1 \times 10^{11} m^{-3}$). The red curve is the fitted spectrum with $T_e = 2057K, n_e = 1.13x10^{11} m^{-3}$ Other input parameters are as per Table 4.1.

the electron temperature is overestimated to $2016K$ (compared to $2000K$) and the electron number density is overestimated to $1.06 \times 10^{11} m^{-3}$ instead of $1.00 \times 10^{11} m^{-3}$. Although the fitted spectrum leads to small differences in interpreted parameters, this calculation for small shears indicate that both $n_e$ and $T_e/T_i$ would be overestimated. In Fig. 4.14, we present another example for $S_i = 0.02$. In this case, the electron temperature would be overestimated by $\sim 3\%$ and the number density by $13\%$. This case shows that significant overestimation in $n_e$ can be obtained even in presence of very small shears. Assuming that $\Omega_i = 300s^{-1}$, this corresponds to $V'_{di} = 6s^{-1}$.

We performed another simulation for $S_i = 0.07$ (results not plotted). We obtained overestimations $8\%$ in $T_e$ and $52\%$ in $n_e$. Our preliminary results suggest that under realistic shears, the plasma density derived with standard Maxwellian interpretation is the parameter that could be most severely overestimated (more than $\sim 50\%$). In future work, we will allow the ion temperature to vary during the least square fitting process in order to obtain a

more accurate estimation of possible errors.

## 4.4   Summary and conclusions

We have studied separately the contribution of ion temperature anisotropy and velocity shears in modifying or enhancing the EISCAT VHF ISR spectrum density. For smaller wavelengths that are relevant to ISR observations, we had to keep the cyclotron terms in the summation of Bessel functions for a magnetized plasma. Under this regime, we confirmed that these terms blend in to produce spectra that are similar to the unmagnetized case.

After having derived the spectral density function, $S(\mathbf{k}, \omega)$, for bi-Maxwellian plasmas while taking into account ion gyroresonances (in a magnetized plasma), we found that both IA peaks are enhanced when the perpendicular ion temperature increases with respect to the parallel one, at least when the angle is far from orthogonality. However, we also showed that ion temperature anisotropy is in fact unimportant when the radar is pointing at the critical angle for which the total ion temperature is equal to the effective temperature. We concluded that the enhancement in IA shoulders is due to the expected reduced ion Landau damping associated with a lower parallel ion temperature with respect to the electron temperature. In addition, when the radar is looking in directions near perpendicular to the geomagnetic field, we found that the presence of ion temperature anisotropy with $T_{\perp i} > T_{\parallel i}$ leads to an enhancement in the Bernstein modes modulating the spectrum. In the end, we did not find any significant contribution from ion temperature anisotropies in enhancing the ion component of ISR spectra in a magnetized plasma. To our knowledge, such study had never been undertaken before. This work confirms that ion gyroresonance effects can be safely neglected even for a bi-Maxwellian plasma, at least when the radar probing direction is far from orthogonal to $\mathbf{B}_0$.

Then, we considered the effects of ion velocity shears on the shape of ISR spectra. To this end, we first discussed the regime in parameter space that would allow using the dielectric function for sheared and Maxwellian plasmas in the calculation of ISR spectra.

Afterwards, we searched for minima in the morphology of the dielectric function, $\varepsilon$, that could be associated with ISR spectral enhancements. This allowed to investigate the conditions that would allow the greatest enhancements in the ion line portion of ISR spectra. We found that, in the limit for which the spatial scale length associated with the hydrodynamic drift velocity gradient is larger than the Bragg wavelength, small ion velocity shears can, in somes cases, lead to double peaks enhancement in spectral power by an order of magnitude. This effect is more important when the radar probing direction is closer to perpendicular than parallel to $\mathbf{B}_0$. However, such enhancements would be difficult to observe. For one thing, they would be very sensitive to the aspect angle. Also, to be consistent with the assumptions stemming from the local approximation, the radar probing direction would need to be perpendicular to the velocity gradient direction. Finally, such calculations would be valid in cases for which the velocity gradient scale length is larger than the scale length associated with the scattering volume. Nevertheless, this study provides new insights on the extent for which ISR spectra can be affected by small parallel velocity shears before the onset of microinstabilities.

Chapter 5

# Summary, Conclusions and Future Work

## 5.1 Summary and Conclusions

In general, the aim of this thesis was to further our understanding of possible direct genera-
tion mechanisms behind small-scales irregularities in the high-latitude F-region, which can
be observed with incoherent or coherent scatter radars. In particular, we considered the con-
tribution of parallel current densities, ion velocity shears and ion temperature anisotropies
in the triggering of plasma instabilities and the subsequent occurence of irregularities since
these processes are known to exist at high latitudes.

Space weather affects the properties of the terrestrial ionosphere. The effects of space
weather are even more important at high-latitudes since the ionosphere is strongly coupled
with the magnetosphere and the solar wind. In particular, the high-latitude F-region can
be host to phenomena such as energetic particles precipitating along the magnetic field
lines, intense field-aligned currents, perpendicular electric field and E×B drifts, ion up-
flows/outflows and field-aligned structures.

The presence of field-aligned currents carried by thermal particles, ion velocity shears
and temperature anisotropies can be sources of plasma instabilities in the high-latitude
ionosphere and in turn, it can lead to small-scale irregularities. Therefore, we were faced
with the following question: in terms of observations, what magnitudes of parallel current
densities, ion velocity shears and temperature anisotropies could the ionosphere support?
From the literature review, we showed that very intense and localized field-aligned current
densities in excess of $1000 \ \mu A/m^2$ exist sometimes at high latitudes, despite the presence
of much lower large-scale average parallel current densities. With ion outflows also being
an important part of high-latitude processes, perpendicular shears in parallel ion velocities
on the order of $1 - 20 \ ms^{-1}m^{-1}$(Hz) seem to be sustainable. In addition, ion temperature

anisotropies with $T_{\perp i}/T_{\parallel i}$ on the order of 2-5 can be expected at times in the high-latitude F-region.

The detection of naturally enhanced ion-acoustic lines near the edges of auroral structures, often linked with ion upflows and parallel current densities, suggests that shear-modified CDEIA instabilities could take place in these regions. Also, the increase of IA waves growth rate with temperature anisotropy, as reported in laboratory experiments, suggests that anisotropic plasmas could be unstable to smaller critical drifts.

Based on these observations, the following scientific questions provided an important motivation for this thesis: Can ion temperature anisotropies and velocity shears lower the threshold requirements for current-driven electrostatic ion-acoustic (CDEIA) instabilities in the high-latitude F-region? Also, what magnitudes of current densities (or relative drifts), shears, and temperature anisotropies does the theory predict for the onset of instabilities? Similarly, could this additional physics lead to enhanced incoherent scattering from ion-acoustic waves in the high-latitude F-region, which could possibly be detected with incoherent scatter radars?

After having generalized the electrostatic kinetic dispersion relation of St-Maurice *et al.* (2007) to a bi-Maxwellian plasma and studied the instability threshold conditions, we arrived at the following main conclusions:

- At altitudes high enough so that collisions with neutrals can be neglected, we found that ion temperature anisotropy lowers the threshold conditions for a large range of intermediate wave vector angles. This lowering of instability threshold conditions is likely caused by the reduced ion Landau damping that would be expected in a plasma with a lower parallel ion temperature with respect to the electron temperature.

- In the collisional F-region, the critical relative drifts are increased by approximately one order of magnitude due to the dampening effect of collisions. However, small drift and shear threshold conditions can be obtained in spite of collisions. In this

case, the instability is restricted to very narrow angular intervals, close to the direction perpendicular to the geomagnetic field. We found that realistic ion temperature anisotropies reduce these instability threshold drift minima to smaller shear requirements, for modes propagating almost perpendicularly to the geomagnetic field. For directions close to perpendicular to the geomagnetic field, it appears that the increase in $T_{\perp i}$ plays a role more important than reducing the ratio $T_{\parallel i}/T_e$ in setting the conditions for instability.

- In terms of possible observations of coherent echoes, our study showed that $V'_{di} < 30 \ ms^{-1}m^{-1}$ could be required at threshold, assuming that $\Omega_i \sim 300 \ s^{-1}$, for wave frequencies $\omega/kC_s \lesssim 0.3$ and with ion anisotropies of the order $A_i \sim 2$. These modes have an ideal geometry to be observed with SuperDARN radars that are pointing almost perpendicularly to the geomagnetic field. Nonetheless, these modes would be very sensitive to the aspect angle, since they are restricted to very narrow angular intervals. In those situations, the Doppler shifts in the E×B moving frame would be on the order of $\sim 45 \ s^{-1}$, for $\lambda = 10 \ m$ and assuming $C_s \sim 1500 \ ms^{-1}$. This instability mechanism could account, in some cases, for discrepancies between the line-of-sight drifts and the line-of-sight component of the E×B drift of the order of several hundreds $ms^{-1}$.

Another objective was to study the effects of ion velocity shears and temperature anisotropies on the ISR spectrum density function $S(k, \omega)$ to determine whether this additional physics could enhance the IA spectrum. After having derived the ISR spectral density function for stable, magnetized, collisionless and bi-Maxwellian plasmas, we computed ISR spectra under various ion temperature anisotropies and velocity shears. Our study led to the following conclusions:

- In a plasma for which ion gyroresonances effects are not neglected, we showed that ion temperature anisotropy is in fact unimportant when the incoherent radar is pointing at the critical angle for which the total ion temperature is equal to the effective temperature. The enhancement in ion-acoustic shoulders when the radar is looking in directions close to parallel to the magnetic field is likely due to the reduced ion

Landau damping associated with a lower parallel ion temperature with respect to the electron temperature. When the radar is looking in directions near perpendicular to the magnetic field, the presence of ion temperature anisotropy leads to enhancement in the Bernstein modes modulating the spectrum. We confirmed that ion gyroresonance effects can be safely neglected even for a bi-Maxwellian plasma, at least when the radar probing direction is far from orthogonal to the geomagnetic field.

- In the limit for which the spatial scale length associated with velocity shears is larger than the Bragg wavelength, small ion velocity shears can, in somes cases, lead to double peaks enhancement in spectral power by an order of magnitude. This effect is more important when the radar probing direction is closer to perpendicular than parallel to the magnetic field. This fact notwithstanding, such enhancements would be sensitive to the radar probing direction, Also, in a manner consistent with the local approximation used to derive $S(k, \omega)$, the radar probing direction would need to be perpendicular to the velocity gradient direction. Nevertheless, this study provides new insights on the extent for which ISR spectra can be affected by small parallel velocity shears before the onset of microinstabilities.

In the end, the ion temperature anisotropy is an important parameter that needs to be considered in the studies of sheared and collisional low-frequency CDEIA waves and instabilities in the high-latitude F-region, especially at small aspect angles. Such instabilities could play a role in the direct generation of field-aligned irregularities in the collisional F-region that could be observed with coherent radars. On the other hand, our study suggests that temperature anisotropies do not play a significant role in enhancing spectra that would be expected from incoherent scatter radars. This mechanism did not provide any additional contribution to the possible generation of coherent echoes, or NEIALs. Yet, even "small" ion velocity shears seem to be capable under the right conditions of producing significant enhancements in ISR spectra, especially for directions closer to perpendicular to the geomagnetic field. Although not a mechanism of choice to explain observations of NEIALs, it could lead to an overestimation of the interpreted electron to ion temperature ratio $T_e/T_i$ and the electron density $n_e$ when using standard ISR fitting procedures.

## 5.2   Future Work

The following are suggestions for additional work related to plasma instability threshold conditions:

- The kinetic model could be generalized to include density gradients in the local approximation. Such density gradients would be representative of actual geophysical density gradients occuring near the edges of auroral arcs.

- Compare threshold conditions predicted from linear theory with outputs obtained from the recent electrodynamical model of de Boer *et al.* (2010). This model computes systematically the temperatures (including their anisotropies), densities, collision frequencies, electric fields, vertical electron and ion drifts, as well as ion velocity shears.

- Seek for unusual Doppler shifts, Doppler widths or aspect angles in SuperDARN data, especially near the edges of regions with sharp convection changes. After having separated ground and E-region echoes, study the geophysical conditions behind the occurence of these unusual F-region echoes. The presence of very narrow spectra (less than 50 $ms^{-1}$ for instance) that are not E$\times$B drifting might be due to the local mechanisms discussed in this thesis.

The following are suggestions for additional work related to incoherent scatter radar spectra:

- To include collisions in the calculation of the spectrum density function $S(k,\omega)$.

- To study how the spectrum density function vary with wavenumbers, which would be representative of different incoherent scatter radars. Also, when fitting ISR spectra using the standard Maxwellian interpretation, allow a third parameter (in this case $T_i$) to vary in order to obtain a more accurate estimation of possible errors.

- Perform a Monte Carlo simulation including ion velocity shears and compare ISR spectra with those predicted from linear theory.

- Attempt to obtain ISR observations in presence of sheared ion upflows (for small shears). The radar pointing direction would need to be perpendicular to the velocity gradient direction.

# Bibliography

Amatucci, W. E. (1999). Inhomogeneous plasma flows: A review of in situ observations and laboratory experiments. *Journal of Geophysical Research: Space Physics*, **104**(A7), 14481–14503.

Bahcivan, H. and Cosgrove, R. (2008). Enhanced ion acoustic lines due to strong ion cyclotron wave fields. *Ann. Geophys.*, **26**, 2081–2095.

Bahcivan, H., Nicolls, M. J., and Perry, G. (2013). Comparison of superDARN irregularity drift measurements and F-region ion velocities from the resolute bay ISR. *J. Atmos. Sol.-Terr. Phys.*, **105–106**(0), 325 – 331.

Basu, B. and Coppi, B. (1988). Fluctuations associated with sheared velocity regions near auroral arcs. *Geophys. Res. Lett.*, **15**(5), 417–420.

Basu, B. and Coppi, B. (1989). Velocity shear and fluctuations in the auroral regions of the ionosphere. *J. Geophys. Res.*, **94**(A5), 5316–5326.

Basu, S., Basu, S., MacKenzie, E., Coley, W., Hanson, W., and Lin, C. (1984). F-region electron density irregularity spectra near auroral acceleration and shear regions. *J. Geophys. Res.*, **89**(A7), 5554–5564.

Basu, S., Basu, S., Senior, C., Weimer, D., Nielsen, E., and Fougere, P. (1986). Velocity shears and sub-km scale irregularities in the nighttime auroral F-region. *Geophys. Res. Lett.*, **13**(2), 101–104.

Basu, S., Basu, S., MacKenzie, E., Fougere, P., Coley, W., Maynard, N., Winningham, J., Sugiura, M., Hanson, W., and Hoegy, W. (1988). Simultaneous density and electric field fluctuation spectra associated with velocity shears in the auroral oval. *J. Geophys. Res.*, **93**(A1), 115–136.

Baumjohann, W. and Treumann, R. (1997). *Basic space plasma physics*. Imperial College Press.

Beynon, W. and Williams, P. (1978). Incoherent scatter of radio waves from the ionosphere. *Reports on Progress in Physics*, **41**(6), 909–955.

Bhatnagar, P. L., Gross, E. P., and Krook, M. (1954). A model for collision processes in gases. i. small amplitude processes in charged and neutral one-component systems. *Phys. Rev.*, **94**, 511–525.

Blixt, E., Grydeland, T., Ivchenko, N., Hagfors, T., La Hoz, C., Lanchester, B., Løvhaug, U., and Trondsen, T. (2005). Dynamic rayed aurora and enhanced ion-acoustic radar echoes. *Ann. Geophys.*, **23**, 3–11.

Borovsky, J., Suszcynsky, D., Buchwald, M., and DeHaven, H. (1991). Measuring the thicknesses of auroral curtains. *Arctic*, pages 231–238.

Brekke, A. (2012). *Physics of the upper polar atmosphere*. Springer.

Buchert, S., van Eyken, A., Ogawa, T., and Watanabe, S. (1999). Naturally enhanced ion-acoustic lines seen with the EISCAT svalbard radar. *Adv. Space Res.*, **23**, 1699–1704.

Buneman, O. (1959). Dissipation of currents in ionized media. *Phys. Rev.*, **115**, 503–517.

Chibisov, D., Mikhailenko, V., and Stepanov, K. (2011). The ion kinetic d'Angelo mode. *Phys. Plasmas*, **18**, 102105–102110.

Collis, P., Häggström, L., Kaila, K., and Rietveld, M. (1991). EISCAT radar observations of enhanced incoherent scatter spectra; their relation to red aurora and field-aligned currents. *Geophys. Res. Lett.*, **18**(6), 1031–1034.

Daldorff, L. K., Pécseli, H., and Trulsen, J. (2007). Nonlinearly generated plasma waves as a model for enhanced ion acoustic lines in the ionosphere. *Geophys. Res. Lett.*, **34**(18), 18101.

D'Angelo, N. (1965). Kelvin—helmholtz instability in a fully ionized plasma in a magnetic field. *Phys. Fluids*, **8**, 1748–1750.

de Boer, J., Noël, J.-M., and St-Maurice, J.-P. (2010). The effects of mesoscale regions of precipitation on the ionospheric dynamics, electrodynamics and electron density in the presence of strong ambient electric fields. *Ann. Geophys.*, **28**(6), 1345–1360.

de La Beaujardiere, O., Heelis, R., *et al.* (1984). Velocity spike at the poleward edge of the auroral zone. *J. Geophys. Res.*, **89**(A3), 1627–1634.

Diaz, M., Semeter, J., Oppenheim, M., and Zettergren, M. (2010). Analysis of beam plasma instability effects on incoherent scatter spectra. *Ann. Geophys.*, **28**, 2169–2175.

Diaz, M., Oppenheim, M., Semeter, J., and Zettergren, M. (2011). Particle-in-cell simulation of incoherent scatter radar spectral distortions related to beam-plasma interactions in the auroral ionosphere. *J. Geophys. Res.*, **116**(A1).

Dougherty, J. and Farley, D. (1960). A theory of incoherent scattering of radio waves by a plasma. *Proc. R. Soc. A.*, **259**(1296), 79–99.

Earle, G., Kelley, M., and Ganguli, G. (1989). Large velocity shears and associated electrostatic waves and turbulence in the auroral F-region. *J. Geophys. Res.*, **94**(A11), 15321–15333.

Evans, J. (1969). Theory and practice of ionosphere study by Thomson scatter radar. *Proc. IEEE*, **57**(4), 496–530.

Farley, D. T., Dougherty, J. P., and Barron, D. W. (1961). A theory of incoherent scattering of radio waves by a plasma ii. Scattering in a magnetic field. *Proc. R. Soc. A.*, **263**(1313), 238–258.

Fejer, B. G. and Kelley, M. C. (1980). Ionospheric irregularities. *Rev. Geophys.*, **18**(2), 401–454.

Fejer, J. (1961). Scattering of radio waves by an ionized gas in thermal equilibrium in the presence of a uniform magnetic field. *Can. J. Phys.*, **39**(5), 716–740.

Fejer, J. A. (1960). Radio-wave scattering by an ionized gas in thermal equilibrium. *J. Geophys. Res.*, **65**(9), 2635–2636.

Forme, F. (1993). A new interpretation on the origin of enhanced ion acoustic fluctuations in the upper ionosphere. *Geophys. Res. Lett.*, **20**(21), 2347–2350.

Forme, F. (1999). Parametric decay of beam-driven langmuir wave and enhanced ion-acoustic fluctuations in the ionosphere: a weak turbulence approach. *Ann. Geophys.*, **17**, 1172–1181.

Forme, F. R. E., Fontaine, D., and Wahlund, J. E. (1995). Two different types of enhanced ion acoustic fluctuations observed in the upper ionosphere. *J. Geophys. Res.*, **100**(A8), 14625–14636.

Foster, J., Del Pozo, C., Groves, K., and St-Maurice, J.-P. (1988). Radar observations of the onset of current driven instabilities in the topside ionosphere. *Geophys. Res. Lett.*, **15**(2), 160–163.

Foster, J. C. (1990). Plasma turbulence and enhanced UHF radar backscatter form the topside ionosphere. *Physics of Space Plasma (1988), SPI Conf. Proc., Scientific Pub., Cambridge*, **8**, 213–229.

Fried, B. and Conte, S. (1961). *The plasma dispersion function: the Hilbert transform of the Gaussian*. New York: Academic Press.

Fried, B. and Gould, R. (1961). Longitudinal ion oscillations in a hot plasma. *Phys. Fluids*, **4**, 139–147.

Froula, D., Sheffield, J., Glenzer, S., and Neville C. Luhmann, J. (2010). *Plasma Scattering of Electromagnetic Radiation: Theory and Measurement Techniques*. Academic Press/Elsevier.

Gaimard, P., St-Maurice, J.-P., Lathuillere, C., and Hubert, D. (1998). On the improvement of analytical calculations of collisional auroral ion velocity distributions using recent Monte Carlo results. *J. Geophys. Res.*, **103**, 4079–4095.

Ganguli, G., Lee, Y., and Palmadesso, P. (1988). Kinetic theory for electrostatic waves due to transverse velocity shears. *Phys. Fluids*, **31**, 823–838.

Gary, S. P. and Schwartz, S. J. (1980). An electrostatic flow shear instability. *J. Geophys. Res.: Space Physics (1978–2012)*, **85**(A6), 2978–2980.

Gavrishchaka, V., Ganguli, S., and Ganguli, G. (1998). Origin of low-frequency oscillations in the ionosphere. *Phys. Rev. Lett.*, **80**(4), 728–731.

Gavrishchaka, V., Ganguli, S., and Ganguli, G. (1999). Electrostatic oscillations due to filamentary structures in the magnetic-field-aligned flow: The ion-acoustic branch. *J. Geophys. Res.*, **104**(A6), 12683–12694.

Gavrishchaka, V., Ganguli, G., Scales, W., Slinker, S., Chaston, C., McFadden, J., Ergun, R., and Carlson, C. (2000). Multiscale coherent structures and broadband waves due to parallel inhomogeneous flows. *Phys. Rev. Lett.*, **85**(20), 4285–4288.

Glatthor, N. and Hernandez, R. (1990). Temperature anisotropy of drifting ions in the auroral F-region, observed by EISCAT. *J. Atmos. Terr. Phys.*, **52**(6), 545–560.

Greenwald, R., Baker, K., Dudeney, J., Pinnock, M., Jones, T., Thomas, E., Villain, J.-P., Cerisier, J.-C., Senior, C., Hanuise, C., *et al.* (1995). Darn/superdarn. *Space Sci. Rev.*, **71**(1-4), 761–796.

Grydeland, T., La Hoz, C., Hagfors, T., Blixt, E., Saito, S., Strømme, A., and Brekke, A. (2003). Interferometric observations of filamentary structures associated with plasma instability in the auroral ionosphere. *Geophys. Res. Lett.*, **30**(6), 1338.

Grydeland, T., Blixt, E., Løvhaug, U., Hagfors, T., La Hoz, C., and Trondsen, T. (2004). Interferometric radar observations of filamented structures due to plasma instabilities and their relation to dynamic auroral rays. *Ann. Geophys.*, **22**, 1115–1132.

Guio, P. and Forme, F. (2006). Zakharov simulations of Langmuir turbulence: Effects on the ion-acoustic waves in incoherent scattering. *Phys. Plasmas*, **13**, 122902.

Hall, L. S., Heckrotte, W., and Kammash, T. (1965). Ion cyclotron electrostatic instabilities. *Phys. Rev.*, **139**, A1117–A1137.

Harris, E. (1959). Unstable plasma oscillations in a magnetic field. *Phys. Rev. Lett.*, **2**(2), 34–36.

Harris, E. (1961). Plasma instabilities associated with anisotropic velocity distributions. *J. Nucl. Energy, Part C*, **2**, 138–145.

Hunsucker, R. and Hargreaves, J. (2002). *The High-Latitude Ionosphere and its Effects on Radio Propagation*. Cambridge University Press.

Kagan, L. and St-Maurice, J. (2005). Origin of type-2 thermal-ion upflows in the auroral ionosphere. *Ann. Geophys.*, **23**, 13–24.

Kelley, M. (2009). *The Earth's Ionosphere: Plasma Physics and Electrodynamics*. International Geophysics Series. Academic Press.

Kelley, M. and Carlson, C. (1977). Observations of intense velocity shear and associated electrostatic waves near an auroral arc. *J. Geophys. Res.*, **82**(16), 2343–2348.

Kindel, J. and Kennel, C. (1971). Topside current instabilities. *J. Geophys. Res.*, **76**(13), 3055–3078.

Kintner, P. (1976). Observations of velocity shear driven plasma turbulence. *J. Geophys. Res.*, **81**(28), 5114–5122.

Kivanc, O. and Heelis, R. (1999). On relationships between horizontal velocity structure and thermal ion upwellings at high latitudes. *Geophys. Res. Lett.*, **26**(13), 1829–1832.

Knudsen, D. J., Haerendel, G., Buchert, S., Kelley, M., Steen, Å., and Brändström, U. (1993). Incoherent scatter radar spectrum distortions from intense auroral turbulence. *J. Geophys. Res.: Space Physics (1978–2012)*, **98**(A6), 9459–9471.

Koepke, M. (2004). Sheared-flow-driven electrostatic waves in laboratory and space plasmas. *Phys. Scr.*, **2004**, 182–187.

Koepke, M., Teodorescu, C., and Reynolds, E. (2003). Space relevant laboratory studies of ion-acoustic and ion-cyclotron waves driven by parallel-velocity shear. *Plasma Phys. Control. Fusion*, **45**, 869–889.

Koepke, M., Reynolds, E., *et al.* (2007). Simultaneous, co-located parallel-flow shear and perpendicular-flow shear in low-temperature, ionospheric-plasma relevant laboratory plasma. *Plasma Phys. Control. Fusion*, **49**(5A), A145.

Kontar, E. and Pécseli, H. (2005). Nonlinear wave interactions as a model for naturally enhanced ion acoustic lines in the ionosphere. *Geophys. Res. Lett.*, **32**(5), 5110.

Krall, N. and Trivelpiece, A. (1973). *Principles of plasma physics*. McGraw-Hill.

Liu, H. and Lu, G. (2004). Velocity shear-related ion upflow in the low-altitude ionosphere. *Ann. Geophys.*, **22**(4), 1149–1153.

Lockwood, M. and Winser, K. (1988). On the determination of ion temperature in the auroral F-region ionosphere. *Planet. Space Sci.*, **36**(11), 1295–1304.

Loranc, M. and St-Maurice, J.-P. (1994). A time-dependent gyro-kinetic model of thermal ion upflows in the high-latitude F-region. *J. Geophys. Res.*, **99**(A9), 17429–17451.

Loranc, M., Hanson, W., Heelis, R., and St-Maurice, J.-P. (1991). A morphological study of vertical ionospheric flows in the high-latitude F-region. *J. Geophys. Res.*, **96**(A3), 3627–3646.

Løvhaug, U. and Flå, T. (1986). Ion temperature anisotropy in the auroral F-region as measured with EISCAT. *J. Atmos. Terr. Phys.*, **48**(9), 959–971.

Lu, G., Reiff, P., Moore, T., and Heelis, R. (1992). Upflowing ionospheric ions in the auroral region. *J. Geophys. Res.*, **97**(A11), 16855–16863.

Lunde, J., Gustavsson, B., Løvhaug, U., Lorentzen, D., and Ogawa, Y. (2007). Particle precipitations during NEIAL events: simultaneous ground based observations at Svalbard. *Ann. Geophys.*, **25**, 1323–1336.

Maggs, J. and Davis, T. (1968). Measurements of the thicknesses of auroral structures. *Planet. Space Sci.*, **16**(2), 205–209.

McCune, J. E. (1965). General criterion for electrostatic plasma instabilities with uniform magnetic field. *Phys. Rev. Lett.*, **15**(16), 684–685.

Michell, R. and Samara, M. (2010). High-resolution observations of naturally enhanced ion acoustic lines and accompanying auroral fine structures. *J. Geophys. Res.*, **115**(A3), A03310.

Michell, R. and Samara, M. (2013). Observability of NEIALs with the sondrestrom and poker flat incoherent scatter radars. *J. Atmos. Terr. Phys.*

Michell, R., Lynch, K., Heinselman, C., and Stenbaek-Nielsen, H. (2008). PFISR nightside observations of naturally enhanced ion acoustic lines, and their relation to boundary auroral features. *Ann. Geophys.*, **26**, 3623–3639.

Michell, R., Lynch, K., Heinselman, C., and Stenbaek-Nielsen, H. (2009). High time resolution PFISR and optical observations of naturally enhanced ion acoustic lines. *Ann. Geophys.*, **27**, 1457–1467.

Mikhailenko, V., Chibisov, D., and Mikhailenko, V. (2006). Shear-flow-driven ion cyclotron instabilities of magnetic field-aligned flow of inhomogeneous plasma. *Phys. Plasmas*, **13**, 102105.

Mikhailenko, V., Mikhailenko, V., and Stepanov, K. (2008). Ion cyclotron instabilities of parallel shear flow of collisional plasma. *Phys. Plasmas*, **15**, 092901.

Mikhailenko, V., Chibisov, D., and Koepke, M. E. (2012). Excitation mechanisms and spectral properties of the ion-cyclotron parallel-velocity shear driven instability. *J. Geophys. Res.*, **117**(A4), 4322.

Neubert, T. and Christiansen, F. (2003). Small-scale, field-aligned currents at the top-side ionosphere. *Geophys. Res. Lett.*, **30**(19).

Noël, J., St-Maurice, J., and Blelly, P. (2000). Nonlinear model of short-scale electrodynamics in the auroral ionosphere. *Ann. Geophys.*, **18**, 1128–1144.

Noël, J., St-Maurice, J., and Blelly, P. (2005). The effect of E-region wave heating on electrodynamical structures. *Ann. Geophys.*, **23**(6), 2081–2094.

Ogawa, Y., Fujii, R., Buchert, S., Nozawa, S., Watanabe, S., and Van Eyken, A. (2000). Simultaneous EISCAT svalbard and VHF radar observations of ion upflows at different aspect angles. *Geophys. Res. Lett.*, **27**(1), 81–84.

Ogawa, Y., Buchert, S., Fujii, R., Nozawa, S., and Forme, F. (2006). Naturally enhanced ion-acoustic lines at high altitudes. *Ann. Geophys.*, **24**, 3351–3364.

Ossakow, S. and Chaturvedi, P. (1979). Current convective instability in the diffuse aurora. *Geophys. Res. Lett.*, **6**(4), 332–334.

Perraut, S., Brekke, A., Baron, M., and Hubert, D. (1984). EISCAT measurements of ion temperatures which indicate non-isotropic ion velocity distributions. *J. Atmos. Terr. Phys.*, **46**(6), 531–543.

Perron, P., Noël, J., and St-Maurice, J. (2009). Velocity shear and current driven instability in a collisional F-region. *Ann. Geophys.*, **27**, 381–394.

Perron, P., Noël, J., Kabin, K., and St-Maurice, J. (2013). Ion temperature anisotropy effects on threshold conditions of a shear-modified current driven electrostatic ion-acoustic instability in the topside auroral ionosphere. *Ann. Geophys.*, **31**(3), 451–457.

Ponomarenko, P. V., St-Maurice, J.-P., Waters, C. L., Gillies, R. G., and Koustov, A. V. (2009). Refractive index effects on the scatter volume location and doppler velocity estimates of ionospheric hf backscatter echoes. *Ann. Geophys.*, **27**(11), 4207–4219.

Raman, R. V. (1980). *Incoherent scattering of radar waves in the auroral ionosphere*. Ph.D. thesis, University of Michigan.

Raman, R. V., St-Maurice, J.-P., and Ong, R. (1981). Incoherent scattering of radar waves in the auroral ionosphere. *J. Geophys. Res.*, **86**(A6), 4751–4762.

Rietveld, M., Collis, P., and St-Maurice, J.-P. (1991). Naturally enhanced ion acoustic waves in the auroral ionosphere observed with the EISCAT 933-Mhz radar. *J. Geophys. Res.*, **96**(A11), 19291–19305.

Rother, M., S.-K. and Lühr, H. (2007). CHAMP observation of intense kilometer-scale field-aligned currents, evidence for an ionospheric Alfvén resonator. *Ann. Geophys.*, **25**(7), 1603–1615.

Ruohoniemi, J., Greenwald, R., Baker, K., Villain, J., and McCready, M. (1987). Drift motions of small-scale irregularities in the high-latitude F region: An experimental comparison with plasma drift motions. *JGR: Space Physics (1978–2012)*, **92**(A5), 4553–4564.

Salpeter, E. E. (1960). Scattering of radio waves by electrons above the ionosphere. *J. Geophys. Res.*, **65**(6), 1851–1852.

Sandahl, I., Sergienko, T., and Brändström, U. (2008). Fine structure of optical aurora. *J. Atmos. Terr. Phys.*, **70**(18), 2275–2292.

Schunk, R. and Nagy, A. (2004). *Ionospheres: Physics, Plasma Physics, and Chemistry*. Cambridge atmospheric and space sciences series. Cambridge University Press.

Scime, E., Keesee, A., Spangler, R., Koepke, M., Teodorescu, C., and Reynolds, E. (2002). Evidence for thermal anisotropy effects on shear modified ion acoustic instabilities. *Phys. Plasmas*, **9**, 4399–4401.

Sedgemore-Schulthess, F. and St-Maurice, J. (2001). Naturally enhanced ion-acoustic spectra and their interpretation. *Surv. Geophys.*, **22**(1), 55–92.

Sedgemore-Schulthess, K., Lockwood, M., Trondsen, T., Lanchester, B., Rees, M., Lorentzen, D., and Moen, J. (1999). Coherent EISCAT Svalbard Radar spectra from the dayside cusp/cleft and their implications for transient field-aligned currents. *J. Geophys. Res.*, **104**, 24613–24624.

Shume, E. B. (2000). *Simulation of Gyro Lines for the EISCAT Svalbard Radar*. Master's thesis, Univ. of Tromsø, Tromsø, Norway.

Skolnik, M. I. (2003). *Introduction to Radar Systems*. Tata McGraw Hill.

Spangler, R., Scime, E., and Ganguli, G. (2002). Parallel inhomogeneous flows in a thermally anisotropic plasma: The electrostatic ion-acoustic branch. *Phys. Plasmas*, **9**, 2526–2533.

St-Maurice, J., Hanson, W., and Walker, J. (1976). Retarding potential analyzer measurement of the effect of ion-neutral collisions on the ion velocity distribution in the auroral ionosphere. *J. Geophys. Res.*, **81**, 5438–5446.

St-Maurice, J., Prikryl, P., Danskin, D., Hamza, A., Sofko, G., Koehler, J., Kustov, A., and Chen, J. (1994). On the origin of narrow non-ion-acoustic coherent radar spectra in the high-latitude E-region. *J. Geophys. Res.*, **99**(A4), 6447–6474.

St-Maurice, J., Noël, J.-M., and Perron, P. (2007). An assessment of how a combination of shears, field-aligned currents and collisions affect f-region ionospheric instabilities. *J. Plasma Physics*, **73**(1), 69–88.

St-Maurice, J.-P. (2003). 2003 EISCAT radar school: Non thermal scattering mechanisms. Lecture notes presented at the EISCAT radar school in Menlo Park, California, `www.eiscat.com/groups/Documentation/CourseMaterials/2003MenloPark`.

St-Maurice, J.-P. and Hamza, A. (2009). Small scale irregularities at high latitudes, Characterising the ionopshere, Ed. G. Wyman; Technical Report RTO-TR-IST-051. `http://www.rto.nato.int/abstracts.aspx`.

St-Maurice, J.-P. and Schunk, R. (1979). Ion velocity distributions in the high-latitude ionosphere. *Rev. Geophys. and Space Phys.*, **17**(1), 99–133.

St-Maurice, J.-P. and Schunk, R. W. (1977). Auroral ion velocity distributions for a polarization collision model. *Planet. Space Sci.*, **25**(3), 243–260.

St-Maurice, J.-P., K. W. and James, D. (1996). In situ generation of intense parallel electric fields in the lower ionosphere. *J. Geophys. Res.*, **101**(A1), 335–356.

Stix, T. (1992). *Waves in plasmas*. American Institute of Physics.

Sullivan, J., Lockwood, M., Lanchester, B., Kontar, E., Ivchenko, N., Dahlgren, H., and Whiter, D. (2008). An optical study of multiple neial events driven by low energy electron precipitation. *Ann. Geophys.*, **26**, 2435–2447.

Suvanto, K., Lockwood, M., and Fuller-Rowell, T. (1989). The influence of anisotropic F-region ion velocity distributions on ionospheric ion outflows into the magnetosphere. *J. Geophys. Res.*, **94**(A2), 1347–1358.

Swartz, W. E., Providakes, J. F., Kelley, M. C., and Vickrey, J. F. (1988). The effect of strong velocity shears on incoherent scatter spectra: A new interpretation of unusual high latitude spectra. *Geophys. Res. Lett.*, **15**(12), 1341–1344.

Teodorescu, C., Koepke, M., and Reynolds, E. (2003). On the role of ion temperature anisotropy in the growth and propagation of shear-modified ion-acoustic waves. *J. Geophys. Res.*, **108**, 1043–1053.

Treumann, R. and Baumjohann, W. (1997). *Advanced Space Plasma Physics*. Imperial College Press.

Trondsen, T. and Cogger, L. (1997). High-resolution television observations of black aurora. *J. Geophys. Res.*, **102**(A1), 363–378.

Trondsen, T. and Cogger, L. (2001). Fine-scale optical observations of aurora. *Phys. Chem. Earth, Pt. C*, **26**(1), 179–188.

Tsunoda, R., Livingston, R., Vickrey, J., Heelis, R., Hanson, W., Rich, F., and Bythrow, P. (1989). Dayside observations of thermal-ion upwellings at 800-km altitude: an ionospheric signature of the cleft ion fountain. *J. Geophys. Res.*, **94**(A11), 15277–15290.

Tsunoda, R. T. (1988). High-latitude F region irregularities: A review and synthesis. *Reviews of Geophys.*, **26**(4), 719–760.

Wahlund, J.-E., Opgenoorth, H., Häggström, I., Winser, K., and Jones, G. (1992a). EISCAT observations of topside ionospheric ion outflows during auroral activity: Revisited. *J. Geophys. Res.*, **97**(A3), 3019–3037.

Wahlund, J.-E., Forme, F., Opgenoorth, H., Persson, M., Mishin, E., and Volokitin, A. (1992b). Scattering of electromagnetic waves from a plasma: Enhanced ion acoustic fluctuations due to ion-ion two-stream instabilities. *Geophys. Res. Lett.*, **19**, 1919–1922.

Walker, D., Amatucci, W., Antoniades, J., Ganguli, G., Bowles, J., Duncan, D., Gavrishchaka, V., and Koepke, M. (1997). Perpendicular ion heating by velocity-shear-driven plasma waves. *Geophys. Res. Lett.*, **24**, 1187–1190.

Watson, G. (1944). *A treatise on the theory of Bessel functions*. Cambridge University Press.

Whalen, B., Green, D., and McDiarmid, I. (1974). Observations of ionospheric ion flow and related convective electric fields in and near an auroral arc. *J. Geophys. Res.*, **79**(19), 2835–2842.

Winkler, E., St-Maurice, J.-P., and Barakat, A. (1992). Results from improved monte carlo calculations of auroral ion velocity distributions. *J. Geophys. Res.: Space Physics (1978–2012)*, **97**(A6), 8399–8423.

Winser, K., Lockwood, M., and Jones, G. (1987). Non-thermal plasma observations using EISCAT: Aspect angle dependence. *Geophys. Res. Lett.*, **14**(9), 957–960.

Xu, L., Koustov, A. V., Thayer, J., and McCready, M. A. (2001). Superdarn convection and Sondrestrom plasma drift. *Ann. Geophys.*, **19**(7), 749–759.

Yau, A. and André, M. (1997). Sources of ion outflow in the high latitude ionosphere. *Space Sci. Rev.*, **80**, 1–25.

# Appendix A

# More on the Procedure to Derive the Fluid Dispersion Relation

The fluid-like dispersion relation (Eq. 3.14) was not derived using fluid theory, but rather by simplifying the kinetic dispersion relation (Eqs. 3.2 and 3.10–3.13). This allows to retain some Landau growth/damping effects and to calculate the instability threshold conditions. For ion-acoustic waves, this is done by taking the long-wavelength limit ($k\lambda_{De} \to 0$) since ion Landau damping increases as the wavelength approaches the Debye length. In addition, to further minimize ion Landau damping kinetic effects, the phase velocity has to be much larger than the background ion thermal velocity $|\omega/k| \gg v_{ti}$ and smaller than the electron thermal velocity $|\omega/k - V_{de}| \ll v_{te}$ in order to fall within the positive slope of the electron distribution (thus allowing energy transfer from thermal particles to the wave).

Following standard procedure, we apply the small electron and large ion argument Taylor expansion to the plasma dispersion function Z. In this study, since the relevant temperature in the argument the plasma dispersion function Z is the parallel temperature, $T_{\|i}$, this procedure is equivalent to the condition $T_{\|i} \ll T_e$. In this case, the plasma dispersion function can then be approximated with $Z(z_i) \approx -1/z_i - 1/2z_i^3$ for the ions and $Z(z_e) \approx i\sqrt{\pi} - 2z_e$ for the electrons, where $z_{i,e}$ is the argument of the $Z$ function for the ions/electrons. There is no wave-particle interaction term in the form of $i\sqrt{\pi}\sigma z e^{-z^2}$ in the ion plasma dispersion function since the imaginary part is positive (Fried and Conte, 1961). In order to recover the fluid limit, we considered cases for which $b_i \ll 1$, so that only the $n = 0$ mode survives the sum over the modified Bessel functions. The modified Bessel function can then be further approximated by the relation $I_0(b_i) \approx 1 - b_i$. Finally, the function $U_e$ has been neglected, since $\sqrt{\frac{T_e}{m_e}} >> \sqrt{\frac{T_i}{m_i}}$, as a result of the small electron inertia ($m_e << m_i$).

# Appendix B

# Numerical Analysis of the Kinetic Dispersion Relation

In this appendix, we provide additional information on the numerical analysis procedure that was undertaken to find the instability threshold conditions. The electrostatic dispersion relation corresponds to the zeros of the dielectric function. The plasma dielectric $\varepsilon$ is a complex function that depends on complex frequency: $\varepsilon(k, \omega_R, \gamma) = \varepsilon_R(k, \omega_R, \gamma) + i\varepsilon_i(k, \omega_R, \gamma)$. It can be expanded with respect to the real frequency at vanishing growth rate such that

$$\varepsilon \sim \varepsilon_R(\omega_R) + i\varepsilon_i(\omega_R) + i\gamma \frac{\partial \varepsilon_R}{\partial \omega}|_{\gamma=0}. \tag{B.1}$$

When calculating the threshold conditions, which correspond to zero growth ($\gamma = 0$), the real and imaginary parts of the dielectric function must be equal to 0 ($\varepsilon_R = \varepsilon_i = 0$).

## B.1 Dimensionless Quantities

For all numerical calculations, the wave frequency $\omega_R/kC_s$, gyrofrequency $\Omega_i/kC_s$, collision frequencies ($\nu_i/\Omega_i$ and $\nu_e/\nu_i$), perpendicular ion over electron temperature ratio $\tau$ and the ion temperature anisotropy ratio $A_i$ were held fixed and provided as input parameters. Also, we used $O^+$ as the major ion constituent with $m_i/m_e = 29166$. The associated threshold shears and drifts were calculated for different values of $\theta$ by searching for the numerical roots of the aforementioned system of equations. The two unknowns in normalized form are the ion velocity shear $\zeta_i = k_\perp V'_{di}/|k_\parallel|\Omega_i = S_i/\tan\theta$ and the vertical electron drift (with respect to the ion frame) $V_{de}/C_s$. These normalisation parameters differ from those of Spangler *et al.* (2002) since we were interested in comparing our results with St-Maurice *et al.* (2007)'s results. When finding roots of the kinetic dispersion relation, the critical drift numerical solutions were normalized with the total ion-acoustic speed, using the total ion temperature expression $T_i = (T_{\parallel i} + 2T_{\perp i})/3$. Hence, the isothermal ion-acoustic speed can

be formulated as a function of parallel and perpendicular thermal velocities

$$
\begin{aligned}
C_s &= v_{\|ti}\sqrt{A_i\left(\frac{1}{\tau}+\frac{1}{3}\left(\frac{1}{A_i}+2\right)\right)} \\[2mm]
&= v_{te}\sqrt{\frac{m_e}{m_i}}\sqrt{1+\frac{\tau}{3}\left(\frac{1}{A_i}+2\right)} \\[2mm]
&= v_{\perp ti}\sqrt{\frac{1}{\tau}+\frac{1}{3}\left(\frac{1}{A_i}+2\right)}
\end{aligned}
\tag{B.2}
$$

from which the following dimensionless quantities were expressed as

$$
b_i = \frac{k_\perp^2 k_B T_{\perp i}}{\Omega_i^2 m_i} = \cos^2\theta\left(\frac{kC_s}{\Omega_i}\right)^2\left[\frac{1}{\left[\frac{1}{\tau}+\frac{1}{3}\left(\frac{1}{A_i}+2\right)\right]}\right]
$$

$$
\frac{\omega}{\sqrt{2}|k_\||v_{\|ti}} = \left(\frac{\omega}{kC_s}\right)\left(\frac{1}{\sqrt{2}\sin\theta}\right)\sqrt{A_i\left[\frac{1}{\tau}+\frac{1}{3}\left(\frac{1}{A_i}+2\right)\right]}
$$

$$
\frac{\omega}{\sqrt{2}|k_\||v_{\|te}} = \left(\frac{\omega}{kC_s}\right)\left(\frac{1}{\sqrt{2}\sin\theta}\right)\sqrt{\frac{m_e}{m_i}}\sqrt{1+\frac{\tau}{3}\left(\frac{1}{A_i}+2\right)}
$$

$$
\frac{V_{de}}{\sqrt{2}v_{te}} = \frac{V_{de}}{C_s}\left(\frac{1}{\sqrt{2}}\right)\sqrt{\frac{m_e}{m_i}}\sqrt{1+\frac{\tau}{3}\left(\frac{1}{A_i}+2\right)}.
$$

## B.2 Computer Analysis

The Matlab "fsolve" subroutine, as part of Matlab Optimisation Toolbox, was used to find the zeros of the system of nonlinear equations. An initial guess needs to be provided to the optimisation algorithm. Several additional optimization options (e.g.: maximum number of function evaluations, number of iterations, etc.) can be provided when the solver failed to converge to a solution. In addition, the tolerance parameters were set to a higher precision than default values. In most cases, the tolerance on the objective function (TolFun) and the lower bound on the step size (TolX) were set to $1 \times 10^{-15}$.

The subroutine "Faddeeva" (FFT-based) was used to compute the exponentially scaled complex complementary error function $W(z) = \exp(-z^2)\text{erfc}(-iz)$ where $\text{erfc}(x)$ is the complex complementary error function ($W(z)$ is also named Fadeeva function, especially

in the Russian litterature). The plasma dispersion function $Z$ can then be expressed as

$$Z(z) = i\sqrt{\pi}[\text{erfc}(z)]. \tag{B.3}$$

The accuracy of the function was improved by increasing the optional parameter $N$ (second argument), which defines the number of expansion terms, from $N = 12$ (default value) to 500. The accuracy of the Faddeeva subroutine, which includes the analytical continuation in the lower imaginary plane, was confirmed by comparing with the original calculation tables of Fried and Conte (1961).

The $n^{th}$ order modified Bessel functions of the first kind $I_n(b)$ were computed using the Matlab "besseli" subroutine. In the calculation of derivatives of Bessel functions $I'_n(b)$, the following recursion relation was used

$$I'_n(b) = I_{n+1}(b) + \frac{n}{b}I_n(b). \tag{B.4}$$

## B.3  Morphological study of the function to determine the initial guess

The reason behind the morphological study was to examine how the dielectric function behaves at a given angle of the wave vector. Numerical solutions were validated by visualising the morphology of the dielectric function. Furthermore, it allowed to locate the minima of the function in order to provide better initial guess to the optimisation algorithm. The natural logarithm of the modulus of the dielectric function was plotted (surface plot) as a function of ion shears and relative drifts. Figures 4.5 to 4.7 provide examples of morphological study of the function $\varepsilon$ although, in this case, $\ln|\varepsilon|$ is plotted as a function of shears and frequency.

# Curriculum Vitae

## Personal

- Place of birth: Québec, Qc

- Year of birth: 1980

## Education

- M.Sc. Physics, Royal Military College of Canada (RMCC), 2004.

- B.Sc. (First class honours) Space Sciences, RMCC, 2002.

## Employment

- Military Faculty/Lecturer, Department of Physics, RMCC, 2013–present.

- Teaching Assistant/Ph.D. Candidate, Department of Physics, RMCC, 2013–present.

- Teaching Assistant/Ph.D. Student, Department of Physics, RMCC, 2011-2013.

- Officer-in-Command, 5 Area Support Group Signals Squadron, Canadian Forces Base (CFB) Valcartier, 2009-2011.

- Infantry Battalion/Battle Group Signals Officer, CFB Valcartier & Kandahar, Afghanistan, 2006-2009.

- Staff Officer, 5 Headquarters & Signals Squadron, CFB Valcartier, 2005-2006.

- Teaching Assistant/M.Sc. Candidate, Department of Physics, RMCC, 2003-2004.

## Publications

### Journal Articles

- P.J.G. Perron, J.-M. Noël, J.-P. St-Maurice and K. Kabin, Ion temperature anisotropy effects on the dispersion relation and threshold conditions of a sheared current-driven electrostatic ion-acoustic instability with applications to the collisional high-latitude F-region, *J. Plasma Phys.*, submitted 9 January 2014.

- P.J.G. Perron, On the requirement of space weather situational awareness to achieve effects in a joint, interagency, domestic and arctic environment, *Canadian Military Journal*, submitted 14 August 2013 (Expected to be published in Fall 2014).

- P.J.G. Perron, J.-M. Noël, K. Kabin and J.-P. St-Maurice, Ion temperature anisotropy effects on threshold conditions of a shear-modified current driven electrostatic ion-acoustic instability in the topside auroral ionosphere, *Ann. Geophys.* 31 (3), 451-457, 2013, doi:10.5194/angeo-31-451-2013.

- P.J.G. Perron, J.-M. A. Noël and J.-P. St.-Maurice, Velocity shear and current driven instability in a collisional F-region, *Ann. Geophys.*, 27, Issue 1, 381-394, 2009, doi:10.5194/angeo-27-381-2009.

- J.-P. St-Maurice, J.-M. Noël and P.J.G. Perron, An assessment of how a combination of shears, field-aligned currents and collisions affect F-region ionospheric instabilities, *J. Plasma Phys.* 73 (1), 69-88, 2007, doi: 10.1017/S002237780600434X.

### Conference Proceedings (Oral and Poster Presentations)

- P.J.G. Perron, J.-M. Noël, J.-P. St-Maurice and K. Kabin, Possible direct generation mechanisms of small-scale irregularities in the auroral F-region and their relation to coherent and incoherent scatter radar observations, Division of Atmospheric and Space Physics (DASP) of the Canadian Association of Physicists (CAP) meeting, Fredericton, New-Brunswick, February 19-21, 2014.

- P.J.G. Perron, J.-M. Noël, J.-P. St-Maurice and K. Kabin, Effects of ion temperature anisotropy and shears on PFISR theoretical incoherent scatter spectrum of stable CDEIA modes in the topside auroral F-region, 2013 American Geophysical Union (AGU) Fall Meeting, San Francisco, California, US, 9-13 December 2013.

- P.J.G. Perron, J.-M. Noël, J.-P. St-Maurice, K. Kabin and J. De Boer, Effects of ion temperature anisotropy and shears on PFISR theoretical incoherent scatter spectrum of stable CDEIA modes in the topside auroral F-region, DASP annual meeting, Kingston, Ontario, February 18-20, 2013.

- J. De Boer, J.-M. Noël, J.-P. St-Maurice and P.J.G. Perron, Modeling the perpendicular electric field structure in the vicinity of auroral precipitation arcs, 2012 AGU Fall Meeting, San Francisco, California, US, 3-7 December 2012.

- P.J.G. Perron, J.-M. Noël, J.-P. St-Maurice, K. Kabin and J. De Boer, Ion temperature anisotropy effects on threshold conditions of shear-modified current driven electrostatic ion-acoustic instability in the auroral F-region, 2012 AGU Fall Meeting, San Francisco, California, US, 3-7 December 2012.

- P.J.G. Perron, J.-M. Noël, K. Kabin and J.-P. St-Maurice, Ion temperature anisotropy effects on threshold conditions of shear-modified current driven electrostatic ion-acoustic instability in collisional F-region, Physics in Canada, Vol. 68, No. 2 (supplement), 2012 CAP Congress, University of Calgary, Calgary, Alberta, June 11-15, 2012.

- P.J.G. Perron, J.-M. Noël and J.-P. St-Maurice, Ion velocity shears and low frequency oscillations in a collisional ionosphere: numerical analysis of the kinetic dispersion relation, University of Western-Ontario, DASP Annual Workshop, London, ON, February 2004.

- P.J.G. Perron, J.-M. Noël and J.-P. St.-Maurice, Electron shears and low frequency oscillations in a collisional ionosphere, Eos Trans. AGU, 85(17), Jt. Assem. Suppl., Abstract SM53B-10, 2004.

- P.J.G. Perron, J.-M. Noël and J.-P. St-Maurice, Electron velocity shears and low frequency oscillations in a collisional ionosphere, University of Western-Ontario, DASP Annual Workshop, London, ON, February 2004.

## Thesis

- P.J.G. Perron, Shear and current driven electrostatic instability in a collisional ionosphere - Numerical analysis of the fluid and kinetic dispersion relation, Department of Physics, Royal Military College of Canada, M.Sc. Thesis (Physics), April 2004, 153 pages.

## Seminar / Physics Department Colloquium Presentation

- P.J.G. Perron, Possible direct generation mechanisms of small-scale irregularities in the auroral F-region and their relation to radar observations, Department of Physics, RMCC, 14 March 2014.

## Other Student Activities

- Military Post-Graduate (PG) Students Representative (member) on the Graduate Studies Committee, RMCC, 2013-present.

- Chair, Miliary PG Students Committee, RMCC, 2013-present.

- Organizer for the 2013 PG Students Orientation Day, RMCC, September 2013.

- Organizer for the Space Science Group Seminar Series, Department of Physics, RMCC, 2011-2012.

- Member of the RMCC Stage Band, 2011-2012.

## Professional Activities

- Member, Canadian Association of Physicists (Division of Aeronomy and Space Physics, Division of Plasma Physics), 2011–Present.

- Member, American Geophysical Union, 2011–Present.

## Honours, Awards & Scholarships

- Canadian Defence Academy Research Program (CDARP) Awardee for research proposal entitled: Space weather nowcasting capability to determine effects on high-frequency (HF) radio communications in the Arctic, 14400$, March 2014.

- Best Student Oral Presentation, Division of Atmospheric and Space Physics, Canadian Association of Physicists, Fredericton, February 2014.

- Honourable Mention for outstanding student research paper, Canadian Association of Physicists, Calgary, June 2012.

- Best Student Poster Presentation, Division of Atmospheric and Space Physics, Canadian Association of Physicists, Calgary, June 2012.

- Canadian Forces Decoration, 2010.

- General Campaign Star, OPERATION ATHENA, Kandahar, Afghanistan, October 2009.

- 5 Canadian Mechanised Brigade Group Commander's Commendation for outstanding contribution during the Standing Contingency TF Experiment Exercice, June 2007.

- Governor General's Academic Gold Medal, RMCC, May 2004.

- Governor General's Academic Silver Medal, RMCC, May 2002.

- Defence Research and Development Branch Scholarship, May 2002.

- Metro Richelieu Inc. Scholarship, 2002.

- Stuart S. Barton Science Award, RMCC, May 2002.

- Physics Departmental Medal Award, Space Sciences Program, RMCC, May 2002.

- Military Engineering Award, RMCC, May 2002.

- Military Leadership Excellence Medal Award, RMCC, May 2001.

## Other Courses & Formations

- SuperDARN Graduate School, University of Saskatchewan, May 22-24, 2013.

- Certificate of Proficiency in Amateur Radio, Basics with Honours, April 2013.

- Incoherent Scatter Radar Summer School, Banff, July 30-August 4, 2012.

- Canadian Forces (CF) Network Operations Course, CF School of Communications and Electronics, Kingston, 2010.

- Civilian Human Resources Management Course, Department of National Defence, Montreal, 2010.

- Information Technology Infrastructure Library (ITIL) foundations version 3, Quebec, 2010.

- Land Forces Command and Staff College, Army Operations Course, Kingston, 2007.

- Officers Professional Military Education Program, 2006.

- Workplace Relations Advisor & Harassement Advisor Course, Quebec, 2005.

- Intermediate Spanish Course, St-Lawrence College, Kingston, 2003.